공학박사학위논문

기술 포트폴리오 평가를 포함한 미래항공 모빌리티의 확률론적 설계 프로세스

Improved Probabilistic Design Process for Advanced Air Mobility with Technology Portfolio Assessment

2023 년 2 월

서울대학교 대학원

기계항공공학부

임 대 진

기술 포트폴리오 평가를 포함한 미래항공 모빌리티의 확률론적 설계 프로세스

Improved Probabilistic Design Process for Advanced Air Mobility with Technology Portfolio Assessment

지도교수 이 관 중

이 논문을 공학박사 학위논문으로 제출함

2022 년 11 월

서울대학교 대학원

기계항공공학부

임 대 진

임대진의 공학박사 학위논문을 인준함

2022 년 12 월

위 원 장 : 권 기 범

부위원장 : 이 관 중

위 원 : 김 형 진

위 원 : 이 상 아

위 원 : 정 기 훈

Abstract

Improved Probabilistic Design Process for Advanced Air Mobility with Technology Portfolio Assessment

Daejin Lim
School of Mechanical and Aerospace Engineering
The Graduate School
Seoul National University

Within the last several decades, breakthroughs in multiple disciplines of aircraft technology and design have paved the way to the advent of a novel aircraft system that is collectively referred to as advanced air mobility these days. Specifically, the increasing maturity of electrified propulsion technologies is one of the most powerful drivers for various configurations for advanced air mobility and its possible operation in urban areas.

The novelty of advanced air mobility makes it difficult to use historical data accumulated during over half of a century in the earlier design phase where

numerous iterative processes are carried out to derive design requirements and initial sizing layout and information as a starting point of the design. Therefore, a physics-based design approach is necessary for the initial sizing of advanced air mobility and the conceptual design has become more significant. In efforts to derive a more reliable and credible design for advanced air mobility, the improvements in two primary tasks in the conceptual design phase were achieved with the use of the statistical and probabilistic methodology in this study.

The first task is “technology assessment” to list up available technologies and decide which technology portfolio could bring the success of aircraft development with the maximum effectiveness and the minimum cost increasement. Presented is an uncertainty-based technology portfolio assessment framework based on mathematical formulations that are more realistic and practical in addition to taking into account the interaction between technologies and uncertainties associated with the impact of technologies and the surrogate model itself. This method possibly enables elevating the level of knowledge in the conceptual design phase, which eventually leads to a reduction of the number of iterative design feedbacks and committed cost for the life cycle of the advanced air mobility.

The second task is “sizing” to obtain overall dimension and weight distribution for the further design phases. Not only was presented a deterministic sizing framework for advanced air mobility firstly, but uncertainties from physical geometric parameters and simplified mathematical analysis modules were also identified and imposed into the sizing framework with Monte Carlo simulation. The

expansion to uncertainty-incorporated sizing allows securing a proper buffer or margin in sizing result, and allows understanding the system response to the uncertainties in the earlier design phase, which makes decision-makers prepare for the next design phase.

Both improved frameworks were demonstrated on a hypothetical advanced air mobility of vertical take-off and landing configuration with full electric propulsion system, respectively. The demonstrations showed the validity of the presented frameworks providing ways for utilization and interpretation of their application consequences. Both uncertainty-based frameworks for technology portfolio assessment and sizing of advanced air mobility are platform-agnostic frameworks that are applicable to various aircraft development programs. Hence, the base philosophy of the frameworks can be shared broadly.

Keywords: Advanced air mobility, eVTOL, Conceptual design phase, Sizing method, Multidisciplinary analysis, Technology portfolio assessment, Uncertainty-based design, Uncertainty quantification, Model uncertainty

Student Number: 2017-27961

Table of Contents

Nomenclature

Symbols

a	element of TIM
a	speed of sound
A	rotor disk area
Alt	alternative candidate
AR	aspect ratio
b	element of TCIM
c	chord length
C	cost parameter
$Capa$	battery capacity
C_D	3D drag coefficient
C_d	2D drag coefficient
C_L	3D lift coefficient
C_{L_α}	3D lift coefficient curve slope
C_l	2D lift coefficient
C_{l_α}	2D lift coefficient curve slope
Co_f	coefficient for equivalent plat plate area
C_P	power coefficient
C_T	thrust coefficient
Day_{oper}	yearly operational days

e	element of TPEM
e	Oswald factor
$E[\cdot]$	expectation operator
E_{bat}	battery energy capacity
F	Prandtl's tip loss factor
f	equivalent flat plate area
f_{ad}	adjustment factor
GW	gross weight
I	current
$k_{e_{D_0}}$	correction coefficient for zero lift drag influence
k_{e_M}	correction coefficient for Mach number influence
k_{e_F}	correction coefficient for fuselage influence
L_{rod}	rod length
LC_{bat}	usable discharge cycle of battery
$LtoD_e$	effective lift to drag ratio
M	Mach number
N_{rod}	the number of rods
N_{rotor}	the number of rotors
N_s	the number of samples
N_{tilt}	the number of tilt actuators
N_z	load factor
N_b	the number of blades

p_{m_L}	root mean squared sound pressure for loading noise
p_{m_T}	root mean squared sound pressure for thickness noise
P	power
Q	rotor torque
r	nondimensional spanwise location of rotor blade
R	system response of interest
R_{rod}	supporting rod radius
R_{rotor}	rotor radius
s	system attribute
S_{ref}	reference area
S_w	wing area
SE_{bat}	specific energy of battery
SI	sensitivity index
SP	specific power
t	element of TPM
t_{rod}	supporting rod thickness
T	technology symbol
t/c	maximum airfoil thickness ratio
T_{rotor}	rotor thrust
tw	rotor blade twist variant
V_∞	freestream speed
V_{tip}	rotor tip speed

w	weight factor for effectiveness calculation
W	weight
y	quantity of interest

Greek letters

α	relaxation factor for gross weight convergence
α	scale parameter for Weibull distribution
α_{tilt}	tilt angle
$\alpha_{w_{inc}}$	wing incidence angle
β	rotor twist angle
β	Prandtl-Glauert parameter
β	shape parameter for Weibull distribution
χ_{bat}	battery discharge C-rate
Δ	interaction factor
η	efficiency coefficient
κ	ratio of 2D lift curve slope to 2π
κ_{tech}	correction factor for technology improvement
λ	taper ratio
λ	rotor inflow velocity ratio
Λ	sweepback angle
μ	mean or expectation
$\tilde{\mu}_3$	skewness coefficient

Ω_{rotor}	rotational speed of rotor
ϕ	induced angle of attack
$\prod$	product operator
ρ_{air}	air density
ρ_{rod}	rod material density
σ	standard deviation
σ^2	variance
σ_R	rotor solidity
$\sum$	summation operator
θ	collective pitch angle
θ	model uncertainty parameter

Subscripts

avionics	avionics system
bat	battery
BL	baseline
ht	horizontal tail
inv	inverter
max	maximum
mot	motor
out	output
rotor	rotor

unit	unit
vt	vertical tail
w	wing

Abbreviations

ANOVA	Analysis of variance
BEMT	Blade element momentum theory
BET	Blade element theory
CDF	Cumulative distribution function
COV	Coefficient of variation
DOC	Direct operating cost
DoD	Depth of discharge
DOE	Design of experiment
EASA	European union aviation safety agency
EE	Economic effectiveness
EIS	Entry into service
EP	Economic parameter
EPS	Electric propulsion system
eVTOL	electric vertical take-off and landing
FAA	Federal aviation administration
FH	Flight hour
FM	Figure of merit

GW	Gross weight
LHS	Latin hypercube sampling
MCS	Monte Carlo simulation
MLP	Multilayer perceptron
NPP	Normal probability plot
OASPL	Overall sound pressure level
PDF	Probability density function
PE	Performance effectiveness
PP	Performance parameter
RDT&E	Research, development, test, and evaluation
RISPECT+	Rotorcraft initial sizing and performance estimation code and toolkit plus
RPM	Rotational per minute
RSM	Response surface method
SE	System effectiveness
SoC	State of charge
SPL	Sound pressure level
TCIM	Technology compatibility and interaction matrix
TCM	Technology compatibility matrix
TIM	Technology impact matrix
TMS	Thermal management system
TPEM	Technology portfolio effect matrix

TPEV	Technology portfolio effect vector
TPM	Technology portfolio matrix
TPV	Technology portfolio vector
TRL	Technology readiness level
VLM	Vortex lattice method

List of Figures

List of Tables

Chapter 1

Introduction

1.1. Background of the Research

Aircraft design is a sophisticated, complicated, and iterative process in nature from concept sketches to a complex integrated system. It is a distinct discipline in aerospace engineering such as aerodynamics, aeroacoustics, structures, propulsions, controls, and weight and balance. Aircraft design involves all these disciplines together communicating with each other to reach a common goal for a designed aircraft. As the aircraft system itself has become more complex, which is a consequence of desiring higher and better performance, the design process has also become systematically well organized. Nowadays, the organized design process has been continuously evolving to accommodate evolutionary or revolutionary aircraft.

Within the last several decades, breakthroughs in many disciplines pave the way for the advent of a novel aircraft system that is collectively referred to as advanced air mobility these days. Among the breakthroughs, the electrified propulsion system using electric motors is one of the most powerful drivers to result in various configurations for advanced air mobility and possible operation in urban areas. Some examples of the exclusive configurations of advanced air mobility are shown in Fig. 1.1 [1] where multiple vertical rotors and wing systems for the electric vertical take-off and landing (eVTOL) can be seen. Their own operational characteristics include relatively lower flight altitude, shorter flight range, flying over crowded residential

area, and a greater number of vehicles in restricted airspace compared to conventional aircraft.

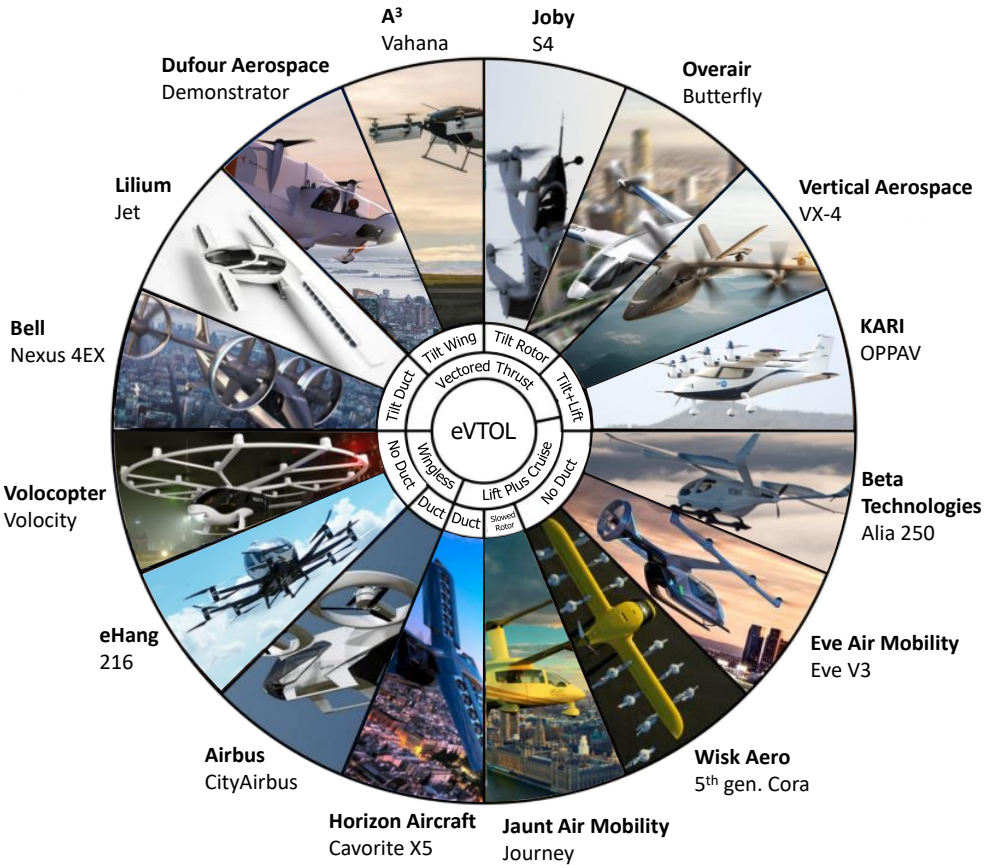

Fig. 1.1. the electric VTOL wheel of fortune

(Modified and updated from Ref. [1])

The representative design process for the aircraft starts with settlement of system requirements, concept study, and conceptual design for the targeted aircraft. There are several difficulties in designing advanced air mobility. Firstly, to bring future aircraft system into reality, technological drivers are needed to be identified satisfying target performance and requirements. Another difficulty is a design of advanced air mobility itself. Since available design knowledges and information are little in the earlier design phase, empirical methods based on historical data and experience are usually used for the tasks. However, it is a little bit difficult and sometimes impractical to apply historical data accumulated over half a century to the design of advanced air mobility due to its exclusive configurations and unique operational characteristics. Hence, a physics-based design approach is necessary for the initial sizing of advanced air mobility, and the conceptual design phase has become crucial to designing credible advanced air mobility from a given set of design requirements. In addition to them, during the procedure, it is also necessary to identify uncertainties in the system and process, to analyze and understand their effect on the tasks since there is little information on the system response as mentioned before. From a brief review of the conventional design process and descriptions of the primary tasks in the conceptual design phase, primary tasks-related studies for advanced air mobility and their limitations follow.

1.1.1. Brief review of a design process

The representative aircraft development process is shown in Fig. 1.2 [2] where major steps and their relationship are presented. The complete process can be divided three processes: requirements draw, system design, and manufacturing and testing. The system design process is usually broken into the conceptual design phase, preliminary design phase, and detail design phase. The level of complexity, maturity, and information of the system keeps increasing as the design phases progress. Among the three design phases, this paper focuses on the conceptual design phase and brief reviews of each step are described in the following sections. Details of the design process can be found in several design materials [2–5].

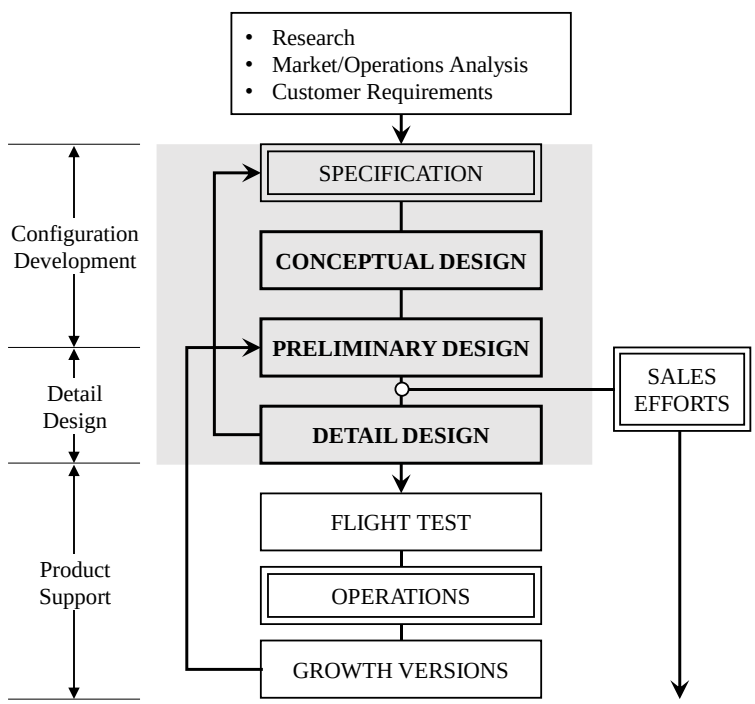

Fig. 1.2. Representative aircraft development process

(reproduced from Ref. [2]. Courtesy of J.H. McMasters [6])

System requirements (Pre-conceptual design)

As part of the aircraft design process, the very first step is to draw and confirm the top-level requirements, which will act as guidelines, objectives, and constraints during the design phase. The sources of requirements are diverse including market customers, aircraft operators, governments, and airworthiness regulations. The mission profile, performance capability, and the restriction of dimension are three examples that can be obtained by conducting market research, interviewing potential customers, and researching technology development. Sometimes, this phase is merged in the early stage of the conceptual design phase because the adequacy and properness of some of the requirements can only be evaluated by objective numbers obtained through a quick drawing, trade-off study, and initial sizing.

Conceptual design phase

Based on the established design requirements, the conceptual design phase is initiated. The ultimate goal of this phase is to generate a baseline design that meets and outdoes the requirements. The baseline design encompasses a proof of concept, overall dimension, geometry and arrangement of major components, weight distribution, flight performance, cost information, or a list of applied technologies. The most critical aspect of the conceptual design phase is to reflect the interactions between as many components as possible and across all disciplines, rather than to result in detailed information for a certain component. The baseline design does not need to be optimized, but it would be better to optimize it at the conceptual design

phase. As a result of the conceptual design phase, some of the design characteristics and arrangement of the aircraft are set to be frozen after a successful system design review process. Since the obtained baseline information is the starting point of further design phases, it is necessary to incorporate technical risks and evaluate the possibility of failure as much as possible during all the tasks in this phase.

Preliminary design phase

In the preliminary design phase, attention is shifted away from the top system level (the aircraft itself) to the subsystem level in different disciplines, while pursuing higher-level details and sophistication. It is the goal of this phase to elaborate on the component design prior to moving on to the detail design phase. Validation of the sophisticated design is conducted at this stage before reflecting "real-world" aspects such as attachment parts, gap sealing, and joint connections which are considered in the detail design phase.

Detail design phase

In the detail design phase, the actual component design with the highest level of detail is carried out. The components are prepared for manufacturing, assembly of subsystems, and building of the aircraft as a whole. Tests are conducted in real compartments. After the detailed design phase, production of the aircraft begins with making production tooling and the aircraft is delivered to customers after completing flying tests and getting certification from related regulatory authorities.

1.1.2. Importance of conceptual design phase

Complex aeronautical systems are typically developed with a long timeframe from concept study to entry into service (EIS), followed by a long operational life cycle. They usually are some years in the design and manufacturing process, several years in the certification process, and a couple of decades in operations before getting disposed of. For example, UH-60 Blackhawk took 9 years and AH-64 Apache took 14 years from the initiation of the program to its first deployment, respectively [7]. The averaged timeframe of Airbus and Boeing airliners is 6.5 years [8]. This implies that the conceptual design phase precedes much earlier before the date of EIS.

Though all of the phases in the design process are important, the conceptual design phase is particularly significant since it is the first step of aircraft design in which a blueprint layout of the target aircraft configuration is determined. This then serves as the basis for the rest of the process. Quantitatively, the importance of the conceptual design phase is usually presented by the impact on the life cycle cost of the aircraft. Fig. 1.3 shows a well-known relationship in system engineering: cumulative percent of the life cycle cost according to the development phase [9]. There are three lines in the figure: a solid line for “Cost committed”, a solid bold line for “Cost expended”, and a dashed line for “Ease of change”. As can be seen in the figure, almost 80% of life cycle cost have been committed before the end of the design and development phase with a very small amount of expended cost. 70% of the life cycle cost is even committed at the first development phase where conceptualization, or conceptual design, is conducted. Since the level of “ease of

change" decreases exponentially as the development progresses, the cost of change for faulted design drastically increases like the butterfly effect. Suppose that flaws are discovered in the later design phase, manufacturing or test phase. The later flaws are discovered, the larger amount of expended endeavors, labors, and budgets become meaningless. Moreover, similar processes are reduplicated again to fix the flaws or redesign. These tragic situations must lead to an unexpected rise in research, development, test, and evaluation (RDT&E) cost, an increase of the acquisition cost of the aircraft, and a delay of the date of EIS. A development program failure may also be the result. This phenomenon is shown with the centered arrow line displaying exponential increases in cost to fix problems. In short, decisions made in the early stage have a significant impact on the future output, so that the conceptual design phase is relatively much more important than others.

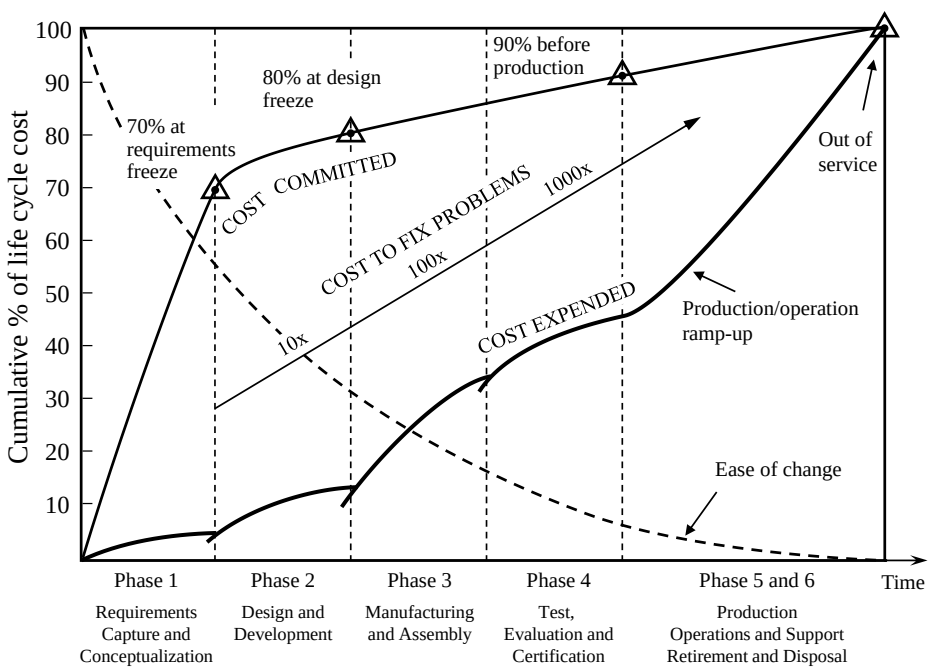

Fig. 1.3. Cumulative percent of life cycle cost by the development phase [9]

1.1.3. Primary tasks in the conceptual design phase

As mentioned earlier, the ultimate goal of the conceptual design phase is to generate a baseline concept including overall dimension, layout and weight distribution. To this end, there are two traditional tasks and an emerging task. The two traditional tasks are “technology assessment” and “sizing”. A task that has emerged during the past several decades is to incorporate the uncertainty effect into traditional tasks in order to reduce the likelihood of failure occurring in the later design phases and the number of design feedbacks for fixing defects or flaws. They are three pillars for the conceptual design as shown in Fig. 1.4.

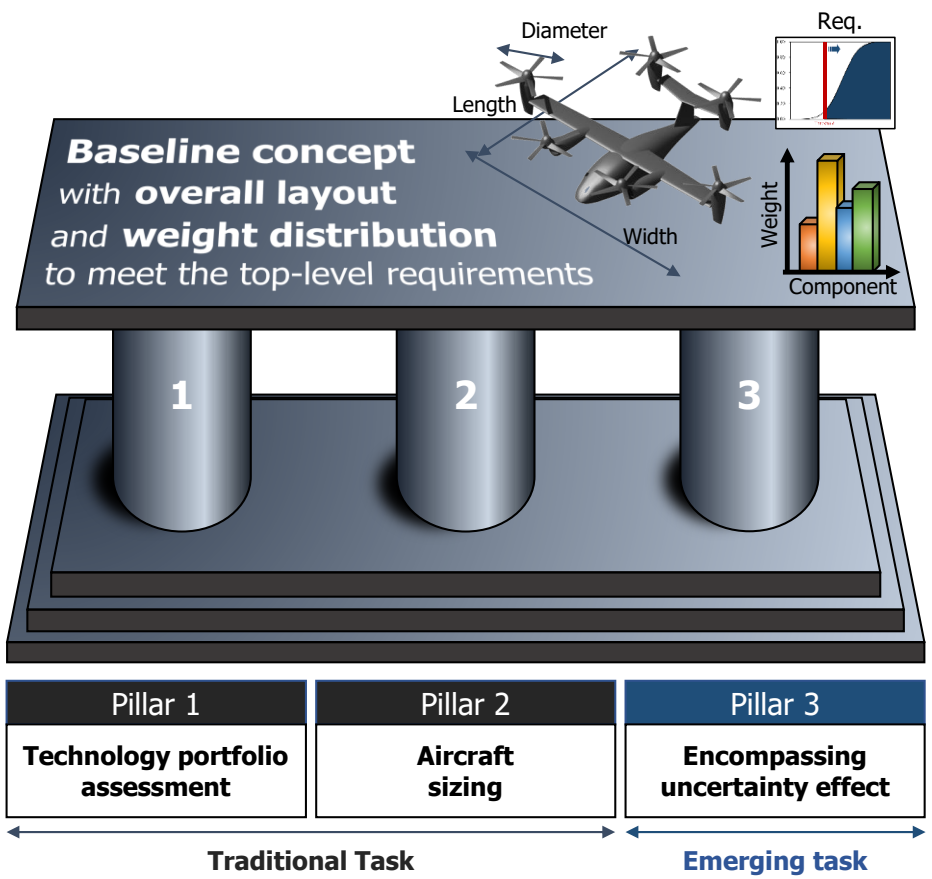

Fig. 1.4. Objective and three pillars of the conceptual design phase

Technology assessment

One of the most challenging works in the conceptual design phase is to list up technologies available and decide which technologies will be selected for the aircraft system development to meet the top-level requirements. Technologies in the shortlist should be assessed with respect to performance improvement, economic benefits, safety augmentation, reliability, operational aspect, environment compatibility, etc. The goal of this task is to identify and select technologies that could derive the most effective solution. As mentioned earlier, the conceptual design precedes much earlier before the aircraft appears and aviates in the real world. At the time point when the aircraft shows up, the customer requirements and expectations for aircraft performance, also referred to as voice of customer, are usually higher than performance that could be achieved by up-to-date fully mature technologies at the time point when the conceptual and preliminary design phase is progressing. As a result of not reaching the target performance indices, the aircraft has no choice but to become obsolete faster than its competitors in the market. Therefore, if a design is to be built in the distant future, an assessment of all possible technologies including emerging and immature ones should be conducted to satisfy system requirements from customers, or feedback to the system requirements phase for relaxation of design requirements.

Sizing and layout determination

Sizing is the most important task in the conceptual design phase. It could be said that sizing is "*Alpha and Omega*" of the conceptual design. From Ref. [3], sizing is described as follows.

> *"Sizing literally determines the size of the aircraft, specifically the weight that the aircraft must be designed to so that it can perform its intended mission carrying its intended payload* [3]*."*

As results of sizing process, the designer can reach the answer to the question of how big and heavy aircraft should be designed for conducting the required mission profile. The answer to "how big" is the overall layout and dimensions of components and the answer to "how heavy" is the weight distribution of the targeted concept configuration. These questions can be answered by simply looking at historical data or by analysis through physics-based methodologies in different disciplines. In the case of advanced air mobility, however, the second approach is more appropriate because the revolutionary design concept makes some parts of the historical data less applicable. Hence, the candidate design concept configuration is sized iteratively with consideration of the interaction between multiple disciplines such as aerodynamics, propulsion, stability and control, and weight engineering. Used design tools and analysis techniques are usually semi-empirical data or simplified mathematical models that have low or middle fidelity to enable quick and fast trade-off studies. Their prediction errors are typically around 5~10% when compared to data from high-fidelity tools, wind tunnel tests, or flight tests. [2].

Encompassing uncertainty effect

In addition to the two traditional primary tasks, another emerging important task is examining the effect of uncertainty on the results of the conceptual design phase. As can be seen in Fig. 1.3, decisions made in the conceptual design have a significant impact on the life cycle cost and the following procedures, so that a proper margin or bumper is needed. Traditionally, a constant factor that is usually referred to as a safety factor or safety margin is applied to secure the bumper area in the design space. However, the traditional method has limitations in the determination of the safety factor for which how much it should be, and therefore, the possibility of "over-design" or "under-design" owing to the inappropriate safety factors. Historical data is not often appropriate for the design of advanced air mobility since the configuration and system architectures are significantly different from conventional aircraft. The uncertainty quantification process in the conceptual design is an aspect of growing concern with regard to deciding on appropriate safety factors. The advancement in computational analysis speed and probabilistic methods enable uncertainty quantification that requires demanding computational resources and time. Through the uncertainty quantification process in the conceptual design phase, it could be achieved a reduction of the number of iterative processes within the conceptual design and between later design phases, and finally increase in the possibility of the success of the aircraft development program.

1.2. Previous studies concerning the primary tasks

Focusing on the primary tasks of the conceptual design phase, many previous studies have been conducted. They are presented here as well as briefly summarized, along with their values and limitations.

Technology assessment

The several frameworks for helping to investigate technology impact have been developed through decades with similar objectives [10–18]. Research teams from Georgia Tech browsed available technology portfolios and evaluated their impacts on various aerospace systems [10–12]. Recent research from other institutes proposed a framework for technology portfolio selection with their own philosophy [13–16], or assessed a specific technology impact on the aircraft systems [17,18]. They all have paved the way to assessing single technology or technology portfolios, but also have limitations in the perspective of realistic validity.

To the authors' best knowledge, the previous studies calculated an accumulated effect of multiple technologies with an additive approach by linear algebra using a matrix inner product. Although the additive approach provides easy and fast calculation during the process of collecting multiple technology effects, one of the issues with the simple summation is that unrealistic situations might occur with the violation of physical limits. Suppose two technologies are independent of each other and are expected to reduce component weight by over 50%, respectively. The additive approach results in a reduction of component weight by over 100%, giving

a zero-mass or negative-mass situation. The further issue is that the non-linear interaction effect between technologies could not be reflected in the additive calculation. When comparable technologies that have an effect on the same system attributes are applied simultaneously, the resultant effect could be amplified or undermined when compared to a single technology-applied scenario. One of the previous studies [11] presented an improved calculation method by adopting correction factors named as technology synergy matrices, but the fundamental was still based on the additive approach.

In the perspective of uncertainties, the previous studies assumed the precise impact of technologies on aircraft system [11] or adopted probabilistic approaches only for the impact of technologies considering their own uncertainties [10,12–18]. Nevertheless, in reality, the uncertain parameters prevail in the other sections such as aircraft geometry, operational conditions, physics-based design tools, and even surrogate mathematical models. The analysis and design tools that are used in the earlier design phase have more uncertainties than those used in the detail design phase because of the compromise between their calculation time and analysis fidelity. In particular, surrogate mathematical models that are usually used for the propagation of uncertainties are an inevitable source of uncertainty during the process. However, the uncertainty from the surrogate mathematical models was excluded in the previous studies.

Sizing for advanced air mobility

After the advent of the advanced air mobility concept enabled by rapid improvement in electrified propulsion technology and concerns for environmental issues and sustainability of transportation systems, a lot of studies for the sizing of future aircraft with different electric propulsion systems have been conducted [19–30]. However, most of them specifically focused on integrating electrified propulsion systems into a conventional fixed-wing layout without considering various configurations and architectures. In addition to that, only few studies considered and analyzed the uncertainty effect on the performance of the aircraft, and most of them presented deterministic evaluation and sizing methods, so that sizing results were provided by scalar values for a fixed set of input parameters: for instance, gross weight of 5600 pounds., the rotational speed of the rotor of 1300 rotation per minute (RPM), and required battery energy of 120 kWh.

The first limitation that constrained applicability of the method depending on the configuration and propulsion architecture of the advanced air mobility was resolved by Ref. [19–21] where a generic conceptual design methodology that is applicable to various types of the advanced air mobility was developed by presenting four essential analysis modules.

However, the second limitation that the deterministic sizing methods were used is not addressed relatively much in the perspective of system responses, especially in the sizing of advanced air mobility. It's hard to find uncertainty quantification studies on the sizing of the advanced air mobility in the conceptual design phase.

Many uncertainty-related studies for the aircraft dealt with uncertainties in a specific discipline such as operational situations [31], computational aerodynamic analysis [32,33], acoustics [34,35], tracking and localization [36,37], emissions [27], and structural responses [38,39]. Although they are also necessary studies and milestones for the success of advanced air mobility, uncertainty quantification in the perspective of flight performance and sizing is required for a reliability-based design. Moreover, similar to the situation in the technology assessment category, uncertainties from simplified analysis models used in the conceptual design phase should be considered.

1.3. Motivation and objectives

Reviewing previous studies and the importance of technology portfolio assessment and sizing for advanced air mobility, it is evident that the assessment of a technology portfolio with an improved mathematical formulation and incorporation of diverse uncertainties is worth pursuing. They are needed to avoid unphysical simulation situations and to obtain the most probabilistically promising technology portfolio. Furthermore, when conducting the sizing process, it is imperative to consider the uncertainty effect to achieve reliability-based sizing and design. Since one of the most promising applications and uses of advanced air mobility is a transportation service in urban areas where the ramifications of accidents during operation are far more serious, the reliability of advanced air mobility is a substantially essential factor.

Thus, this study attempts to present improved methodologies for technology portfolio assessment and sizing of advanced air mobility under the uncertainty environments. To this end, improvement in the deterministic formulation of methodology for technology portfolio assessment and sizing framework is suggested firstly, and then, a stochastic method is combined with them for the uncertainty quantification after identifying uncertain parameters. Using the constructed frameworks, pilot projects are conducted to demonstrate the application and efficacy of the suggested methodology, respectively.

1.4. Outline of the dissertation

The remaining parts of this dissertation are organized as follow.

Chapter 2 mainly describes the two frameworks under deterministic environment. One is for the technology portfolio assessment in Section 2.1 where the process of technology portfolio assessment is presented step by step. The other is a multidisciplinary conceptual sizing framework for the advanced air mobility in Section 2.2 where primary modules of the sizing framework are described.

Chapter 3 provides information of various uncertainties underlying in the process of the technology portfolio assessment and the conceptual sizing framework, which expanding the deterministic environment into probabilistic environment. After briefly describing source of uncertainties and their classification, certain uncertainties interested in this study are identified including those in geometric parameters and simplified analysis modules. Then, specific methods for modeling, handling, and propagation of the uncertainties are presented.

In Chapter 4, the proposed methods are applied and demonstrated by using a hypothetical advanced air mobility aircraft. The improved probabilistic process for technology portfolio assessment shows how to select the most reliable and affordable technology combinations. The uncertainty quantification in the aircraft performance presents some insights and guidelines of understanding the characteristics of the uncertainties and handling them in the conceptual design phase.

Finally, the summarization, conclusion of the dissertation, and future works are provided in Chapter 5

Chapter 2

Formulation of Assessment and Design Framework

Chapter 2 mainly describes the main building blocks of two frameworks under a deterministic environment to present their fundamental concepts. One is for the technology portfolio assessment in the pre-conceptual design phase in Section 2.1 where the process of technology portfolio assessment is presented step by step. The other is a multidisciplinary sizing framework for advanced air mobility in Section 2.2 where major modules of the sizing framework are described.

2.1. Technology Portfolio Assessment

2.1.1. Overall Process

An overall process of the proposed technology portfolio assessment method is shown in Fig. 2.1. The process consists of three main building blocks. The "Technology portfolio" block starts with identifying and listing "*N*" technology candidates and then investigating their maturity levels. After three processes of 1) investigating compatibility and interaction between technologies, 2) identifying related system attributes, and 3) compiling possible technology portfolios, matrices that contain each information are generated. Through the combination of the three matrixes, the final resultant matrix is obtained for simulating the effects of technology infusion. The "Surrogate model" block proceeds parallel to the first block and it produces a mathematical substitute for the analysis and design tools.

Uncertainty in the surrogate model is estimated if necessary. Assessment of the technology portfolios is conducted in the “Computation and Post-Processing” block, taking into account the results obtained thus far. In this third step, the decision makers could gather valuable information, including the most advantageous portfolio of technologies and the anticipated benefits in terms of economics or performance quantities of interest. During the overall process, several uncertainties can be incorporated and uncertainty-related subprocesses are highlighted, which is described in Section 3.2 after detailing the deterministic-based process first. The three processes and key matrices are described step by step.

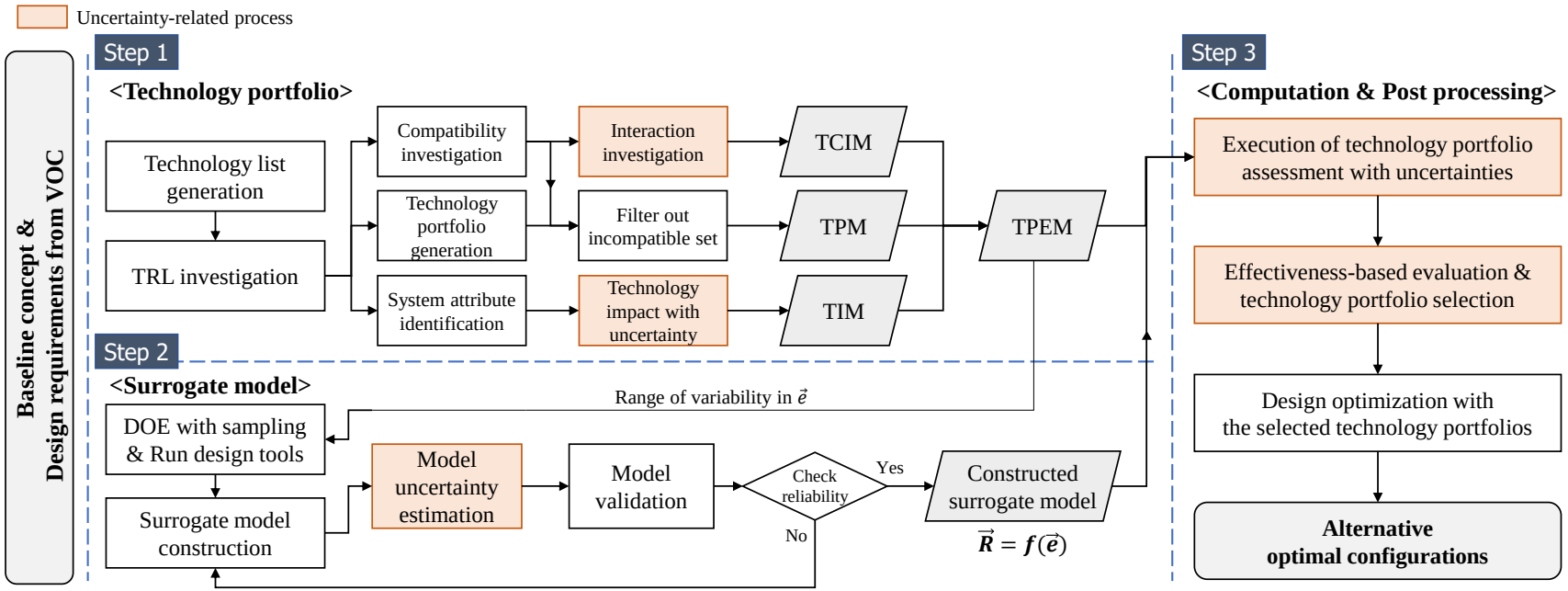

Fig. 2.1. Overall technology portfolio assessment process

2.1.2. Impact of Technologies in System Level

The very first step of the technology portfolio assessment process is a generation of the portfolios. From the "*N*" technologies, technology portfolios vector (TPV) can be obtained by choosing to include each technology, T_i, in the portfolio or not. A single TPV acts as a possible solution for an alternative design candidate, Alt_p. The elements of TPV are defined as follows:

$$\vec{T}|_{Alt_p} = (t_1, t_2, \cdots, t_N) \quad \begin{cases} t_i = 1, & if\ T_i\ is\ selected \\ t_i = 0, & if\ T_i\ is\ not\ selected \end{cases} \tag{2.1}$$

where p is the index of an alternative design candidate. The maximum index of the alternative design candidates is equal to 2^N if all "*N*" technology candidates are compatible to each other. The cluster of TPV constructs technology portfolio matrix (TPM). The TPM has "*p*" rows and "*N*" columns, shaping a "*p*" times "*N*" matrix.

In a conceptual design environment, it is difficult to embed, simulate, and assess future technologies due to the relatively low fidelity of the sizing and analysis tools that usually rely on historical data and simplified mathematical models. Thus, physical changes in fundamental level by the innovative technologies could not be considered directly in the earlier design phase. In order to mimic the situation where advanced technologies are applied to the aircraft system, the impact of each technology on aircraft system attributes was modeled as a single factor by previous studies [10–12]. The concept of impact factor is leveraged and this impact factor is defined by Eq. (2.2) in terms of percentage according to the variation direction of a system attribute, s_i, by a technology infusion. The system attributes can be any parameters of interest including component weight, specific energy of energy

sources, aerodynamic coefficients, component unit cost, and available operating days. For example, when carbon composite wing structure is applied (T_1), it can be given -10% of figure for an impact factor on weight reduction of wing ($a_{1,1} = -10\%$), which implies 10% reduction in the wing weight (s_1). Meanwhile, RDT&E cost (s_2) is expected to increase by 5% with the same technology, giving 5% as an impact factor on RDT&E cost ($a_{2,1} = 5\%$). Figures for not affected system attributes are given as zero. Using this factor allows both favorable effects and adverse effects of a technology to be incorporated in the earlier sizing and analysis environment.

$$a_{i,j} = \begin{cases} -, & if\ s_i\ is\ not\ affected\ by\ T_j \\ < 0, & if\ s_i\ is\ decreased\ by\ T_j \\ > 0, & if\ s_i\ is\ increased\ by\ T_j \end{cases} \tag{2.2}$$

Multiple numbers for the impact factor constitute a vector for a single technology, and then a technology impact matrix (TIM) is built by concatenating the vectors according to the number of identified technologies [10–12]. Similar matrices were also presented by other studies [13–16]. TIM is directly mapping the impact of "*N*" technologies to "*M*" system attributes. The elements of TIM can be quantified in various ways, such as literature reviews, high-fidelity physics-based computations, direct experiments, the Delphi technique, which relies on experts' opinions, and a possibility-theory-based method [18]. A notional TIM is shown in Fig. 2.2 which is an "*M*" by "*N*" matrix.

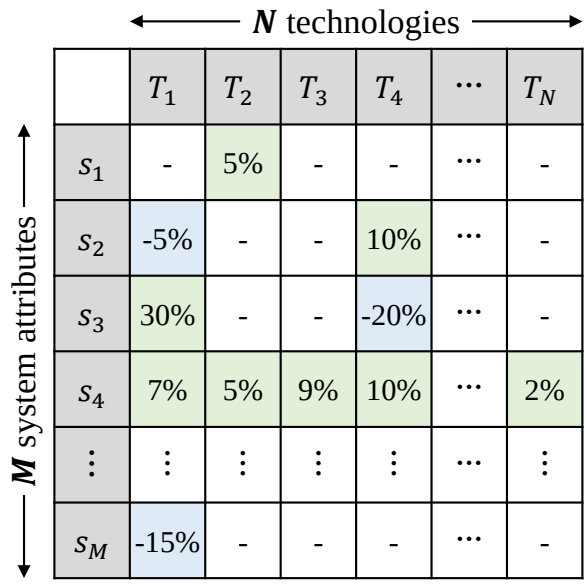

Fig. 2.2. Notional technology impact matrix

2.1.3. Technology Compatibility & Interaction

In order to reduce the size of the problem by filtering out incompatible technology combinations in the TPM, a so-called technology compatibility matrix (TCM) was usually used [10,11,13–16] before. In this study, typical TCM was expanded to be able to incorporate additional information of the interactions between "*N*" listed technologies, and then renamed as technology compatibility and interaction matrix (TCIM). The elements of TCIM are determined by the following rules:

$$b_{i,j} = \begin{cases} 0, & if\ T_i\ and\ T_j\ are\ not\ compatible \\ < 1, & if\ T_i\ gets\ uncooperative\ influence\ by\ T_j \\ 1, & if\ T_i\ and\ T_j\ are\ not\ influencing\ each\ other \\ > 1, & if\ T_i\ gets\ cooperative\ influence\ by\ T_j \end{cases} \tag{2.3}$$

The element of 1.05, for instance, means that a 5% additional favorable effect is obtained when compared to the situation where two technologies are independent. A typical TCM is a symmetric matrix since technology compatibility is most likely to be bidirectionally identical. If "A" technology is incompatible with "B" technology, the opposite should also be true.

It is possible, however, that some of the technology combinations may have asymmetrical relationships in terms of interaction between technologies, and their interaction effect might different which attributes are investigated. Let us suppose that the truss-braced wing technology and the carbon composite wing technology are selected in a TPV. The expected weight reduction impact by the carbon composite could be degraded because the junction of the wing and brace strut needs to be additionally reinforced or other metallic materials should be used to avoid tear of the

carbon. On the other hand, the expected aerodynamic performance increase by applying a truce-braced wing is not influenced by carbon materials. Another example could be a combination of a technology for anti-icing coating on the wing and a technology for flow control over the wing. Although the performance of the anti-icing coating may not deteriorate, the performance of the flow control technology might be degraded owing to roughness change by the surface coating.

In order to consider these kinds of situations TCIM in this study has an asymmetric structure. It is difficult to determine the figures for TCIM elements since many of the technologies of interest are so new that some of their characteristics are not completely understood as yet. Literature reviews, the Delphi method using expertise from the experts, and a possibility-theory-based method [18] could help to determine the TCIM like TIM. A notional TCIM is presented in Fig. 2.3.

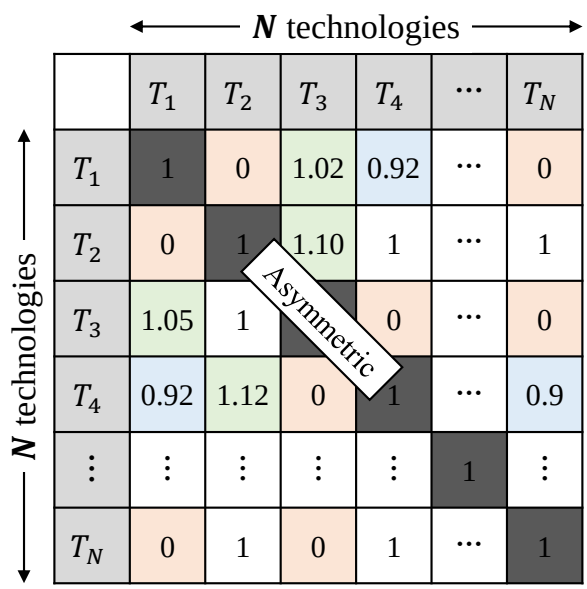

	T_1	T_2	T_3	T_4	⋯	T_N
T_1	1	0	1.02	0.92	⋯	0
T_2	0	1	1.10	1	⋯	1
T_3	1.05	1	1	0	⋯	0
T_4	0.92	1.12	0	1	⋯	0.9
⋮	⋮	⋮	⋮	⋮	1	⋮
T_N	0	1	0	1	⋯	1

Fig. 2.3. Notional technology compatibility and interaction matrix

Based on the elements of TCIM, interaction factor for i[th] technology, Δ_i, can be calculated by Eq. (2.4).

$$\Delta_i|_{Alt_p} \equiv \begin{cases} \prod_{j=1}^{N} \left\{ \left(b_{i,j} - 1\right) \cdot t_i t_j|_{Alt_p} + 1 \right\}, & for\ performance\ attributes \\ 1, & for\ cost\ attributes \end{cases} \quad (2.4)$$

The first basic assumption about the interaction factor is that the interaction factor has an influence only on performance-related aircraft characteristic parameters. For cost-related aircraft characteristic parameters, the interaction factor is negated. This is because that it is more usual that the situation where a certain amount of financial asset is consumed for the infusion of multiple technologies, but the resultant gain in system attributes might be bigger or smaller than expected.

The second assumption in the definition of Eq. (2.4) is that only pairwise interactional effects are considered, ignoring higher orders of interactional layer more than 2[nd] order relationship between multiple technologies. In other words, “A” technology which has an effect on “B” technology and “C” technology respectively will have the same magnitude of effect on “B” and “C” technologies individually although “A” technology might have different interactional magnitude with “B+C” combination. The schematic of pairwise interactional effect is graphically described in Fig. 2.4. Let me suppose again that the truss-braced wing technology and the carbon composite wing technology are selected in a TPV. In the event that a hybrid laminar flow control technology is additionally incorporated into the TPV, the expected outcome might be different due to structural or spatial issues in the wing in

which the two technologies are already infused. Nevertheless, since pairwise interactions are able to represent primary interactions among technologies, and an examination of all higher-order interactions would be practically irrational, this study presents the most practical solution as Eq. (2.4).

As a result, the TCIM and the interaction factor not only contribute to reducing the exploration area by eliminating the incompatible technology portfolios (reducing the dimension of TPM), but they also help to simulate the interactions between technologies.

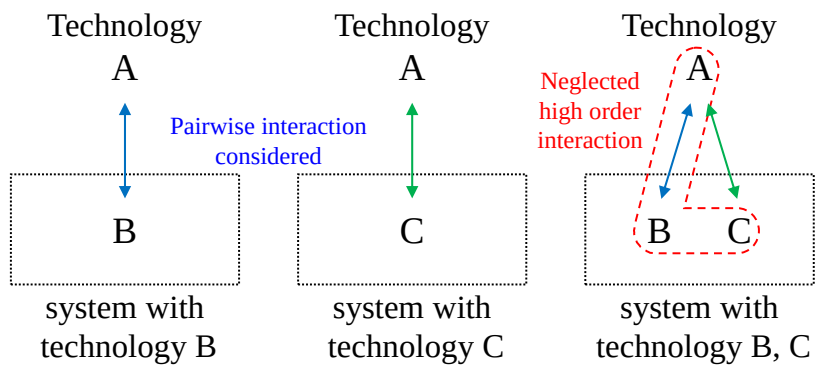

Fig. 2.4. Schematic diagram for interactional effect between technologies

2.1.4. Technology Portfolio Effect

At last, using the elements of the three matrices, TPM, TCIM, and TIM, a compounded impact on the system attributes by the infused technologies, e_i, is calculated by Eq. (2.5), and this forms a technology portfolio effect vector (TPEV) for an alternative design, $\vec{e}|_{Alt_p}$. The system attributes after technology infusion, $s_{i,tech}$, are calculated by Eq. (2.6) where $s_{i,baseline}$ means the system attributes of baseline with no technology infusion.

$$\vec{e}|_{Alt_p} = (e_1, e_2, \cdots, e_M), \quad e_i|_{Alt_p} \equiv \prod_{j=1}^{N} \left(1 + \Delta_j|_{Alt_p} \cdot a_{i,j} \cdot t_j|_{Alt_p}\right) - 1 \qquad (2.5)$$

$$s_{i,tech} = s_{i,baseline} \cdot (1 + e_i) \qquad (2.6)$$

The key difference to other studies [10–16] in the realization of multiple technologies' effect is that the calculation of $e_i|_{Alt_p}$, is based on a multiplicative calculation, not an additive approach. The multiplicative calculation is a more reasonable approach than the additive approach for several reasons. It is first noted that the elements of TIM are presented in percentage form, which implies that the variation of the system attributes by technology infusion is represented as multiplication against a certain baseline value; recall the definition of a percent. Another consideration is that the variation of the single attribute resulting from multiple technologies undergoes a series of overlapped effects, based on the technologies involved. Moreover, one of the issues with the simple summation is that

the unrealistic situations might occur with the violation of physical limits as explained in Section 1.2.; recall the zero-mass or negative-mass situation example. The further issue is that the non-linear interaction effect between technologies could not be reflected in the simple additive calculation.

As a consequence of this fundamental shift from addition to multiplication, it is possible to avoid in itself unphysical results, such as the zero or negative-mass situation. The product of Eq. (2.5) with a negative impact factor (decreasing impact) never reaches exactly zero value. Note that the interaction factor is multiplied in front of the elements of TIM and TPM on the inside of the permutation brackets in Eq. (2.5).

By compiling TPEVs for all possible alternative candidates, the technology portfolio effect matrix (TPEM) is obtained. The notional TPEM is shown in Fig. 2.5. The number of columns of TPEM is equal to "M" system attributes of the aircraft, and the number of rows of TPEM is equal to "p", all possible alternative candidates from "N" technologies after compatibility consideration. TPEM is the final resultant matrix in the "Technology portfolio" building block before feeding itself to the design tools or surrogate models for evaluation of the technology portfolio effect.

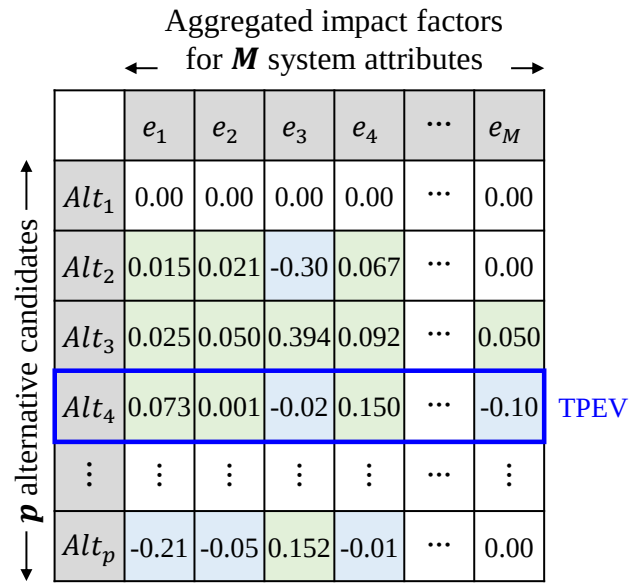

Fig. 2.5. Notional technology portfolio effect matrix

2.1.5. Evaluation by Surrogate Model

Using TPEM and Eq. (2.6), the evaluation of the technology portfolio can be directly conducted with the design and analysis tools by feeding the elements of TPEM into the simulation environment. However, most of the physics-based simulations require expensive computational resources and time, which makes the direct-evaluation method an impractical approach. Since the number of possible technology portfolios follows the power of 2, it would reach over a million in the case of that 20 technologies that are all compatible with each other (2^{20}). In this situation, the adoption of the surrogate models is an inevitable choice in terms of the computational resources and time management. More advantages of using the surrogate models are well described in Ref. [40] with aspects of proprietary protection from "reverse engineering" and connectivity between separated models from different operating environments. Various types of surrogate models are available depending on the specific problems of interest. The examples include regression-based models such as response surface method (RSM) [41,42], interpolation-based methods such as Gaussian process or Kriging [43], and neural network methods such as multilayer perceptron (MLP) [44].

Regardless of the specifically chosen method for the surrogate models, the primary function of the surrogate models here is mapping the vector of the compounded impact of technologies, $\vec{e}$, (input) with the vector of system responses of interest from the tools, $\vec{R}$, (output). In order to efficiently build the surrogate models, design of experiment (DOE) supported by sampling methods is frequently

used for selecting e_i subsets by exploring the multidimensional e_i space. The limit of e_i space can be informed from the range of e_i variations in each column of TPEM. It is important to know this limit because the result obtained with variables out of the range cannot be ensured to be meaningful. As a consequence of the DOE process, adequate sets of e_i combinations are derived for an input table of the surrogate models, and then the corresponding system responses for an output table of the models are obtained through the physics-based analysis tools. The two tables constitute the final knowledge table to build the surrogate models. After building the reliable surrogate models, the evaluation of technology portfolios progresses on the surrogate model environment using TPEM. Fig. 2.6 shows the above-mentioned process for constructing the surrogate model graphically.

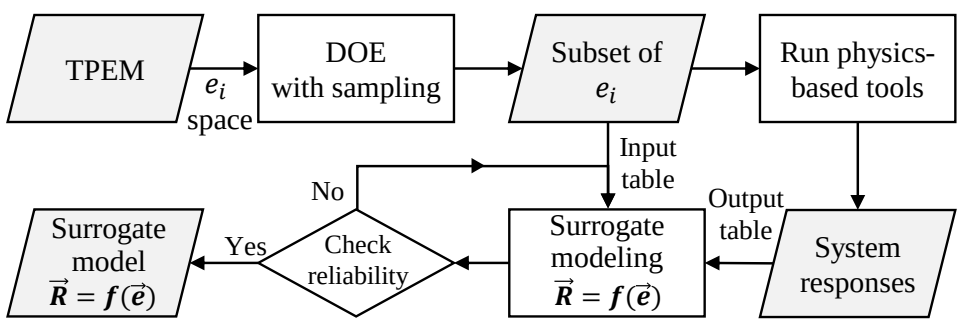

Fig. 2.6. Process of building the surrogate model

2.1.6. Selection by Effectiveness

The variations of the system responses of interest caused by the infused technologies are traced to evaluate the efficacy of the technology portfolios. Although they can be presented individually [15,16], the number of system responses of interest is typically more than 2, so that it could be difficult to figure out which technology portfolio shows better improvement with respect to the overall system at once. One of the methods that were previously suggested in Ref. [10] for evaluating and lining up the portfolios is adopted in this study with minor modifications. The efficacy of each technology portfolio is measured by effectiveness metrics which are defined as the weighted sum of normalized figures where the system-response quantities of interest are divided by those of the baseline configuration. The effectiveness metrics are maximum-desirable indices and they can be categorized and calculated typically with respect to performance and economics perspective. The performance quantities include any metric related to all disciplines at the system level as well as at the subsystem level. The representative examples at the system level are gross weight, energy capacity, lift to drag ratio, and maximum noise level of the aircraft. Structural safety margin, load factor, powertrain efficiency, and component weights are subsystem-level examples. The economics quantities include primarily cost-related parameters such as vehicle acquisition cost, operating cost, and RDT&E cost. The performance effectiveness, PE, and economic effectiveness, EE, are calculated by Eq. (2.7) and Eq. (2.8), respectively where "n" is the number of performance parameters, PP, and "m" is the number of economics parameters, EP.

The w_i is a weight factor for each parameter that the subjectivity of the decision makers is reflected in. The exponent of the parenthesis, d_i, indicates a desirable changing direction of the quantity compared to that of the baseline; "1" denotes a maximization-seeking quantity such as powertrain efficiency and operable days whereas "-1" denotes a minimization-seeking quantity such as gross weight and vehicle cost. These notations allow the effectiveness metrics to naturally be the maximum-desirable indices, which is well matched to the meaning of "effectiveness". Equation (2.9) calculates system effectiveness, SE, which is a weighted sum of performance effectiveness and economic effectiveness, representing a single score for technology infusion.

$$PE = \sum_{i=1}^{n} w_{PP_i} \cdot \left(\frac{PP_i|_{Alt_p}}{PP_i|_{BL}} \right)^{d_i} \quad where \begin{cases} d_i = -1 & for\ minimize \\ d_i = 1 & for\ maximize \end{cases} \tag{2.7}$$

$$EE = \sum_{i=1}^{m} w_{EP_i} \cdot \left(\frac{EP_i|_{Alt_p}}{EP_i|_{BL}} \right)^{d_i} \quad where \begin{cases} d_i = -1 & for\ minimize \\ d_i = 1 & for\ maximize \end{cases} \tag{2.8}$$

$$SE = w_{PE} \cdot PE + (1 - w_{PE}) \cdot EE \tag{2.9}$$

With the aid of these effectiveness metrics, the efficacy of the technology portfolios can be presented by a single aggregated figure that provides an easily understandable way to investigate the most favorable technology combinations. This eventually leads to reasonable decision-making.

The effectiveness indices are usually plotted with RDT&E cost simultaneously. RDT&E cost is a kind of counterpart of effectiveness because technology infusion would increase the RDT&E cost of the aircraft to mature and incorporate the technology [10]. In Ref. [10], the plot of effectiveness with RDT&E cost is called as technology frontier and it provides a Pareto front which shows non-dominated solutions with respect to the effectiveness and cost. A notional technology frontier plot is shown in Fig. 2.7, which is modified from Ref. [10]. Among the solutions that satisfy threshold line, three best solutions can be chosen from the Pareto front: best effectiveness solution, best investment solution, and best compromise solution.

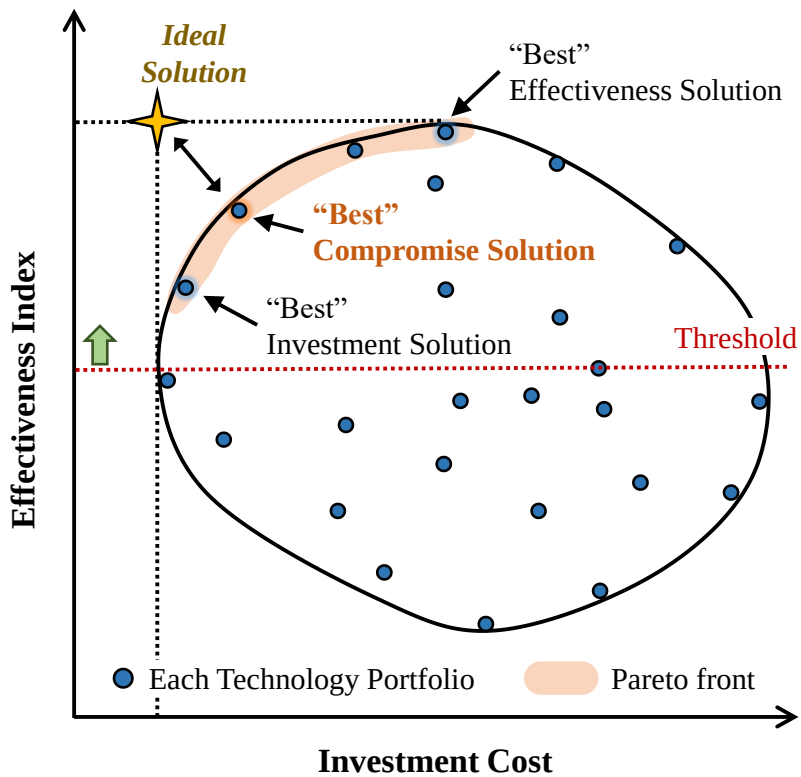

Fig. 2.7. Notional plot of effectiveness and investment cost

(Modified from Ref. [10])

2.2. Sizing Framework for Advanced Air Mobility

The conceptual sizing framework, named as Rotorcraft Initial Sizing and Performance Estimation Code and Toolkit+ (RISPECT+), is developed with colleagues to size advanced air mobility equipped with diverse propulsion systems [19]. The electrified propulsion systems that are modeled in RISPECT+ include series hybrid, parallel hybrid, series-parallel hybrid, and full-electric system. From geometric, aerodynamics, propulsion data, and specific mission requirements, the overall dimension, weight breakdown, and primary subsystem specification are obtained for the sized advanced air mobility meeting the mission requirements. The information of the sized aircraft includes energy capacity, maximum power of motors, lift to drag ratio, disk loading, and wing loading. In this section, primary modules that are constructing RISPECT+ structure are explained with focus on battery-based vertical take-off and landing aircraft. The detailed descriptions can be found in Ref. [19,20,45,46]. This sizing framework provides the aircraft modeling environment throughout this study.

2.2.1. Overall Process and Description

The overall design process of RISPECT+ is shown in Fig. 2.8 which is modified from Ref. [19] with the incorporation of technology factors and additional analysis modules: cost analysis and noise analysis. The sizing process is as follows.

1. With initial assumptions for gross weight and battery capacity, design variables, and parameters, the geometry of advanced air mobility is generated. Then, the sizing of the propulsion system in advanced air mobility is conducted based on a given mission profile. The propulsion system is sized to meet the most demanding flight condition in the mission profile.
2. Energy usage during the mission is calculated by Mission-analysis module, and then it is used for the weight calculation of the energy source. Except for the weight of the energy source, weights of other components such as structure compartments and systems are estimated in Weight-estimation module, producing empty weight.
3. By comparing the calculated empty weight, energy source weight with initially assumed gross weight, available payload, $W_{payload_{avail}}$, is calculated by Eq. (2.10) where W_{empty} is empty weight, W_{bat} is battery weight, and W_{fuel} is fuel weight. Superscript of 'new' is used to mean a newly calculated value.

$$W_{payload_{avail}} = GW_{init} - \left(W_{empty}^{new} + W_{bat}^{new} + W_{fuel}^{new}\right) \tag{2.10}$$

4. This process is iterated until the available payload becomes equal to the required payload by updating gross weight with Eq. (2.11) where α is a relaxation factor to control convergence characteristics.

$$GW^{new} = \alpha\left(W_{empty}^{new} + W_{bat}^{new} + W_{fuel}^{new} + W_{payload_{req}}\right) + (1-\alpha)GW^{old} \quad (2.11)$$

5. After convergence of gross weight, Cost analysis and Noise analysis are conducted separately based on the geometry of the sized advanced air mobility. Cost analysis produces vehicle cost and operating cost [47]. Noise analysis produces the maximum noise level index for hovering condition [48]. During the sizing process, the technology factors that are infused as input data are used in each related analysis module. The sizing process is terminated at this stage unless an optimizer is wrapped.
6. If the optimizer wraps the sizing module, optimization is carried out based on the user-customized problem. The optimal design of advanced air mobility is derived through optimization by changing design variables until design termination criteria such as the maximum number of evaluations or convergence tolerance are satisfied.

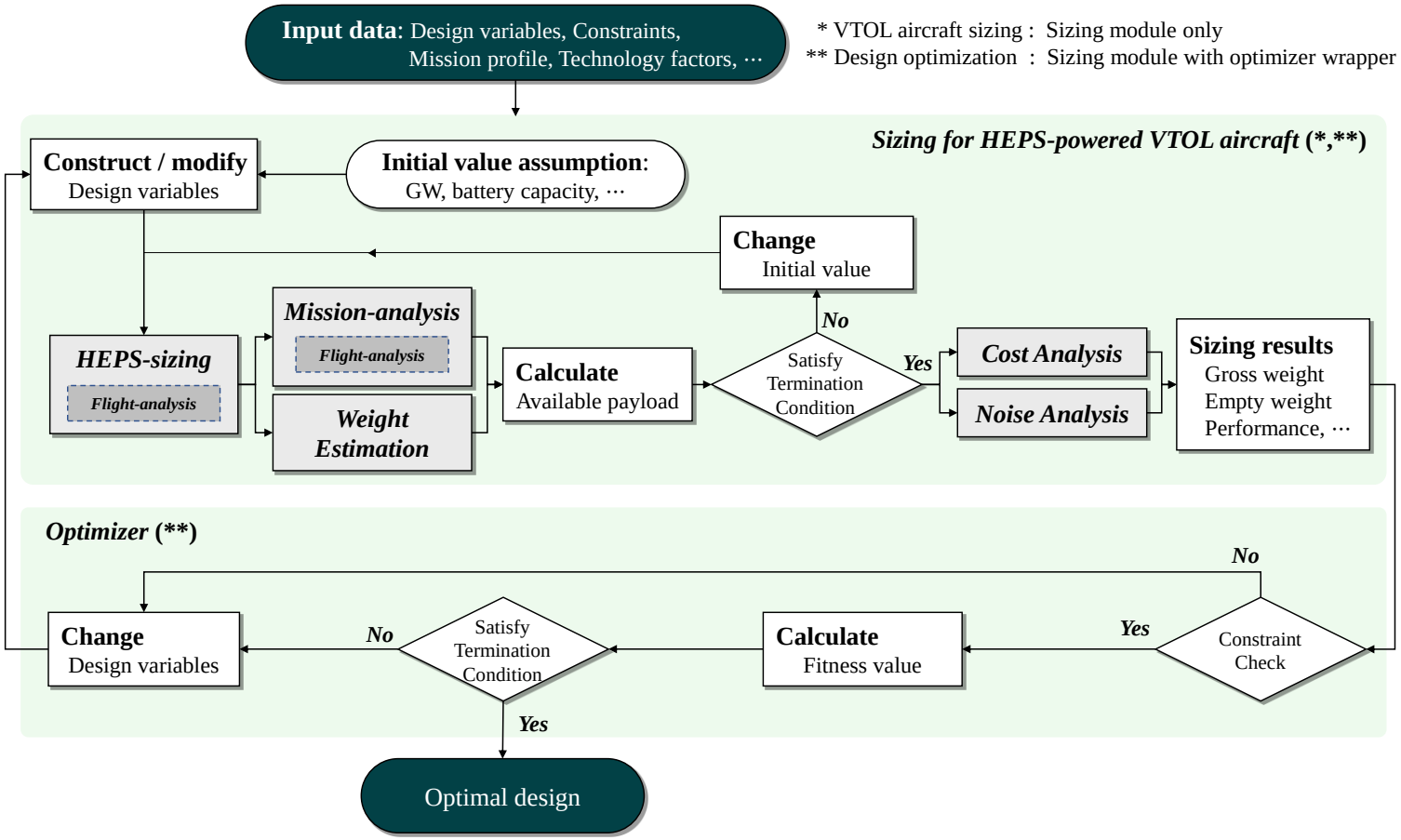

Fig. 2.8. Design process of RISPECT+ (Modified from Ref. [19])

2.2.2. Rotor Aerodynamic Model

A rotor blade is simply parametrized as shown in Fig. 2.9 for the aerodynamic analysis of a single rotor based on blade element theory (BET) [49,50]. r is nondimensionalized spanwise sectional location, c is chord length, β is twist angle, λ is local taper ratio, and tw is local twist variant. The number of split segments can be freely determined.

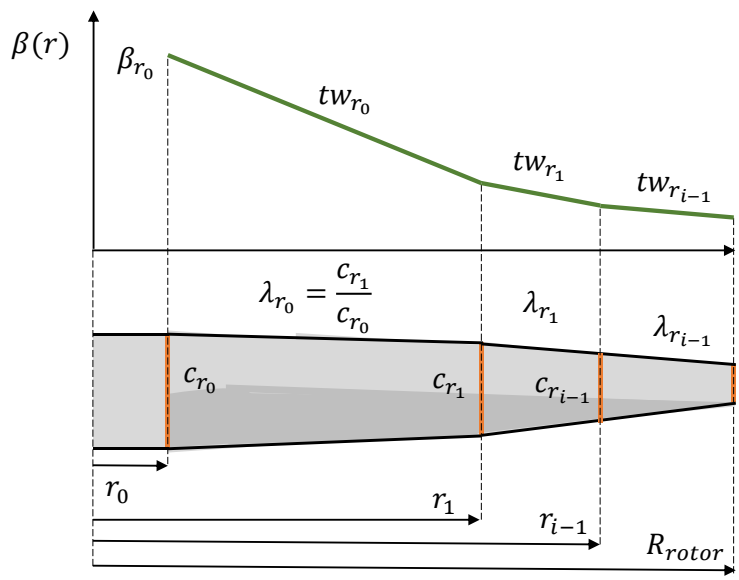

Fig. 2.9. Rotor blade parametrization for blade element theory

Rotor thrust, T_{rotor}, and power P_{rotor} is calculated by Eqs. (2.12) and (2.13), respectively.

$$\begin{aligned} T_{rotor} &= N_b \cdot \int (dL_b \cdot cos\,\phi_b - dD_b \cdot sin\,\phi_b) \\ &= \rho_{air} \cdot A \cdot V_{tip}^2 \cdot \frac{1}{2} \int_{r_0}^{r_{tip}} \sigma_R \cdot r\sqrt{\lambda^2 + r^2} \cdot \left(C_{l_b} - \frac{C_{d_b} \cdot \lambda}{r} \right) dr \end{aligned} \tag{2.12}$$

$$\begin{aligned} P_{rotor} &= N_b \cdot \int (dL_b \cdot sin\,\phi_b + dD_b \cdot cos\,\phi_b) \cdot \Omega_{rotor} y \\ &= \rho_{air} \cdot A \cdot V_{tip}^3 \cdot \frac{1}{2} \int_{r_0}^{r_{tip}} \sigma_R \cdot r\sqrt{\lambda^2 + r^2} \cdot \left(C_{l_b} \cdot \lambda + C_{d_b} r \right) dr \end{aligned} \tag{2.13}$$

ρ_{air} is air density, N_b is the number of rotor blades, ϕ is the induced angle of attack, A is the disk area, V_tip is the rotor blade tip speed, σ_R is the solidity, λ is the inflow velocity ratio, C_{l_b} is the lift coefficient, and C_{d_b} is the drag coefficient of blade airfoil. In axial flow conditions, λ is calculated using the blade element momentum theory (BEMT) with 3D stall-delay model [49–51]. If the inflow is much smaller than the tangential velocity of blade element $(\lambda \ll r)$, λ can be calculated by Eq. (2.14).

$$\lambda(r, \lambda_c) = \sqrt{\left(\frac{\sigma_R \cdot C_{l_\alpha}}{16F} - \frac{\lambda_c}{2} \right)^2 + \frac{\sigma_R \cdot C_{l_\alpha}}{8F} \cdot \theta \cdot r} - \left(\frac{\sigma_R \cdot C_{l_\alpha}}{16F} - \frac{\lambda_c}{2} \right) \tag{2.14}$$

where C_{l_α} is the slope of the 2D lift coefficient curve of blade airfoil, F is the Prandtl's tip loss factor, θ is the collective pitch angle, λ_c is the climbing velocity

ratio. In non-axial flow conditions, the rotor aerodynamic analysis is carried out based on the blade element theory with the linear inflow model [49].

Thrust coefficient C_T and power coefficient C_P are defined as Eqs. (2.15) and (2.16), respectively.

$$C_T = \frac{T_{rotor}}{\rho_{air} \cdot A \cdot V_{tip}^2} \tag{2.15}$$

$$C_P = \frac{P_{rotor}}{\rho_{air} \cdot A \cdot V_{tip}^3} \tag{2.16}$$

Figure of merit, an index of hover efficiency, is calculated using Eq. (2.17)

$$FM = \frac{C_{P_{ideal}}}{C_P} = \frac{C_T^{1.5}}{\sqrt{2} \cdot C_P} \tag{2.17}$$

Rotor aerodynamic model is validated for XV-15 rotor geometry by comparing the calculation result with wind-tunnel data and CFD analyses. The geometry information and reference data are collected from Ref. [52–54]. The comparison result for hover mode is shown in Fig. 2.10, and for tilt mode is shown in Fig. 2.11.

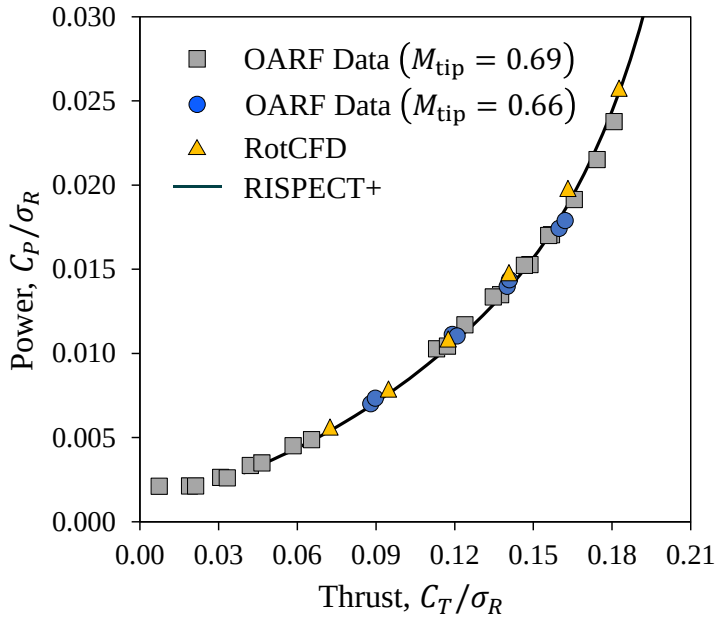

Fig. 2.10. Comparison of XV-15 rotor in hover (Reproduced from Ref. [19])

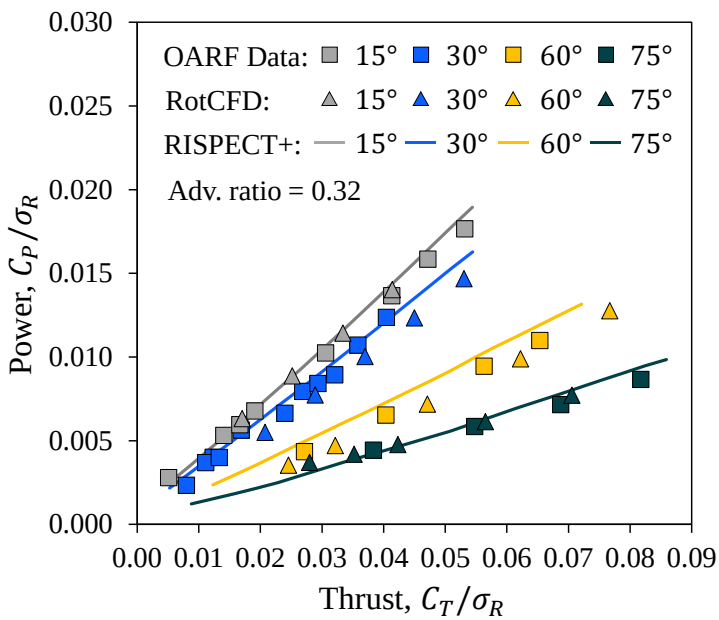

Fig. 2.11. Comparison of XV-15 rotor in tilt mode (Reproduced from Ref. [19])

2.2.3. Wing and Fuselage Aerodynamic Model

Wing aerodynamic analysis is carried out using an aerodynamic coefficient of 2D airfoil, wing geometry, and Oswald factor. 3D lift curve slope for an arbitrary wing, C_{L_α}, is obtained by Eq. (2.18) [3,55]. AR is aspect ratio, β is Prandtl-Glauert parameter which is equal to $(1-M^2)^{0.5}$ where M is Mach number, κ is ratio of 2D lift coefficient curve slope to 2π, and $\Lambda_{0.5c}$ is sweepback angle of mid-chord.

$$C_{L_\alpha} = \frac{C_{l_\alpha}}{1+\frac{C_{l_\alpha}}{\pi \cdot AR}(1+\tau)} \approx \frac{2\pi \cdot AR}{2+\sqrt{\left(\frac{AR\cdot\beta}{\kappa}\right)^2\left(1+\frac{\tan\Lambda_{0.5c}}{\beta^2}\right)+4}} \tag{2.18}$$

Drag coefficient, C_D, is expressed by Eq. (2.19) where C_L is lift coefficient, and e is Oswald factor which accounts for deviation from an ideal elliptical lift distribution.

$$C_D = C_{D_0} + C_{D_i} = C_{D_0} + \frac{C_L^2}{\pi \cdot e \cdot AR_w} \tag{2.19}$$

Oswald factor in this study is calculated following Ref. [56] and expressed by Eq. (2.20) [56] where e_{theo} is a theoretical Oswald factor, $k_{e,F}$ is a correction coefficient for fuselage influence, k_{e,D_0} is a correction coefficient for zero lift drag influence, and $k_{e,M}$ is a correction coefficient for Mach number influence.

$$e = e_{theo} \cdot k_{e,F} \cdot k_{e,D_0} \cdot k_{e,M} \tag{2.20}$$

Using Eqs. (2.18), (2.19), and (2.20), aerodynamic analysis of wing component such as main wing and horizontal wing is carried out.

Aerodynamic analysis of other components such as a fuselage, landing gear, hub, and etc. is focused on drag force using the concept of equivalent flat plat area, f, defined as production of drag coefficient and reference area, S_{ref} (Eq. (2.21)).

$$f = C_D \cdot S_{ref} = \frac{Drag}{0.5 \cdot \rho_{air} \cdot V_\infty^2} \tag{2.21}$$

The equivalent flat plate area can be obtained by computational fluid dynamics analysis or empirical formula. The empirical formula is the function of gross weight (Eq. (2.22)) and is shown in Fig. 2.12 [57]. Co_f is coefficient depending on the aircraft category. A similar approach is also presented in Ref. [49].

$$f = Co_f \left(\frac{GW}{1000}\right)^{2/3} \quad [ft^2] \tag{2.22}$$

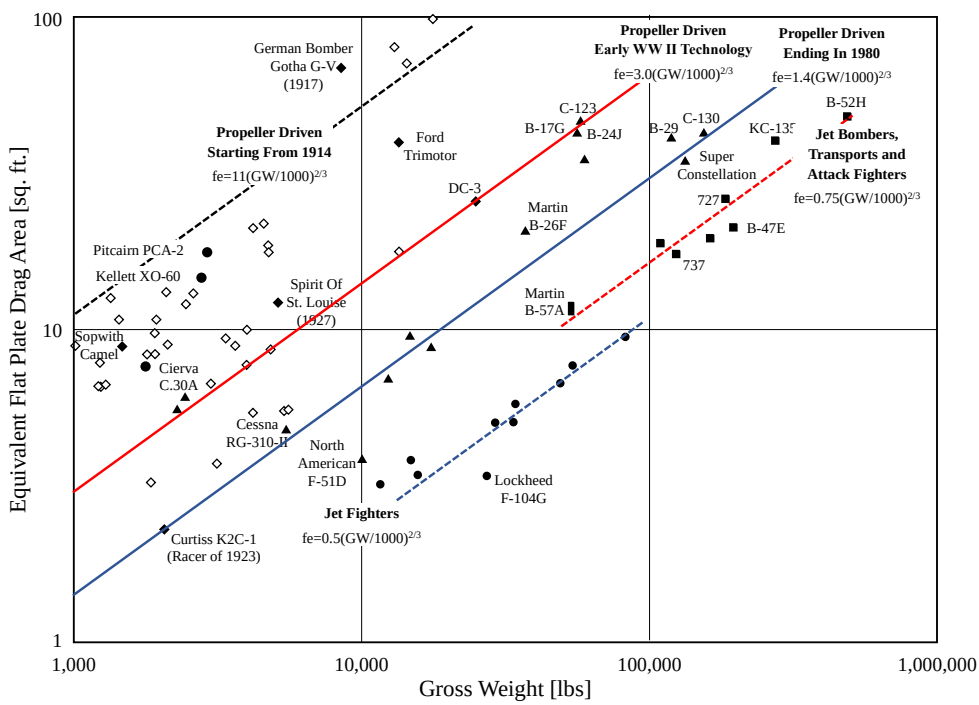

Fig. 2.12. Equivalent flat plate area trend history (Reproduced from Ref. [57])

If advanced air mobility has tilting systems, the additional drag from the tilting nacelle should be added. In Ref. [58], the mathematical equation for tilt nacelle drag is used for conversion mode in phase 1 of development in XV-15, which is shown in Eq. (2.23). In order to apply the equation to advanced air mobility sizing, a correction factor, κ_{tech}, is adopted. The value of 0.5 was assumed to be used for the correction factor in this study with consideration of highly improved compactness of nacelle in advanced air mobility compared to the conventional tilt rotor, XV-15. α_{tilt} is the tilt angle of the nacelle in radians of which the value of 0 is for horizontally fully tilted and the value of $\pi/2$ is for vertical position.

$$f_{nacelle} = (1 - \kappa_{tech}) \cdot \left(1 + 13.5 \cdot cos^6\left(\frac{\pi}{2} - \alpha_{tilt}\right)\right) \tag{2.23}$$

2.2.4. Electric Propulsion System Sizing Model

The descriptions for the electric propulsion system (EPS) sizing module are focused on the full-electric propulsion system architecture where the battery, electric motor, inverter, and thermal management system (TMS) constitute the overall propulsion system. Descriptions of additional components for other electrified propulsion architectures such as turbo-electric, series hybrid, parallel hybrid, and series-parallel hybrid systems can be found in Ref. [19,20,45].

The analysis fidelity of the electric propulsion system in RISPECT+ is stratified into two levels. The low-level-fidelity method is based on using constant efficiency for each electric component during a flight mission [19]. The battery is modeled as a black box containing energy, so called as “energy in a box”. This method is the simplest and quickest way to incorporate electric propulsion into advanced air mobility sizing in the conceptual design phase. It enables to size an advanced air mobility system under the minimum data environment which is the common situation in conceptual design.

The higher fidelity method is based on linear approximation in characteristics of battery [59] and equivalent circuits for electric motors [60] and inverters [61]. Reference [21] described the second method incorporated in RISEPCT+ in detail. Although this method enables more sophisticated analysis in the electric propulsion system, more specific data and assumptions are required to model the electric components and calculation time is increased, which is a kind of counterpart for pursuing higher fidelity.

In this study, the efficiencies of the electric components are treated as a constant (low-fidelity model) to focus on a demonstration for application of the proposed portfolio assessment process and uncertainty assessment with manageable computational time. Thus, the following paragraphs are presenting the low-fidelity model.

Battery

As a container of electric energy for energy sources in advanced air mobility, rechargeable batteries or secondary batteries are usually used. There are a lot of battery chemical compositions for them, lithium-based batteries called as lithium-ion batteries are the most commonly selected type for them. Depending on materials for cathode in lithium battery cells, the characteristics of lithium battery such as nominal cell voltage, discharge profile trend, specific power and specific energy are totally different.

In the method of "energy in a box", the required parameters for battery sizing are the efficiency coefficient, maximum depth of discharge (DoD), maximum discharge C-rate, and specific energy of the battery. Battery efficiency is usually in the range of 91~97% depending on operating conditions [21,29,62]. The DoD indicates the percent of battery used energy relative to the rated energy of the battery; 0.2 of DoD means 20% of battery energy is used and 80% of energy is remaining. The DoD has a relation with state of charge (SoC) as Eq. (2.24). Usually, the maximum DoD, DoD_{max} is constrained as 0.8 for battery life-cycle and operation safety.

$$DoD = 1 - SoC \tag{2.24}$$

Discharge C-rate is a rate of discharge in battery cells, which expresses the discharge current relative to the current required to discharge the cell in one hour [63]. This is mathematized as Eq. (2.25) where χ_{bat} is discharge C-rate, $P_{bat_{\text{out}}}$ is output power from battery, η_{bat} is battery efficiency, and E_{bat} is battery energy.

$$\chi_{bat} = \frac{I_{bat}}{Capa_{bat}} = \frac{P_{bat}}{E_{bat}} = \frac{P_{bat_{out}}}{\eta_{bat} \cdot E_{bat}} \tag{2.25}$$

The required battery energy is determined by comparing two values that are calculated using maximum DoD and discharge C-rate, respectively. The first criterion is calculated on the basis of maximum DoD by Eq. (2.26) where the accumulated battery usage required for the mission, equal to the production of power and time Δt, is divided by maximum DoD. If battery efficiency is not constant, it should be calculated inside of Sigma notation.

$$E_{bat}|_{DoD} = \frac{\sum E_{bat_i}}{DoD_{max}} = \frac{\sum P_{bat_{out}} \cdot \Delta t}{\eta_{bat} \cdot DoD_{max}} \tag{2.26}$$

The second criterion is obtained by the basis of the maximum C-rate by Eq. (2.27) where the maximum output power of the battery is divided by maximum C-rate. This criterion determines the minimum battery energy satisfying the C-rate constraint.

$$E_{bat}|_{\chi} = \frac{P_{bat_{out_{max}}}}{\eta_{bat} \cdot \chi_{bat_{max}}} \tag{2.27}$$

The final battery energy is the bigger value between the two criteria (Eq. (2.28))

$$E_{bat} = max\left(E_{bat}|_{DoD},\ E_{bat}|_{\chi}\right) \tag{2.28}$$

After obtaining battery energy, battery weight is calculated by Eq. (2.29) where W_{bat} is battery energy and SE_{bat} is specific energy. SE_{bat} of lithium-series batteries have variability depending on their chemistry composition (Fig. 2.13 [64]). For advanced air mobility sizing, specific energy in the range of 180 ~ 500 Wh/kg is usually used [19,26,29,59,62,63,65].

$$W_{bat} = \frac{E_{bat}}{SE_{bat}} \tag{2.29}$$

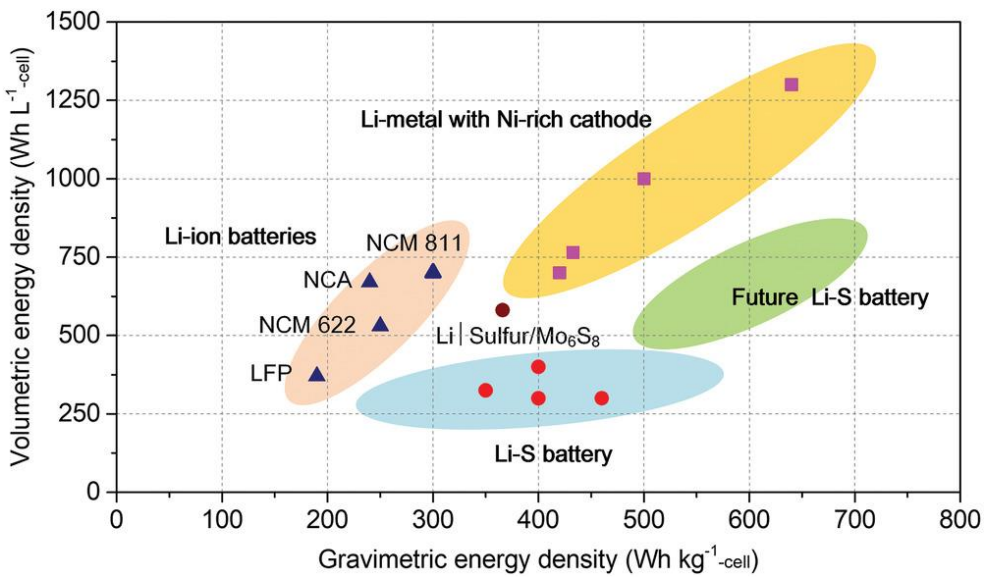

Fig. 2.13. Comparison of lithium batteries depending on chemistry [64]

Electric Motor

For the electric propulsion system, electric motors drive a shaft of the propulsor (rotor, and propeller) to generate the required thrust for aviation by changing electric power to mechanical power. Target mechanical power is calculated by Eq. (2.13). One of the most significant characteristics required for electric motors for aviation is higher specific power than ever. Among various types of electric motors, permanent-magnet synchronous motors have got the spotlight for an available solution [66,67]. They show high efficiency, specific power, robustness, and ease of maintenance. In many studies for advanced air mobility sizing, constant efficiency is usually set around 95% or over in the case of future aircraft [26,29,62,63,65].

The specific power of electric motors, defined as maximum power per weight, is a representative performance index of electric motors. The range of specific power of electric motors that are currently under development or were developed for aviation applications is shown in Table 2.1. The data were collected from presentation material [68], manufacturer's websites, and official documents [69]. In the studies of future aircraft, much higher values of specific power that is near to the goal of roadmaps are used [29,62]

Table 2.1. Specification of electric motors for aviation application

Manufacturer	Model	Efficiency	Specific power [kW/kg]
Siemens [68]	SP2000D	-	7.6 (target)
	SP260D-0	0.95	5.2
MagniX*	Magni350	> 0.93	3.14
	Magni650	> 0.93	3.2
EMRAX†	EMRAX 188	0.92~0.98	4.0
	EMRAX 208	0.92~0.98	4.4
	EMRAX 268	0.92~0.98	5.27
	EMRAX 348	0.92~0.98	5.0
Pipistrel [69]	E-811	-	2.17

Electric motor weight is obtained using the efficiency and specific power of electric motors as Eq. (2.30) where W_{mot} is motor weight, $P_{mot_{out_{max}}}$ is maximum output power from motors, η_{mot} is motor efficiency, and SP_{mot} is the specific power of electric motors.

$$W_{mot} = \frac{P_{mot_{out_{max}}}}{\eta_{mot} \cdot SP_{mot}} \tag{2.30}$$

* https://www.magnix.aero/services

† https://emrax.com/e-motors/

Inverter and controller

Inverters provide alternating current to electric motors by converting direct current from batteries to operate the electric motors in the required power and torque condition. For the class of advanced air mobility, IGBT inverters are usually used [63]. They control the rotational speed of the electric motors by various modulation schemes such as space vector pulse-width modulation. In general, inverters during typical operation show 95% of efficiency due to power losses caused by switching between the blocking state and conducting state, and by heat [29,63,70]. With advanced control modulation schemes, materials, and cooling systems, the losses can be significantly diminished, so that an efficiency over 95%, up to 98~99% is applied for sizing of advanced air mobility in many different studies [26,29,62,63,70,71]. The specific power of inverters, defined as maximum power per weight, is in the range of around 3-11 kW/kg [63] and values over 12 kW/kg was often used for advanced air mobility sizing [29,62].

Inverter weight is obtained using efficiency and specific power of inverters as Eq. (2.31) where W_{inv} is inverter weight, $P_{inv_{out_{max}}}$ is maximum output power from inverters, η_{inv} is inverter efficiency, and SP_{inv} is specific power of inverters.

$$W_{inv} = \frac{P_{inv_{out_{max}}}}{\eta_{inv} \cdot SP_{inv}} \tag{2.31}$$

Thermal Management System

Thermal management system (TMS) herein indicates a kind of compound system to handle heat generated from the battery, electric motors, and inverters without explicitly distinguishing their own cooling mechanisms. To this end, it is assumed that all power losses occurring from each component are converted to heat and TMS capacity is equal to them. Thus, the maximum power of TMS, $P_{TMS_{max}}$, is defined as the sum the maximum power losses of the electric components (Eq. (2.32)). The weight of TMS, W_{TMS}, is obtained as $P_{TMS_{max}}$ divided by the specific power of TMS, SP_{TMS}. (Eq. (2.33)).

$$P_{TMS_{max}} = \sum \{(1 - \eta_{comp}) \cdot P_{comp_{max}}\} \tag{2.32}$$

$$W_{TMS} = \frac{P_{TMS_{max}}}{SP_{TMS}} \tag{2.33}$$

2.2.5. Weight Estimation Model

Weight estimation model for advanced air mobility in RISPECT+ is based on semi-empirical methods that were constructed with geometry and performance indices.

The structure group comprises of the rotor, propeller, fuselage, wing, empennages, supporting rod, tilting actuator, and landing gear. Most equations are given by Raymer [3], US army report [72], and NDARC [73] that are presented as follows. The application of the weight equations is dependent on a configuration of advanced air mobility. For instance, tilting actuator weight is added only for a vectored thrust configuration. The equations are based on English unit system.

Rotor (Propeller)

Weight of a rotor, W_{rotor}, is obtained by Eq. (2.34) where T_{max} is maximum thrust, A is disk area, and κ_{tech} is correction factor for advanced technologies.

$$W_{rotor} = (1 - \kappa_{tech}) \cdot 0.08094 \cdot T_{max}^{1.0477} \cdot (T_{max}/A)^{-0.07821} \tag{2.34}$$

Fuselage

Weight of a fuselage, $\mathrm{W_{fuse}}$, is obtained by Eq. (2.35) where N_z is load factor, GW is gross weight, R_{rotor} is rotor radius, and N_{rotor} is the number of rotors.

$$W_{fuse} = (1 - \kappa_{tech}) \cdot 0.02665 \cdot (N_z \cdot GW)^{0.943} \cdot \left(R_{rotor} \cdot \frac{N_{rotor}}{2}\right)^{0.654} \tag{2.35}$$

Wing

Weight of a main wing, W_{wing}, is obtained by Eq. (2.36) where S_w is wing area, λ_w is taper ratio, AR_w is aspect ratio, and $\mathrm{t/c}$ is maximum airfoil thickness.

$$W_{wing} = (1-\kappa_{tech}) \cdot 0.032 \cdot S_w^{0.758} \cdot \lambda_w^{0.04} \cdot (N_z \cdot GW)^{0.49} \cdot \left(\frac{AR_w}{cos^2(\Lambda_w)}\right)^{0.6} \cdot \left(\frac{100}{cos(\Lambda_w)}\frac{t}{c}\right)^{-0.3} \tag{2.36}$$

If the configuration of advanced air mobility is vectored thrust (tilt rotor), weight equation for the main wing is changed by Eq. (2.37) [74]. Note that SI unit should be used for Eq. (2.37).

$$W_{wing} = (1-\kappa_{tech}) \cdot 0.0288 \cdot (1+0.12 \cdot \tau^{0.4}) \cdot \left(N_z \cdot \frac{GW}{S_w}\right)^{0.52} \cdot S_w^{1.22} \cdot AR_w^{0.47} \cdot \left(\frac{2}{(t/c)}\right)^{0.4} \cdot \left(1.1+\frac{\lambda_w}{2}\right)^{0.695} \tag{2.37}$$

Empennage

Empennages are for a horizontal tail and vertical tail. Their weight is obtained by Eqs. (2.38) and (2.39), respectively. S is area, and AR is aspect ratio.

Horizontal tail $$W_{ht} = (1-\kappa_{tech}) \cdot 0.7176 \cdot S_{ht}^{1.2} \cdot AR_{ht}^{0.32} \tag{2.38}$$

Vertical tail $$W_{vt} = (1-\kappa_{tech}) \cdot 1.046 \cdot S_{vt}^{0.94} \cdot AR_{vt}^{0.53} \tag{2.39}$$

Supporting rod

Weight of supporting rods, W_{rod}, is obtained by Eq. (2.40) where N_{rod} is the number of rods, ρ_{rod} is rod material density, L_{rod} is rod length, R_{rod} is rod radius, and t_{rod} is rod thickness.

$$W_{rod} = N_{rod} \cdot \rho_{rod} \cdot L_{rod} \cdot \pi\left(R_{rod}^2 - (R_{rod} - t_{rod})^2\right) \tag{2.40}$$

Tilting actuator

Weight of tilting actuators, W_{tilt}, is obtained by Eq. (2.41) that is derived from XV-15 and MV-22 data [75]. N_{tilt} is the number of tilting actuators.

$$W_{tilt} = 0.005 \cdot GW \cdot N_{tilt} \tag{2.41}$$

Landing gear

Weight of a landing gear, W_{LG}, is obtained by Eqs. (2.42) and (2.43) depending on the type of landing gear.

Skid type $$W_{LG} = 0.44 \cdot (GW)^{0.63} \tag{2.42}$$

Wheel type landing gear $$W_{LG} = 0.038 \cdot GW \tag{2.43}$$

The propulsion group comprises of battery, electric motors, inverters, TMS, extra circuit protection, and wiring. The weight of the battery, electric motors, inverters, and TMS are obtained by Eqs. (2.29), (2.30), (2.31), and (2.33), respectively. Weights of extra circuit protection and wiring are assumed to be proportional to the weight of the total electric propulsion system as Eqs. (2.44) and (2.45), respectively.

$$W_{circuit} = 0.0084 \cdot W_{EPS} \tag{2.44}$$

$$W_{wiring} = 0.1361 \cdot W_{EPS} \tag{2.45}$$

For the weight of other systems such as flight control systems and furnishing equipment are calculated by equations presented in Ref. [3,72,73] or customized values can be imposed.

The technology correction factors κ_{tech} in several equations is assumed following Ref. [76]. The validation results of the weight estimation model are presented in Ref. [19] for XV-15 data [77] and a hypothetical lift-plus-cruise type eVTOL [76].

2.2.6. Cost Estimation Model

Cost estimation model was coupled with RISPECT+ in order to analyze economics of advanced air mobility, which is especially necessary to address the infusion of new technologies in Section 2.1. The costs of aircraft can be divided into two categories: vehicle cost (Acquisition cost), and operating cost. They are estimated by an in-house tool called as Aircraft Cost Analysis Code (AC^2) [47]. AC^2 was developed with colleagues to estimate economic quantities for generalized advanced air mobility focusing on wing-borne configurations. As of now, this cost estimation model is restricted to wing-borne configurations: vectored thrust and lift-plus-cruise. Additional cares should be taken to use AC^2 for wingless configurations. A detailed description for acquisition cost estimation method can be found in Ref. [47].

Vehicle Cost (Acquisition Cost)

In AC^2, vehicle cost, which is also referred to as acquisition cost, is estimated by using a top-down and bottom-up hybrid approaches. The overall structure of vehicle cost estimation is shown in Fig. 2.14 [47]. A wing-borne configuration of advanced air mobility can be decomposed into three compartments: the base structure, additional airframe, and subpart component.

The base structure stands for a typical aircraft structure in which a single fuselage, a single main wing, empennages, and landing gear constitute the structure. The base structure cost, C_{base}, is estimated based on DAPCA IV method [78] which is mainly

based on the top-down approach using functions of gross weight, number of prototypes, and learning curve. Since most advanced air mobility under currently development have size and dimension similar with general aviation aircraft, DAPCA IV method can be applied. DAPCA IV produces base structure cost that includes RDT&E cost.

The additional airframe stands for auxiliary body components such as the secondary wing in Kitty Hawk Heaviside, and rotor supporting rod in Wisk Cora or Beta Technology Alia 250. The cost of an additional airframe, $C_{add.frame}$, is estimated using equations presented in Ref. [79] where the aircraft is decomposed into 17 parts and the cost of each part was estimated separately. For consideration of more complex configuration of advanced air mobility than general aviation, the adjustment factor, f_{ad}, is derived using data from the tables and figures in Ref. [80]. The adjustment factor depends on the type of aircraft configuration (vectored thrust, and lift-plus-cruise). Due to more complexity, such as a vectoring system, the adjustment factor for vectored thrust configuration is greater than that for lift-plus-cruise configuration. The adjustment factor is multiplied to the base structure cost and additional airframe cost.

The subpart component basically stands for the other components except for the airframe structures. It includes the propulsion system including the rotor, propeller, battery, electric motor, inverter, and so on. For the cost of the propulsion system, a method presented previously is leveraged in this study. Finger et al. [81] presented a cost estimation method for hybrid electric general aviation aircraft. In the method,

they estimated the cost of electric propulsion using unit cost per component power for the motor (Eq. (2.46)) and inverter (Eq. (2.47)) or unit cost per energy for battery (Eq. (2.48)). Rotor cost is estimated by Eq. (2.49), a function of the rotor dimension and power capability. Avionics cost is simply estimated by Eq. (2.50).

$$C_{mot} = N_{mot} \cdot C_{mot_{unit}} \cdot P_{mot_{max}} \tag{2.46}$$

$$C_{inv} = N_{inv} \cdot C_{inv_{unit}} \cdot P_{inv_{max}} \tag{2.47}$$

$$C_{bat} = C_{bat_{unit}} \cdot E_{bat} \tag{2.48}$$

$$C_{rotor} = N_{rotor} \cdot C_{rotor_{unit}} \cdot (2R_{rotor})^2 \cdot \left(\frac{P_{rotor_{max}}}{2R_{rotor}}\right)^{0.12} \tag{2.49}$$

$$C_{avionics} = C_{avionics_{unit}} \cdot W_{avionics} \tag{2.50}$$

The approach in the calculation of the additional airframe cost and subpart cost is a kind of bottom-up approach from the component to the aircraft system. By summing up the three compartments' costs after the application of the adjustment factor, the final vehicle cost of advanced air mobility, $C_{vehicle}$, is obtained as Eq. (2.51).

The key parameter values used for vehicle cost estimation in this study are given in Table 2.2. The number of prototypes and the number of production quantities in 5 years are the input parameters for the calculation of the base structure cost.

$$C_{vehicle} = f_{ad}\left(C_{base} + C_{add.frame}\right) + \sum C_{subparts} \tag{2.51}$$

Table 2.2. Key parameter values used in vehicle cost estimation

Parameter	Value
Number of prototypes	5
Number of production quantities in 5 years	250
Adjustment factors for vectored thrust | lift-plus-cruise	3.30 | 1.85
Rotor cost coefficient per unit	$210
Electric motor cost per unit power	$63 per hp
Inverter cost per unit power	$44 per hp
Battery cost per unit energy capacity	$300 per kWh
Avionics cost per unit weight	$6,000 per lb

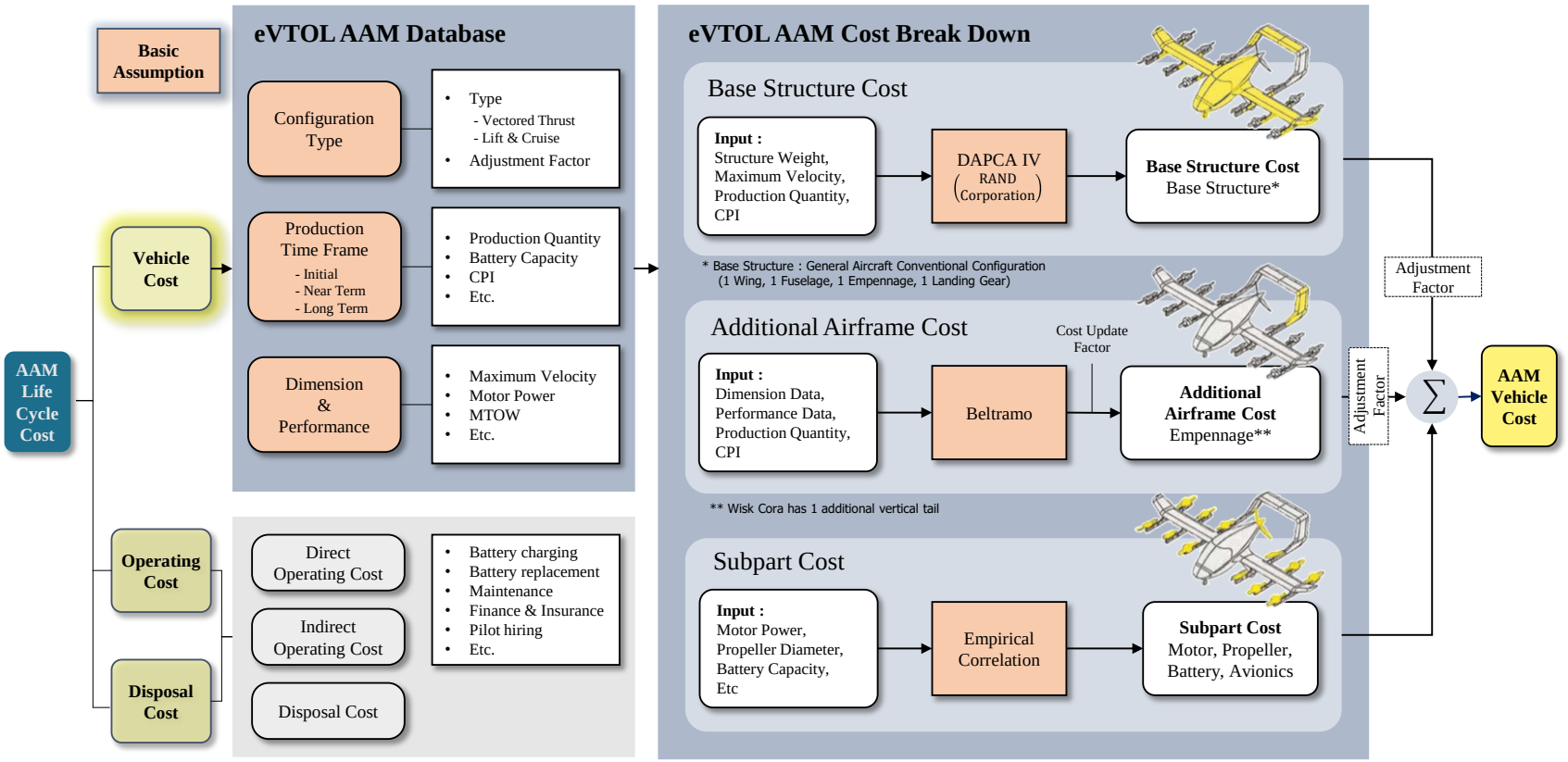

Fig. 2.14. Vehicle cost estimation in AC^2 (Modified from Ref. [47])

Direct operating Cost

Direct operating cost (DOC) is subdivided into several elements including maintenance, depreciation, finance, insurance, battery replacement, charging cost, and pilot [82]. The information of them is obtained from historical data, technical factors, and assumptions used in presentations from eVTOL manufacturers[*,†,‡]. For the maintenance cost of advanced air mobility, the near-term goal for helicopter maintenance cost presented in Ref. [57] is modified as Eq. (2.52) considering the exclusion of the engine. The correction factors, 0.7767 and 0.4893, are derived from the data of two different helicopters: the S-55 and the S-61 [57].

$$C_{DOC_{mnt}} = C_{DOC_{lab}} \cdot 0.7767 \cdot \left[0.0017 \cdot \left(W_{empty}\right)^{0.78+0.3+0.1}\right] \; for\ Labor$$
$$+ 0.4893 \cdot 34 \cdot \left[\frac{C_{vehicle}}{10^6}\right]^{0.68} \qquad for\ Parts \tag{2.52}$$
$$+ 18 \cdot \left(\frac{C_{vehicle}}{10^6}\right) \qquad for\ Major\ Periodic\ Maint.$$

Battery replacement cost is estimated by Eq. (2.53) [82].

$$C_{bat_{replace}} = \frac{C_{bat}}{LC_{bat}} \cdot \bar{\chi}_{bat} \tag{2.53}$$

---

[*]. Joby Aviation, Analyst Day presentation, https://ir.jobyaviation.com/about-us/presentations (accessed at 2021.10.)

[†]. Lilium, Capital Markets Day presentation, https://ir.lilium.com/news-and-events/events-and-presentations (accessed at 2021.10.)

[‡]. Vertical Aerospace, Analyst presentation, https://investor.vertical-aerospace.com/events-and-presentations/presentations/default.aspx (accessed at 2021.11.)

$\bar{\chi}_{bat}$ is averaged battery discharge C-rate and LC_{bat} is battery usable discharge cycle calculated by Eq. (2.54) [82].

$$LC_{bat} = (-152 \cdot log\bar{\chi}_{bat} + 533.54) \cdot (1.3 \cdot DoD_{max}^{-0.195}) \quad (2.54)$$

The key parameter values used for operating cost estimation in this study are given in Table 2.3.

Table 2.3. Key parameter values used in operating cost estimation

Parameter	Value
Number of flights per a day	54
Pilot rate	$114 per FH
Finance and insurance rate per vehicle cost	4% and 3.115%
Landing fee	$35 per landing
Parking rate	$1.5 per FH
Weather and communication service	$2.26 per FH

The specifications of the vehicle such as component weight and energy capacity required for AC^2 were fed from RISPECT+.

2.2.7. Noise Model

Simplified vehicle noise model for rotorcraft is coupled with RISPECT+. The coupled noise model was developed by Ref. [48], and it focuses on rotor noise in axial flight in which an order of higher thrust is required than in wing-borne flight. This noise model enables to quickly incorporate noise performance in system-level conceptual design and to present direction of major design properties. This section describes the main equations for the noise model. The details can be found in Ref. [48] including assumptions and limitations of the noise model.

Rotational Noise

One of the two components of rotor noise without blade slap is rotational noise which is also referred to as harmonic noise. Rotational noise can be divided into two categories: loading noise, caused by thrust generation; and thickness noise, caused by finite blade thickness. The root mean square sound pressure for loading noise, p_{m_L}, and thickness noise, p_{m_T}, can be modeled by the Gutin and Deming formula [83]. They are simplified using equivalent-radius R_e as Eqs (2.55) and (2.56), respectively. The resultant sound pressure level (SPL) is obtained by Eq. (2.57).

$$p_{m_L} = \frac{mN_b\Omega}{2\sqrt{2}\pi a(\Delta S)}\left[T_t cos\theta - Q\frac{a}{\Omega R_e^2}\right]J_{mB}\left(\frac{mN_b\Omega}{a}R_e sin\theta\right) \tag{2.55}$$

$$p_{m_T} = \frac{-\rho_{air}(mN_b\Omega)^2 B}{3\sqrt{2}\pi(\Delta S)}c_b t_b R_e J_{mB}\left(\frac{mN_b\Omega}{a}R_e sin\theta\right) \tag{2.56}$$

$$SPL = 10\,log_{10}\left[N_{rotor}\left(\frac{p_{m_L}^2 + p_{m_T}^2}{p_{ref}^2}\right)\right] \tag{2.57}$$

In the equations, variables are defined as Table 2.4. The definitions of ΔS and θ are given in Fig. 2.15.

Table 2.4. Symbols for rotational noise equations

Symbol	Description	Symbol	Description
a	Speed of sound	Q	Rotor torque
c_b	Blade chord	t_b	Blade maximum thickness
J_{mB}	Bessel function of order mB	ΔS	Distance between the rotor and the observer
m	Harmonic number	Ω	Rotor angular velocity
N_{rotor}	Number of rotors	θ	Observer azimuthal angle

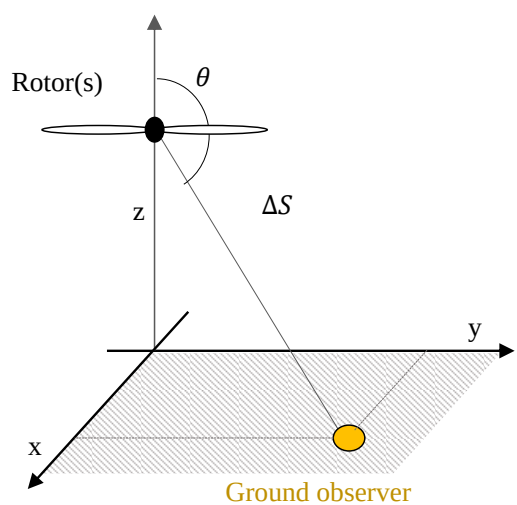

Fig. 2.15. Schematic diagram for rotational noise (Modified from Ref. [48])

Vortex Noise

The other component of rotor noise is vortex noise and SPL by vortex noise is calculated by Eq. (2.58) [48] where T_{rotor}/A is the disk loading, K_2 is a constant, equal to $1.206\,x\,10^{-2}\,s^3/ft^3$, and V_{tip} is blade tip speed.

$$SPL = 20\,log_{10}\left[K_2\frac{V_{tip}}{\rho_{air}(\Delta S)}\sqrt{\frac{N_{rotor}T_{rotor}}{\sigma_R}\left(\frac{T_{rotor}}{A}\right)}\right] \tag{2.58}$$

Equation (2.58) reflects the major parameters related to rotor noise such as tip speed, solidity, and disk loading of the rotor. For example, lowering tip speed results in low SPL, and higher disk loading results in high SPL. Equation (2.58) was validated in Ref. [48] based on data from Ref. [84] for two different helicopter rotors: the CH-3C and the CH-53A within a 3 dB difference compared to the test data.

A-Weighting Correction

Among various decibel weighting corrections by human responses at frequencies, A-weighting correction has been widely used. It is usually used for a regulatory guide such as in Uber Elevate [85] and representative index in noise comparison. The A-weighting response function, $A(f)$ as a function of frequency is plotted in Fig. 2.16 [48]. Although vortex noise is broadband noise, the frequency spectrum of vortex noise also can be modeled by Ref. [48,86], and A-weighting correction is carried out. The A-weighting response plot for vortex noise is also shown in Fig. 2.16.

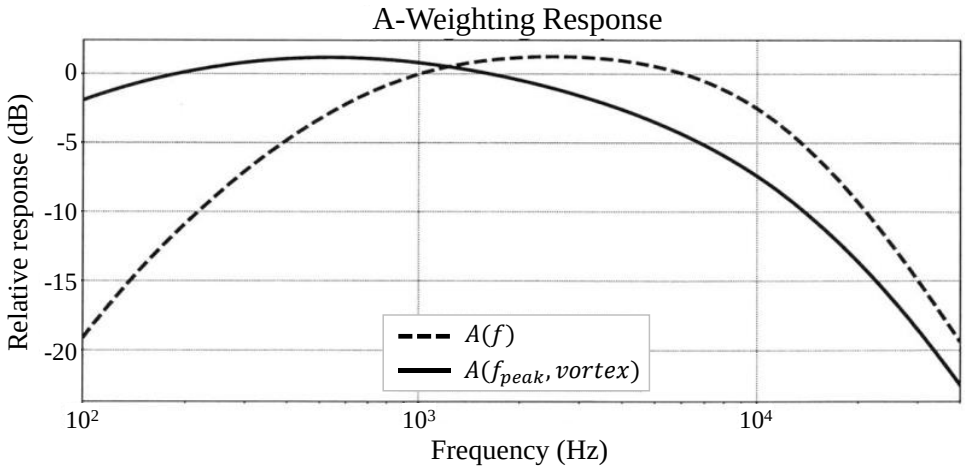

Fig. 2.16. A-weighting response function [48]

Chapter 3

Uncertainty Environment

The uncertainties occurring in the technology portfolio assessment and the sizing framework are diverse. The types of uncertainties and their source are described first, and specific uncertainties in the process are identified and modeled using various techniques. The categorization of uncertainties and terminology in this study is largely based on the method from Ref. [87].

3.1. Types of Uncertainties

A large number of researches have dealt with identifying and categorizing types of uncertainties that occur in science and engineering with computational modeling and analyses. The uncertainties change a deterministic problem in original to a non-deterministic problem resulting in that interpreting the outcomes becomes more complex and difficult. In order to efficiently handle the uncertainties and interpret the outcomes, the most effective categorizing method of uncertainties was developed by the risk assessment community. The method distinguishes uncertainties based on the fundamental nature of uncertainties.: aleatory and epistemic uncertainty [87]. This division increases the ease of interpretation of analysis results and helps to make strategies to handle uncertainties by decision-makers. Distinguishing uncertainties into aleatory and epistemic is widely used across a variety of research [16,27,39,88–92].

3.1.1. Aleatory Uncertainty

Aleatory uncertainty is defined as uncertainty due to inherent physical randomness in nature or a system. This type of uncertainty is also referred to as stochastic uncertainty, variability, and irreducible uncertainty because it is attributed to inherent variability in nature or system randomness that cannot be removed. The representative examples of this type of uncertainty include physical variations in product specification due to manufacturing tolerance, in material properties due to environmental circumstances, and in performance indices of subsystems (efficiency of powertrain). The computational parameters such as initial conditions and boundary conditions are also can be aleatory uncertainty.

This uncertainty is usually mathematically modeled using probability density functions (PDFs) and cumulative distribution functions (CDFs) based on numerous samples with an assumption about the shape of PDFs (Gaussian, uniform, Weibull, etc.) [88]. Notional PDF and CDF graphs are shown in Fig. 3.1.

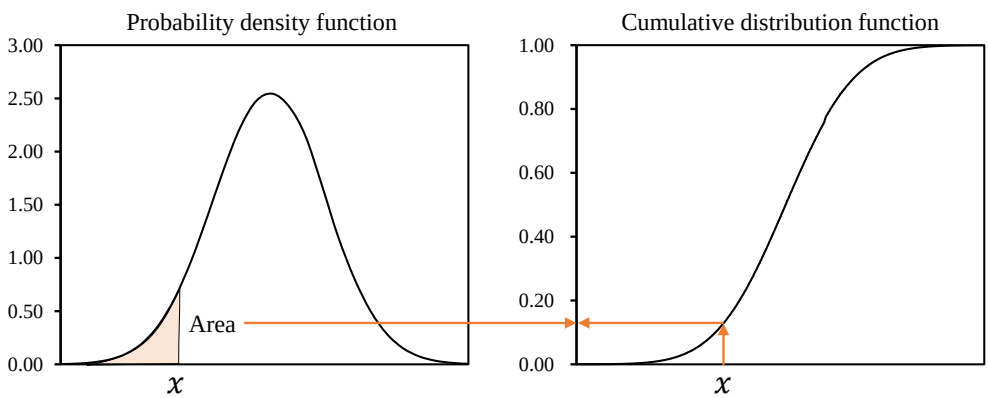

Fig. 3.1. Notional probability density function (left), and cumulative density function (right)

3.1.2. Epistemic Uncertainty

The other uncertainty, epistemic uncertainty, deals with the uncertainties arising from a “lack of knowledge”. “Lack of knowledge” can be caused by insufficient or incomplete data, assumptions in physics, and simplified mathematics model in computations. Since these uncertainties can be reduced with supplementary data and advancements in computational models, epistemic uncertainty is considered as reducible uncertainty. Although epistemic uncertainty is divided further into “recognized uncertainty” and “blind uncertainty”, the further division is not applied in this study.

As epistemic uncertainty is induced by the lack of knowledge related to computational modeling and mathematical modeling, the terminology of “model uncertainty” is simultaneously used in this study. Epistemic uncertainty should be considered especially in earlier design phases such as the pre-conceptual, and conceptual design phases where many mathematical models used in the analyses are simplified and have relatively lower accuracy. Thus, it is important to present outcomes obtained by probability-based analysis due to reducing the possibility of design failure or re-design attempts in the more mature design phases.

In order to embed the effect of epistemic uncertainty in system responses, it is ideal to know the exact distribution of the model uncertainty. However, it is usually an impractical situation because the number of available experimental data is usually limited owing to the limit of budget or timeframe. In that situation, unthoughtful use of PDFs with assumptions may lead to inaccurate predictions in the amount of

uncertainty in the system [87–90]. Thus, epistemic uncertainty is usually considered using intervals. The intervals can be obtained through various ways. One is a comparison with data from computational methods with higher accuracy or experimental data. If data from higher fidelity methods are not available, expertise from experts can help to set the intervals.

3.1.3. Other Uncertainties

In addition to both types of uncertainties, numerical errors arise during the computation process in science computing. The error is defined as a deviation from the true value of a quantity. In Ref. [87], the error is strictly different from the uncertainty and its usefulness of the concept of error is highly dependent on the level of accuracy of the true value. The concept of error is useful in the circumstance where the accuracy of the true value is known, which is not a usual situation though. In that case, it would be a more appropriate approach to characterize the accuracy of the computation as epistemically uncertain [87]. Thus, in this study, the numerical error is considered blindly in the model uncertainty

3.1.4. Effect of Uncertainties

The effects of the two types of uncertainties on an output quantity of interest are shown in Fig. 3.2. In an ideal case where there is no uncertainty with precise knowledge and no variability, a scalar quantity of interest is obtained. The sole aleatory uncertainty results in a distribution, producing a single CDF curve. The sole epistemic uncertainty makes a scalar value shifted, which produces a pure interval. When the two types of uncertainties are mixed together, the multiple CDF curves are generated, and probability area, referred to as a probability box or "p-box", is generated eventually.

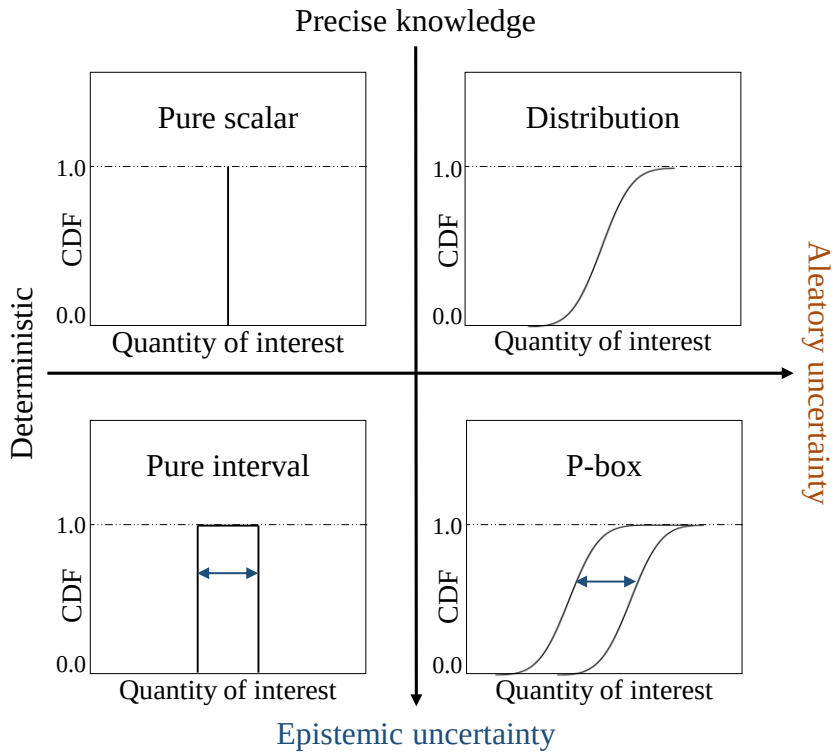

Fig. 3.2. Uncertainty effects on an output quantity of interest

(Modified from Ref. 34)

3.2. Uncertainties in Technology Portfolio Assessment Process

The uncertainties existing in the technology portfolio are identified and treated by following the classification of uncertainties described in Section 3.1.

3.2.1. Uncertainty in technology impact and interaction factor

One of the most major uncertainties is the magnitude of the impact of each technology on system attributes, and elements of TIM. As described earlier in Section 2.1.2, the impact factors for TIM can be quantified through various ways, such as literature reviews, physics-based computations, direct experiments, and the Delphi technique which relies on experts' opinions. Although uncertainties are attributed to each source, in particular, Delphi technique that depends on experts' opinions is one of the main sources of uncertainty. The subjectivity of the experts based on their own experience and confined knowledges only in their disciplines have significant contributions to the uncertainty for the impact factor. Thus, the impact of technologies has inherent variations that can be handled by aleatoric ways.

Additional concerns related to the uncertainty should be focused on the level of technology maturity. There is a high possibility that the enlisted technologies which are selected to meet the design requirements are still in an immature status for integration. The maturity level of technologies is usually measured quantitatively by technology readiness level (TRL) [94,95]. The original definitions of TRL are based on the component level, not the system level. Thus, it is limited to applying the concept of TRL to system response analysis. In order to overcome this limitation,

other indices for considering integration in the perspective of systems were presented [15,16,96–98]. The new readiness level indices could resolve the limitation of the original TRLs, but they make the engineering problem more complex requiring more data collection and scrutinization. To minimize the complexity, the modified definition of TRL presented in Science Applications International Corporation (SAIC) report [99] is used in this study following Ref. [10], instead of incorporating other readiness level indices. The modified definitions of TRL are tabulated in Table 3.1. They are less focused on the component level.

Table 3.1. SAIC Modified TRL description [10]

Description	Level	Qualifier or Development Hurdle
Basic Research	1	Basic scientific/engineering principles observed and reported
Feasibility Research	2	Technology concept, application, and potential benefits formulated (candidate system selected)
Feasibility Research	3	Analytic and/or experimental proof-of-concept completed (proof of critical function or characteristic)
Technology Development	4	System concept observed in laboratory environment (breadboard test)
Technology Development	5	System concept tested and potential benefits substantiated in a controlled relevant environment
System Development	6	Prototype of system concept is demonstrated in a relevant environment
System Development	7	System prototype is tested and potential benefits substantiated more broadly in a relevant environment
Operational Verification	8	Actual system constructed and demonstrated, and benefits substantiated in a relevant environment
Operational Verification	9	Operational use of actual system tested, and benefits proven

Under the TRL assumption, the uncertainty of technology impact on a system is estimated. The immature technology with low TRL is hard to predict its impact on the system owing to a lack of data and knowledge on the technology, which implies the level of epistemic uncertainty is high a lot. As the technology development is progressing, the problem of "lack of knowledge" is resolved by accumulated data and information, which means epistemic uncertainty is reduced. Under this rationale, the expected technology impact distribution when a technology is fully developed reaching TRL of 9 is dependent on the current TRL of technologies. This analogy was presented by Ref. [10] in which the expected impact distributions of technologies were displayed depending on TRL as shown in Fig. 3.3 [10]. The detailed analogy can be found in Ref. [10]

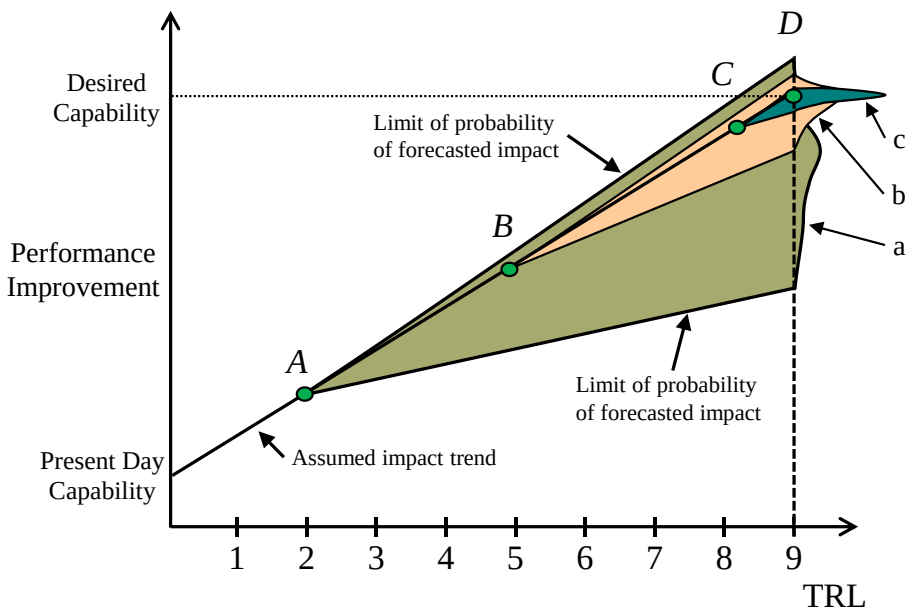

Fig. 3.3. Uncertainty forecast (reproduced from Ref. [10])

In order to handle both aleatory and epistemic uncertainty in the impact of technologies and mathematically reproduce a distribution of it, PDF determined by TRL is adopted for its distribution in this study [10]. Following Ref. [10], Weibull distribution is chosen of which shape parameter, β, and scale parameter, α, are modeled as a function of TRL (Eq. (3.1) [10]). $a_{i,j}$ is the impact factor of defined in Eq. (2.2).

$$\alpha|_{T_i, a_{i,j}, \beta=2} = |30\% a_{i,j}| - (TRL_{T_i} - 1) \cdot \frac{(|30\% a_{i,j}| - |5\% a_{i,j}|)}{8} \qquad (3.1)$$

The PDF curves for Weibull distribution of the two impact factors with different TRL are shown in Fig. 3.4 and Fig. 3.5, respectively. The theoretical limit is marked with a solid blue line. The nominal value (average) of the expected impact of the technology in immature status (low TRL) is far from the theoretical limit value. The variation of the distribution is much broader. On the other way, the nominal value of the expected impact of the technology in mature status (high TRL) is near to the theoretical value, and the distribution shows a narrower variation. The diminishment of variance by increasing TRL is linked to the reduction of epistemic uncertainty by resolving the lack of knowledge. It is noted that, even at TRL of 9, the magnitude of the impact factor cannot reach the theoretical limit and has a variability. This is due to the fact that aleatory uncertainty is irreducible and the theoretical limit is the ideal value. Other distribution functions such as triangular distribution and gamma distribution can also be applied depending on the circumstance of data collection, data characteristics, and decision makers' priority [15,16].

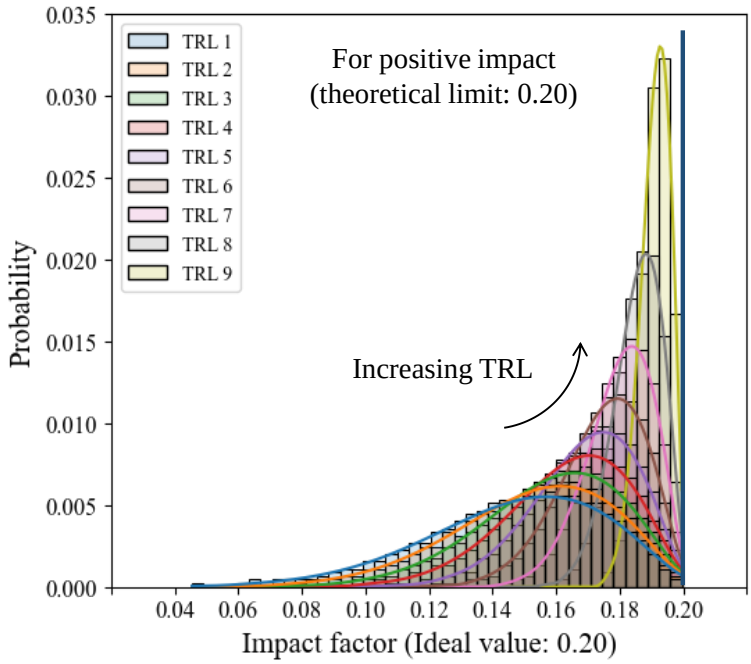

Fig. 3.4. Variability of impact factor depending on TRL (Positive impact)

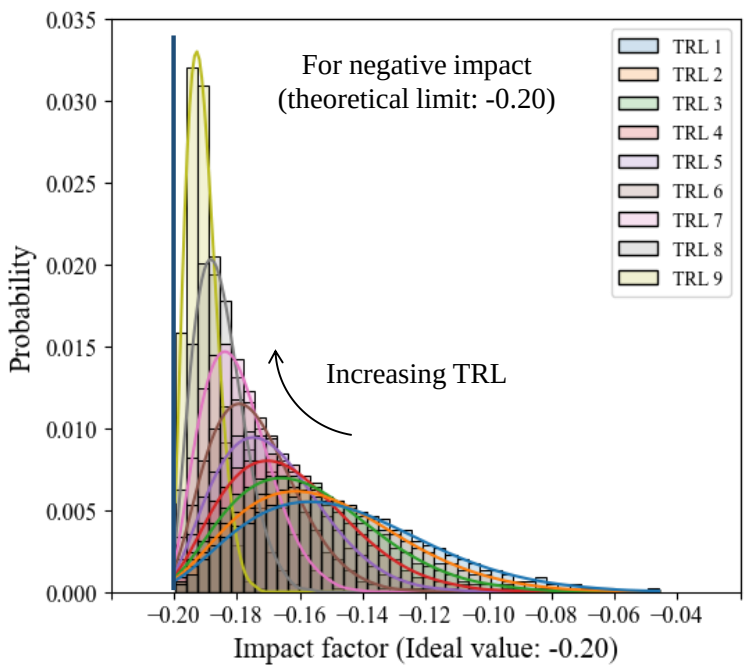

Fig. 3.5. Variability of impact factor depending on TRL (Negative impact)

In addition to uncertainties in the impact of technologies, the elements of TCIM and interaction factors that are obtained by Eq. (2.4) have also both aleatory and epistemic uncertainty for their figures because the elements of TCIM are determined by the similar to the approach for TIM case. They can be modeled using PDFs in the same way. However, this uncertainty was neglected in this study since the variability induced by interaction factors could be mixed and diluted by the variability in the expected impact of the technologies. The limit values of both ends resultant distribution for the variability of the element of TPEM could be different if extreme values from TCIM and TIM are sampled. Nevertheless, the possibility of the situation happening is highly low, resulting in little difference in the resultant elements of TPEM. Meanwhile, the advantage of reducing the computational burden and dimensional curse is significant by ignoring the variability of interaction factors.

Another uncertainty source is TRL of technology by itself. Since TRL is defined qualitatively as in Table 3.1 (also in the original definition), determining the exact number for specific technology is always controversial and subjective. In this dissertation, it is assumed that TRLs of technologies are determined as one value for each technology by averaging information from literature surveys and expertise from experts.

3.2.2. Uncertainty in surrogate model

Another major uncertainty in the process stems from the mathematical surrogate models that replace physics-based design tools. As mentioned earlier in Section 2.1.5, the use of surrogate models such as RSM, Gaussian process, and neural networks is usually an inevitable choice to relieve extremely high computational cost and time issues. This is because of the fact that, even in the deterministic process for technology portfolio assessment, the shortlist of the technology portfolios is extended following 2 to the power of the number of listed technologies (2^N). In building the surrogate models, the input space is usually explored through DOE process with efficient sampling methods such as Latin Hypercube Sampling (LHS) [100], D-optimal [101], and Sobol's sequence [102]. Unlike to the full-factorial method, these sampling methods are not fully cover the input space dimension, so that the surrogate model built with the sampled points should have uncertainty from missing space. The uncertainty is not vanished completely even if the full-factorial sampling is used.

In uncertainty quantification problems, therefore, incorporating the uncertainty from the surrogate models into the results is necessary to provide accurate information leading to appropriate decisions and risk management, but it was neglected in the previous studies [10,15,16] where the surrogate models were only used deterministically after their validation showed errors. The uncertainty from the surrogate models can be classified as an epistemic uncertainty. The schematic figure of the surrogate model and its epistemic uncertainty is shown in Fig. 3.6.

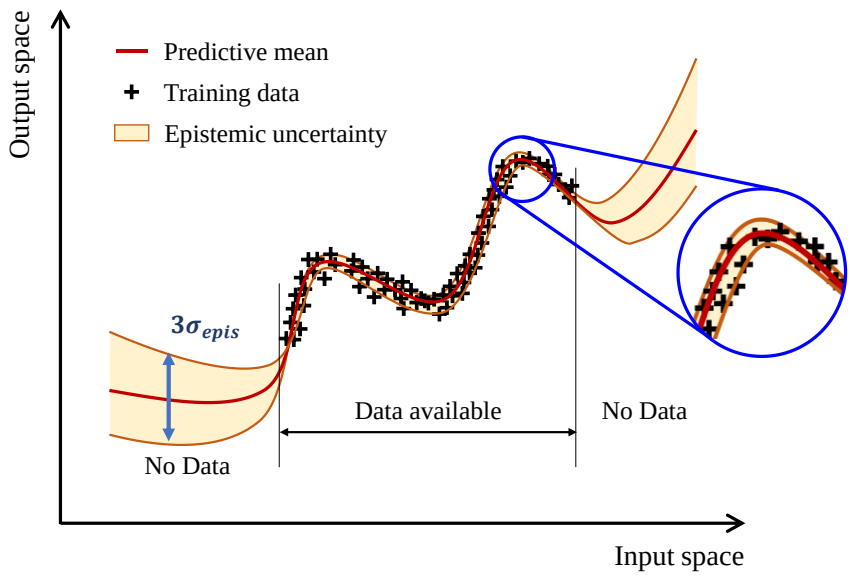

Fig. 3.6. Schematic of surrogate model and its uncertainty

The specific methods for quantifying this epistemic uncertainty depend on the type of surrogate model chosen to be used for individual projects. For example, in the case of the methods that provide variance information by themselves such as Kriging method [43] and Bayesian neural network [103], the variance information can be directly used to estimate the confidence interval that is interpreted as the epistemic uncertainty from the surrogate models. On the other hand, the deterministic surrogate methods such as the conventional RSM [41,42] and MLP neural network [44] do not provide variance information by themselves, so that additional techniques are needed for estimating variance from the model. One of the available techniques for the RSM is to use a prediction interval with probabilistic algorithms for estimating confidence intervals [104,105]. This technique can be applied to any other surrogate models since a prediction interval is always a

calculable feature. In the case of the conventional MLP model, the MC dropout technique [106] could aid to estimate uncertainty by mimicking the Bayesian neural network.

After obtaining variance information according to the chosen surrogate model and interval estimating technique, the total variance of a system response, σ_t^2, is calculated by Eq. (3.2) in which σ_t^2 is equal to the sum of variances by aleatory uncertainty, σ_a^2, and by epistemic uncertainty, σ_e^2, with an assumption that the two aleatory and epistemic uncertainty sources are independent of each other.

$$\sigma_t^2 = \sigma_a^2 + \sigma_e^2 \tag{3.2}$$

3.3. Uncertainties in Conceptual Design Framework

The uncertainties existing in the conceptual design framework were identified and treated by following the classification of the uncertainties described in Section 3.1.

3.3.1. Uncertainty in physical parameter variant

There are a lot of physical parameters used as input variables for the sizing program such as rotor radius, wing span, battery specifications, wind condition, altitude profile, and flight speed. These parameters have inherent randomness in natural environment, which can be handled by the aleatoric way using PDF or CDF curves as described in Section 3.1.1. Although the shape of PDF curve is dependent on collected data or circumstance, Gaussian distribution or normal distribution is the most common type of distribution used to model variation in the physical parameters. A coefficient of variation (COV), a ratio of standard deviation σ and mean μ, defined as Eq. (3.3) is usually used for presenting how much data are scattered with respect to the mean value. With assumptions for the type of distribution and COV for each physical parameter, the variation in the physical parameter can be modeled. The exact parameter considered in uncertainty quantification was presented in Section 4.2. The terminology of parametric uncertainty was interchangeable with aleatory uncertainty or input uncertainty in this dissertation.

$$COV = \frac{\sigma}{\mu} \times 100\ [\%] \tag{3.3}$$

3.3.2. Uncertainty in simplified analysis models

Uncertainties induced by simplified analysis models in RISPECT+ are classified as epistemic uncertainty. In this study, this type of uncertainty is referred to as model uncertainty considering the origination of the uncertainty.

Uncertainties in the two analysis modules in RISPECT+, rotor aerodynamics and wing aerodynamics analysis, were considered because these two modules mainly determine the performance of advanced air mobility. Since the electric propulsion system analyses are based on constant efficiency herein those models were excluded. Through comparing analysis results with experimental data or higher fidelity analysis results, the modules not only were validated, but also parameters that quantify the model uncertainty are obtained for each analysis module. The model uncertainty parameter θ is defined by Eq. (3.4), where y_{pred} is the output quantity of interest calculated by RISPECT+ and y_{true} is the reference value that can be obtained from experiments or datasheets from manufacturers, or higher fidelity solvers.

$$\theta_i = \frac{y_{true}}{y_{pred}} \quad i\ for\ analysis\ model \tag{3.4}$$

It is assumed that the obtained y_{true} is genuinely true value. Uncertainties that might arise in the data-obtaining process such as measurement or post-processing are neglected herein since those kinds of uncertainties are not. In Fig. 3.7, the method for the calculation of the model uncertainty parameter is shown schematically.

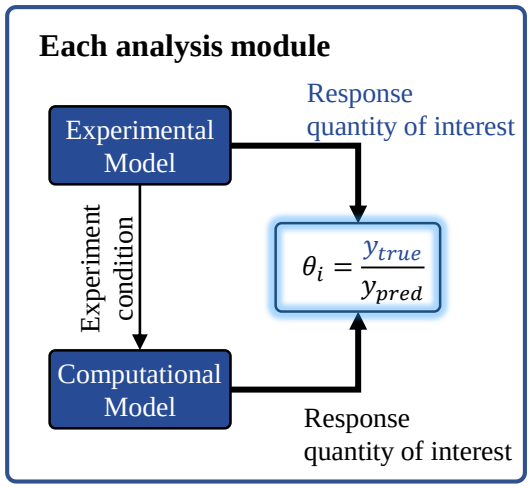

Fig. 3.7. Model uncertainty parameter calculation [91]

Uncertainty in the rotor aerodynamic module was considered in terms of the power of a rotor P_{rotor} which was calculated by the BEMT and BET method [49,50]. The model uncertainty parameter $\theta_{pw,BEMT}$ for the BEMT method and $\theta_{pw,BET}$ for the BET method are defined as Eq. (3.5), respectively. The equations are defined as the power coefficient over rotor solidity in order to directly use data from Fig. 2.10 and Fig. 2.11.

$$\theta_{pw,BEMT} = \left.\frac{C_p/\sigma_{R_{true}}}{C_p/\sigma_{R_{pred}}}\right|_{BEMT}, \quad \theta_{pw,BET} = \left.\frac{C_p/\sigma_{R_{true}}}{C_p/\sigma_{R_{pred}}}\right|_{BET} \tag{3.5}$$

The calculated model uncertainty parameters for each rotor aerodynamics analysis method are presented in Fig. 3.8 and Fig. 3.9, respectively.

Seeing Fig. 3.8 for BEMT method in hover mode, $\theta_{pw,BEMT}$ are scattered almost randomly. After blade loading C_T/σ_R of approximately 0.11, it might be determined that there is a trend between C_T/σ_R and $\theta_{pw,BEMT}$. However, the number of points

used for comparison is not sufficient to induce a certain trend, and the missing area could be generated where the trend would not match well. Hence, an interval covering all data is presented instead of adopting a trend hastily. The $\theta_{pw,BEMT}$ has the expectation of 1.0122, which means the BEMT method in RISPECT+ underestimates the rotor power in hover mode. The interval is from 0.9638 to 1.0582, a range of within 6% difference.

As can be seen in Fig. 3.9, the model uncertainty parameters for the BET method $\theta_{pw,BET}$ are scattered more randomly in this time, so that the same approach using interval was applied for the BET method in tilt mode flight. The $\theta_{pw,BET}$ has the expectation of 0.9541, which means the BET method in RISPECT+ overestimates the rotor power in tilt mode. The interval is from 0.8246 to 1.0441, a range of within 6% difference.

Table 3.2 presents the expectation and interval of the two model uncertainty parameters. It is assumed that the two parameters $\theta_{pw,BEMT}$, and $\theta_{pw,BET}$ are identically applied to other flight conditions where different rotational speeds or advance ratios were encountered during the sizing process.

Table 3.2. Expectation and interval of $\theta_{pw,BEMT}$, and $\theta_{pw,BET}$

Parameter	Expectation	Interval
$\theta_{pw,BEMT}$	1.0122	[0.9638, 1.0582]
$\theta_{pw,BET}$	0.9541	[0.8246, 1.0441]

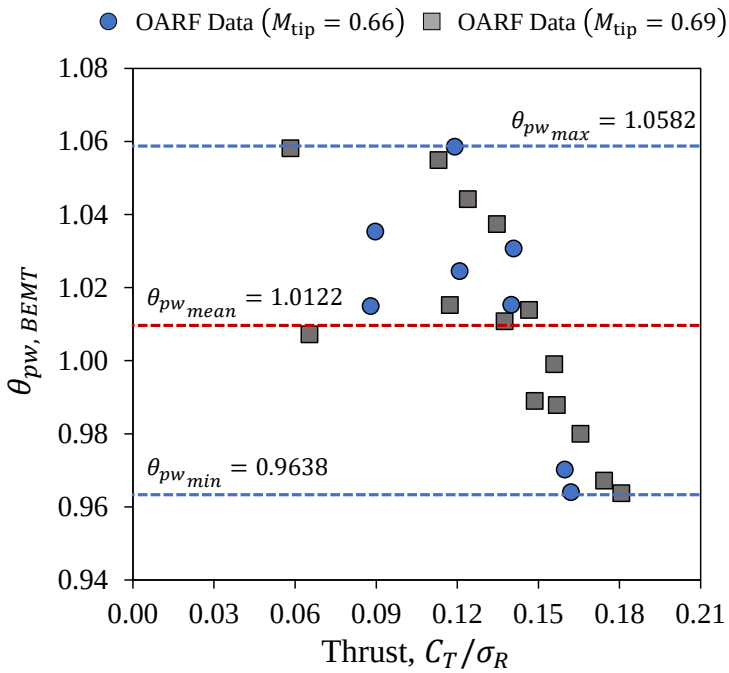

Fig. 3.8. Model uncertainty parameter in BEMT method (hover mode)

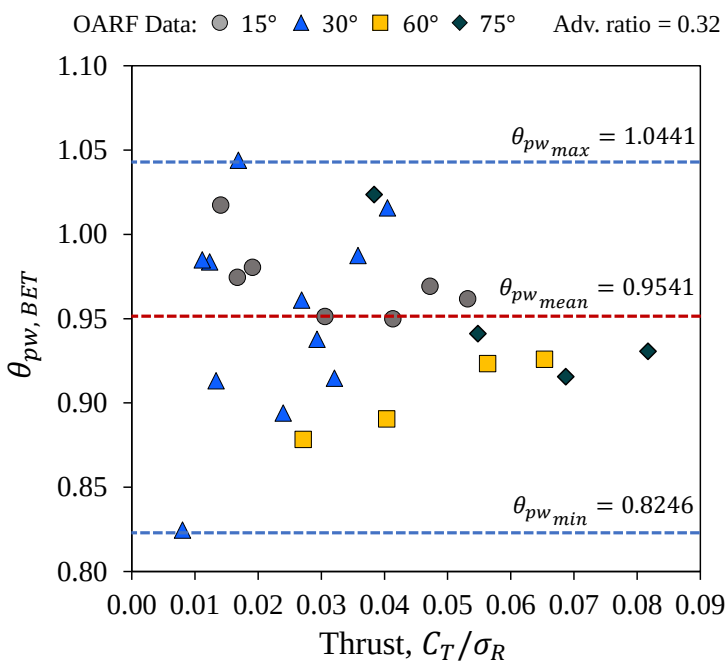

Fig. 3.9. Model uncertainty parameter in BET method (tilt mode)

The same analysis was conducted for the wing aerodynamic analysis. In RISPECT+, the 3D lift coefficient curve slope C_{L_α} was obtained by Eq. (2.18). The model uncertainty parameter for the lift coefficient curve slope $\theta_{C_{L_{\alpha_{wing}}}}$ is defined by Eq. (3.6).

$$\theta_{C_{L_{\alpha_{wing}}}} = \frac{C_{L_{\alpha_{true}}}}{C_{L_{\alpha_{pred}}}} \tag{3.6}$$

In Ref. [55], C_{L_α} per radian calculated by Eq. (2.18) and vortex lattice method (VLM) were presented for various wing planform designs. The data and $\theta_{C_{L_{\alpha_{wing}}}}$ is tabulated in Table 3.4. In this time, $C_{L_{\alpha_{true}}}$ was settled by VLM data.

Table 3.3 presents the expectation and interval of the $\theta_{C_{L_{\alpha_{wing}}}}$. Although the expectation is nearly equal to one, there is an uneven deviation in the interval. The maximum $\theta_{C_{L_{\alpha_{wing}}}}$ is 1.0273, which implies the empirical equation underestimated the lift coefficient curve slope by approximately 3%, and the minimum $\theta_{C_{L_{\alpha_{wing}}}}$ is 0.9623, which implies that the empirical equation could overestimate the lift coefficient curve slope by approximately 4%.

Table 3.3. Expectation and interval of $\theta_{C_{L_{\alpha_{wing}}}}$

Parameter	Expectation	Interval
$\theta_{C_{L_{\alpha_{wing}}}}$	1.0061	[0.9623, 1.0273]

Table 3.4. $\theta_{C_{L_{\alpha_{wing}}}}$ for different wing configurations (data from Ref. [55])

Wing planform	Calculated C_{L_α}		$\theta_{C_{L_{\alpha_{wing}}}}$
	Eq. (2.18)	VLM	
Elliptical, straight half chord	4.90	5.02	1.0245
Elliptical, straight LE*	4.87	4.99	1.0246
Elliptical, straight TE*	4.87	4.99	1.0246
Schuemann	4.88	4.99	1.0225
Semi-straight taper	4.90	4.98	1.0163
Straight taper, straight half chord	4.90	4.96	1.0122
Straight taper, straight LE	4.89	4.95	1.0123
Straight taper, straight TE	4.89	4.95	1.0123
Compound taper	4.90	4.88	0.9959
Rectangular	4.90	4.82	0.9837
Crescent	4.59	4.60	1.0022
Swept back, TR*=0.5, LE sweep 30°	4.40	4.52	1.0273
Swept forward, TR=0.5, LE sweep 30°	4.24	4.32	1.0189
Swept back, TR=1.0, LE sweep 30°	4.35	4.29	0.9862
Delta	2.51	2.44	0.9721
Double delta	2.39	2.30	0.9623
Disk	1.83	1.84	1.0055

* LE: leading edge, TE: trailing edge, TR: taper ratio

The obtained intervals of the model uncertainty parameters for rotor aerodynamics and wing aerodynamics analysis were used in the uncertainty quantification of the flight performance of advanced air mobility in Section 4.2.

3.4. Uncertainty Propagation: Monte Carlo Simulation

One of the various popular methods for the forward propagation of uncertainties to the system responses is Monte Carlo Simulation (MCS). MCS is based on a number of repetitive deterministic calculations with sampled input parameters following the law of large numbers. MCS has been widely implemented for various uncertainty quantification studies [10,15–18,27,39,40,91,107,108] due to the solver-independent characteristics of MCS which encloses the solvers or governing equations outside and does not require additional modifications of them. Although MCS requires excessive computation time, MCS is used in this study, and other probabilistic methods for uncertainty quantification such as polynomial chaos expansion [109], stochastic collocation, and Gaussian quadrature [33] were ruled out mainly owing to the following reasons. The first reason is the relatively large number of random variables in the technology portfolio assessment process (the number of elements in TIM) and a large number of alternative design candidates (the number of rows in TPM). Stochastic expansion methods based on full tensor product quadrature are not effective in this situation [16]. The second reason for applying MCS is to evade additional uncertainties produced when functions of interest (system responses) are approximated by approximation-based methods. Additionally, the fact that a single analysis of RISPECT+ can be executed within several seconds alleviating the time issue is the supplementary reason.

In the technology portfolio assessment process, MCS loop wraps the surrogate model that is constructed for system responses by technology impact. It is a kind of

in-direct MCS environment. On the other hands, in the uncertainty quantification of RISPECT+, MCS loop wraps the conceptual sizing framework, constructing a direct MCS environment.

Although both MCS environments were set with the appropriate assumptions and circumstances, the original MCS coupled with a purely random sampling method typically requires too many sample points, nearly 100,000 size for them, for securing the convergence of response [39,108,110]. To reduce the MCS problem to the more manageable quantification problem, LHS method instead of the random sampling is coupled for MCS, which shows much faster converged results with almost 10 times smaller sample size [27,91,108]. The LHS from multiple PDFs in the uncertainty quantification problem is well described schematically in Fig. 3.10 [27].

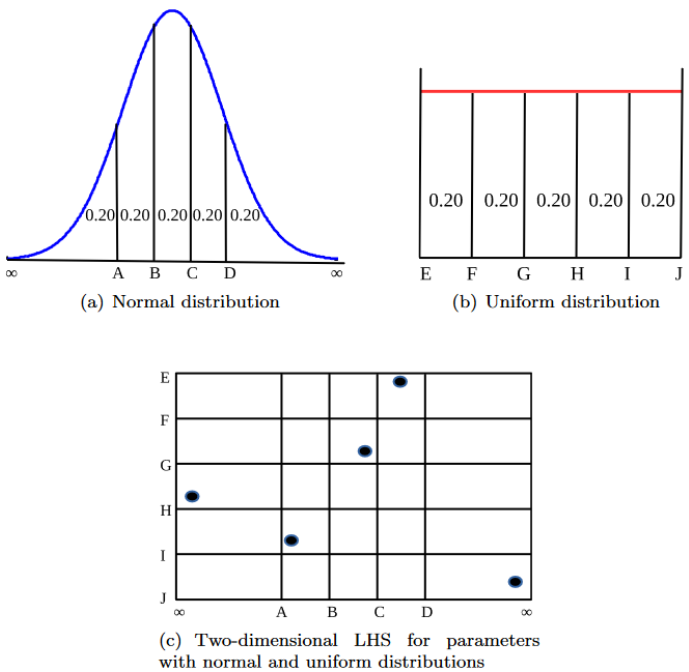

Fig. 3.10. Representation of LHS probable intervals for parameter input space sampling [27]

The schematic diagram of entire MCS process is shown in Fig. 3.11 where uncertain inputs and outputs are shown with PDF curves.

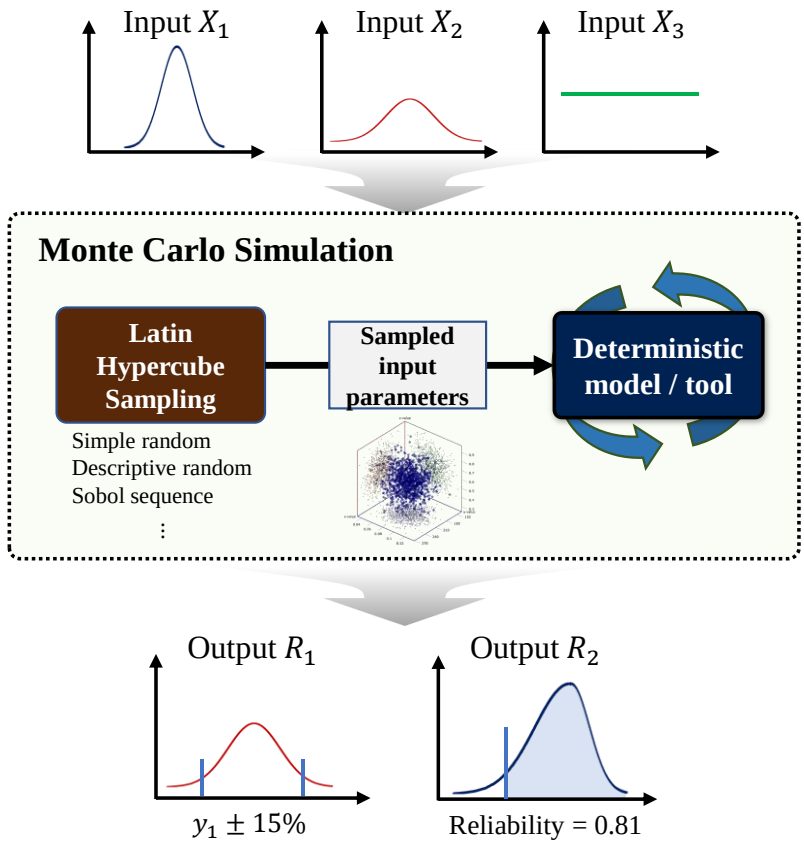

Fig. 3.11. Schematic diagram of MCS

Probabilistic outcomes are obtained as results of MCS. The statistical moments such as expectation (mean), standard deviation, and skewness coefficient can be obtained by Eqs. (3.7), (3.8), and (3.9), respectively. In the equations, N_s is the number of samples, R_i is a system response of interest, μ is an expectation, σ is a standard deviation, $\tilde{\mu}_3$ is a skewness coefficient, and $\mathrm{E}[\cdot]$ is the operator for expectation.

$$\mu_{R_i} = E[R_i] = \frac{1}{N_s}\sum_{k=1}^{N_s} R_{i,k} \tag{3.7}$$

$$\sigma_{R_i} = \sqrt{\frac{1}{N_s}\sum_{k=1}^{N_s}\left(R_{i,k} - \mu_i\right)^2} \tag{3.8}$$

$$\tilde{\mu}_{3_{R_i}} = E\left[\left(\frac{R_i - \mu_i}{\sigma_i}\right)^3\right] \tag{3.9}$$

Using a prescribed value, the reliability can be calculated. The PDF curve of output quantities obtained after MCS can be drawn by kernel density estimator with Gaussian basis function [111] (Eq. (3.10)). The detailed process for MSC process will be presented in the examples of method implementation in the following Chapter 4.

$$\hat{f}_h(x) = \frac{1}{nh}\sum_{i=1}^{n} K\left(\frac{x - x_i}{h}\right) \; where\ K\ is\ kernel\ with\ Gaussian\ basis \tag{3.10}$$

Chapter 4

Method Implementation

The methodologies presented through Chapter 2 and Chapter 3 are implemented to pilot programs for a hypothetical advanced air mobility eVTOL for transportation in urban areas as an exemplary demonstration. The eVTOL aircraft is considered a suitable testbed for the method implementation because various eVTOL aircraft designs have been proposed and developed for future air mobility with a lot of attention received. Section 4.1 demonstrates the process of technology portfolio assessment, and Section 4.2 describes uncertainty quantification in the conceptual sizing of the hypothetical advanced air mobility eVTOL.

4.1. Uncertainty-based Technology Portfolio Assessment for eVTOL

The uncertainty-based technology portfolio assessment for eVTOL was conducted following the steps described in Section 2.1. For a test bed of the process, one of the representative configurations of eVTOL aircraft was used, which was optimally sized before with RISPECT+. In the sizing process after applying the impact of technologies, the optimizer step in Fig. 2.8 was excluded. The elements of TPEV, $\vec{e}$, was fed into RISPECT+ with input data, and correspond parameters were modified by following Eq. (2.6) during the sizing process.

4.1.1. Test Bed eVTOL

The baseline of a hypothetical eVTOL aircraft configuration is displayed in Fig. 4.1 which is similar to Joby S4 configuration, one of the prevalent vectored thrust type eVTOL designs. It has six tilting rotors and T-shaped empennage system. The baseline was sized by RISPECT+ for a typical mission profile where maximum flight range is 100 km with a payload of 500 kg (1102.31 lb), which is shown in Fig. 4.2. The mission profile comprises of vertical take-off, climb, cruise, descent, and vertical landing segments with ground taxiing of 50 m. The numbers for each segment are presented in the figure.

The sizing assumptions such as efficiency coefficients and specific power of electric propulsion components were tabulated in Table 4.1 and the summary for specification of the optimally sized baseline eVTOL aircraft and constraint are presented in Table 4.2. The gross weight was approximately 2409 kg (5311 lb) for carrying the payload of 500 kg (1102.31 lb). The mounted battery energy capacity was estimated as 122 kWh with assumption that specific energy of the battery was given as 205 Wh/kg. The maximum noise level presented by overall sound pressure level (OASPL) with A-weighting was 67.5 dBA, and the effective lift-to-drag ratio was obtained as to be approximately 9.05. The economics quantities of the baseline included vehicle cost, DOC, and RDT&E cost that were analyzed by the equations from Section 2.2.6. Given the assumed constraint values, there were multiple violations in the gross weight, noise level, and direct operating cost.

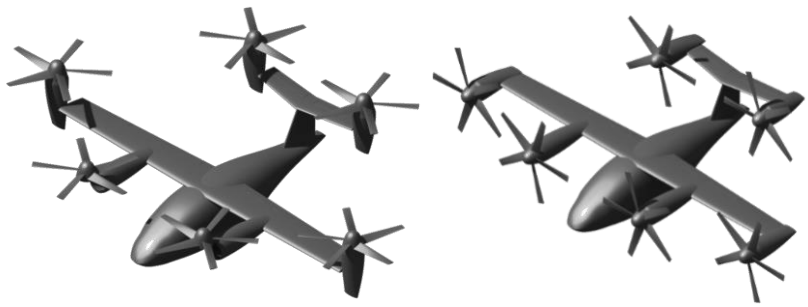

Fig. 4.1. Baseline eVTOL concept (left: VTOL mode, right: cruise mode)

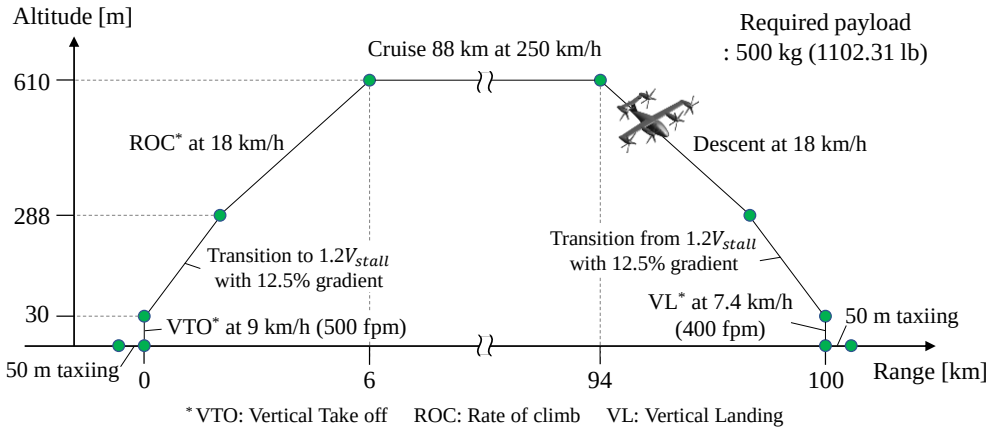

Fig. 4.2. Mission profile schematic used for the baseline eVTOL sizing

Table 4.1. Sizing assumptions

Component	Parameter	Value
Battery	Specific energy	205 Wh/kg
	Maximum DoD	0.80
	Maximum discharge C-rate	10C
	Efficiency	0.93
Electric motor	Specific power	4.1 kW/kg
	Efficiency	0.96
Inverter	Specific power	13 kW/kg
	Efficiency	0.98
TMS	Specific power	0.68 kW/kg

Table 4.2. Baseline eVTOL design summary

Parameter	Value	Constraint / Target
Gross weight	5310.914 lb (2409.01 kg)	$\leq$ 5000 lb
Payload	1103.42 lb (500.50 kg)	·
Battery energy	122.617 kWh	Minimize
Max. OASPL @ hover	67.521 dBA	$\leq$ 65 dBA
Effective lift to drag ratio	9.054	$\geq$ 9.0
Vehicle cost	1.87M USD	Minimize
Direct operating cost	796.01 USD/FH	$\leq$ 750 USD/FH
RDT&E cost	162.55M USD	Minimize

4.1.2. Technology Identification

As shown in Table 4.2, there were multiple violations of constraints in the performance and economics specification. These violations were kinds of show-stoppers in the development program. For example, the operation permit could be restricted based on the maximum noise level by the regulatory administration such as Federal Aviation Administration (FAA) and European Union Aviation Safety Agency (EASA) of which proposal of noise regulation had been discussed to be presented under 65 dBA. Gross weight of which the constraint was set as 5,000 lb also should be reduced over 8% more to satisfy the constraint. Direct operating cost was one of the most important parameters that should be paid attention for the sustainability of the business. Consequently, technologies that have an effect on noise performance, gross weight, and operating cost should be considered and identified.

In this project, seventeen technologies from various disciplines such as aerodynamics, electric propulsion, and manufacturing were identified and their TRL figures were obtained from literature reviews and expertise [112–114]. The identified technologies are listed in Table 4.3 where the TRLs are averaged values. The technologies were directly or indirectly related with the performance and economics specification of the test bed eVTOL. For instance, lithium-sulfur battery cells and fuel cell propulsion technology were connected to gross weight since they determined the energy density of the energy reservoir. Rotor planform and active control technologies had an effect on aerodynamic and aero-acoustic performance.

De/anti-icing technologies could extend operational days per year securing all weather capability for the eVTOL, which eventually led to the reduction in direct operating cost.

Table 4.3. Identified technology list

	Technology	TRL
$\mathbf{T_1}$	Lithium-sulfur battery cell	5
$\mathbf{T_2}$	Fuel cell propulsion	5
$\mathbf{T_3}$	Carbon composite wing structure	7
$\mathbf{T_4}$	Carbon composite fuselage structure	7
$\mathbf{T_5}$	Carbon composite rotor structure	6
$\mathbf{T_6}$	Truss-braced wing	4
$\mathbf{T_7}$	Battery package integration	5
$\mathbf{T_8}$	Laminar flow control	5
$\mathbf{T_9}$	Electric ducted fan	8
$\mathbf{T_{10}}$	High power electric motor	6
$\mathbf{T_{11}}$	Rotor airfoil/planform for aero performance	5
$\mathbf{T_{12}}$	Rotor phase control for low noise and vibration	6
$\mathbf{T_{13}}$	Rotor airfoil/planform for low noise	5
$\mathbf{T_{14}}$	Rotor active twist control for low noise and vibration	5
$\mathbf{T_{15}}$	Heat coil/mat for de/anti-icing	6
$\mathbf{T_{16}}$	Surface coating for anti-icing	7
$\mathbf{T_{17}}$	Fast production technology	5

4.1.3. Technology Impact

The next step was to construct TIM. Among eVTOL aircraft system attributes, 23 parameters that were highly related to subsystems such as powertrain, rotor-blade system, structural system, operating system, and manufacturing technique were selected. They included subsystem weights, aggregated efficiency of the propulsion system, RDT&E cost, and unit cost of parts. The elements of TIM are mainly determined by literature surveys and Delphi approach.

In the process, the increment of RDT&E cost was corrected depending on the nature of the technologies and their TRLs. If a technology is related to components of the aircraft itself that are usually developed by an aviation company, the figure of the impact on RDT&E cost (s_{10}) is relatively high. On the other hand, "off-the-shelf" technology from ally companies, such as battery and electric motor, has a lower magnitude in RDT&E cost only for the integration aspect. Instead, these kinds of technologies induce the increment in unit cost of the related parts. The technologies with low TRL also are assumed to tend to have a relatively high impact on RDT&E cost. This is because that the distributions of impact factor are determined on the basis of the assumption that the all technologies reach TRL of 8 or 9 successfully when the target system is ready to production in the future. In this assumption, it can be inferred that relatively more RDT&E fund is need to catch up belated technology readiness. With this analogy, RDT&E correction is applied when constructing TIM in spite of a little subjectivity.

The constructed TIM at the deterministic assessment with theoretical limits is shown in Fig. 4.3. Based on these figures in the deterministic TIM, when probabilistic approach is applied, the distributions of the elements of TIM is modeled as shown in Fig. 3.4 and Fig. 3.5.

The TRLs of each technology are presented in the first row. The last two right columns are the limit ends of the element of TIM without consideration of the compatibility of the technologies. These limit ends guide the range of the input space for a surrogate model.

		T_1	T_2	T_3	T_4	T_5	T_6	T_7	T_8	T_9	T_{10}	T_{11}	T_{12}	T_{13}	T_{14}	T_{15}	T_{16}	T_{17}	Min	Max
System attributes	**TRL**	**5**	**5**	**7**	**7**	**6**	**4**	**5**	**5**	**8**	**6**	**5**	**6**	**5**	**5**	**6**	**7**	**5**		
Efficiency of rotor	s_1									0.07		0.05	-0.02	-0.04	-0.02				-0.078	0.124
Efficiency of powertrain (Motor, inverter, battery)	s_2	0.05									-0.05								-0.050	0.050
Energy source (Battery, fuel cell) Specific energy	s_3	0.30	0.20					0.05											0.000	0.638
Total wing lift coefficient	s_4						0.05		0.05	0.03							-0.02		-0.020	0.136
Total parasite drag coefficient	s_5						0.03	-0.02	-0.10	0.05						0.02	0.01		-0.118	0.114
Main wing system weight	s_6			-0.15			0.06		0.03	0.02						0.02			-0.150	0.136
Fuselage weight	s_7				-0.20		0.10								-0.05				-0.240	0.100
Rotor system weight (incl. hub, duct)	s_8					-0.05				0.10		0.02	0.05	0.05	0.10	0.01			-0.050	0.374
Electric motor weight	s_9										-0.03								-0.030	0.000
RDT&E fund	s_{10}	0.08	0.10	0.15	0.15	0.15	0.20	0.05	0.20	0.03	0.08	0.15	0.08	0.15	0.15	0.10	0.05	0.20	0.000	5.918
Energy source unit cost	s_{11}	0.50	0.30					0.05											0.000	1.048
Elelctric motor unit cost	s_{12}										0.30								0.000	0.300
Rotor system unit cost	s_{13}					0.05				0.10		0.05	0.10	0.12	0.15	0.05			0.000	0.804
Airframe unit cost	s_{14}			0.08	0.08		0.10		0.05							0.05		-0.05	-0.050	0.415
Battery life cycle	s_{15}	-0.15	-0.05					0.05											-0.193	0.050
Noise level (pressure)	s_{16}									-0.15		0.05	-0.08	-0.05	-0.12				-0.346	0.050
Aircraft production rate	s_{17}			-0.05	-0.05				-0.15			-0.15	-0.05	-0.10	-0.15			0.50	-0.526	0.500
Operating days per year	s_{18}						-0.05				-0.05					0.20	0.10		-0.098	0.320
Number of flight per day	s_{19}	0.05	0.20							0.10			0.15	0.10	0.15	0.10	0.05		0.000	1.329
Total operating year	s_{20}			0.05	0.05			-0.05					0.05	0.02	0.10			-0.10	-0.145	0.299
Avionics system unit cost	s_{21}		0.05						0.05				0.05		0.08	0.10			0.000	0.375
Maintenance unit cost	s_{22}	0.05	0.10	0.08	0.08	0.10	0.08	-0.05	0.15	0.10	0.01	0.05	0.08	0.05	0.20	0.10	0.12		-0.050	2.600
Idle power consumption	s_{23}								0.02				0.05		0.08	0.20			0.000	0.388

Fig. 4.3. Technology impact matrix with theoretical limit

4.1.4. Generation of Technology Portfolio Candidates

The relationships between the identified technologies constructed TCIM element shown in Fig. 4.4 following the definition of the element of TCIM (Eq. (2.3)). Note that most of elements in the lower triangular area are symmetric to those in the upper triangular area, but some of them are asymmetric relationship. The numbers in Fig. 4.4 was obtained based on literature reviews, and expert opinions.

Some of the representative relationships are described below.

1. $T_1 \leftrightarrow T_2$: competing technologies for energy source.
2. $T_1 \leftrightarrow T_{11}$: lithium-sulfur battery has no influence on rotor aero-performance, but high aero-efficient rotor aero-performance technology requires power from energy source, degrading lithium-based battery technology.
3. $T_3 \leftrightarrow T_{17}$: carbon composite structure needs heat, pressure and vacuum to made, which makes hard to mass production.
4. $T_3 \leftrightarrow T_6$: truss-braced wing degrades the benefit of carbon composite structure for wing (low weight) since joint between brace and wing needs to be reinforced by metallic materials (element below of 1). On the other hand, effect of truss-braced wing rarely get impact from carbon composite structure for wing.
5. $T_{11} \leftrightarrow T_{13}$: rotor planform for aerodynamic performance and for noise performance could not be compatible.

	T_1	T_2	T_3	T_4	T_5	T_6	T_7	T_8	T_9	T_{10}	T_{11}	T_{12}	T_{13}	T_{14}	T_{15}	T_{16}	T_{17}
T_1	1.00	0.00	1.00	1.00	1.00	1.00	1.10	1.00	1.05	1.03	0.95	1.00	1.00	1.00	1.00	1.00	1.00
T_2	0.00	1.00	1.00	1.00	1.00	1.00	1.03	1.00	1.00	1.00	1.02	1.00	1.00	1.00	1.00	1.00	1.00
T_3	1.00	1.00	1.00	1.00	1.00	0.90	1.00	0.00	0.95	1.00	1.00	1.00	1.00	1.00	0.00	1.00	0.00
T_4	1.00	1.00	1.00	1.00	1.00	0.90	1.05	1.00	1.00	1.00	1.00	1.00	1.00	1.00	0.98	1.00	0.00
T_5	1.00	1.00	1.00	1.00	1.00	1.00	1.00	1.00	1.00	1.00	0.98	1.00	0.98	0.00	1.00	1.00	0.00
T_6	1.00	1.00	1.00	1.00	1.00	1.00	1.00	0.92	1.00	1.00	1.00	1.00	1.00	1.00	1.00	1.00	1.00
T_7	1.10	1.03	1.00	1.00	1.00	1.00	1.00	1.00	1.00	1.00	1.00	1.00	1.00	1.00	1.00	1.00	1.00
T_8	1.00	1.00	0.00	1.00	1.00	0.92	1.00	1.00	0.95	1.00	1.00	1.00	1.00	1.00	0.00	0.95	1.00
T_9	1.00	1.00	1.00	1.00	1.00	1.00	1.00	1.00	1.00	1.00	0.00	0.00	0.00	0.00	1.00	1.00	1.00
T_{10}	1.03	0.95	1.00	1.00	1.00	1.00	1.00	1.00	1.00	1.00	1.00	1.00	1.00	1.00	1.00	1.00	1.00
T_{11}	1.00	1.00	1.00	1.00	0.98	1.00	1.00	1.00	0.00	1.00	1.00	0.95	0.00	0.95	1.00	1.00	1.00
T_{12}	1.00	1.00	1.00	1.00	1.00	1.00	1.00	1.00	0.00	1.00	0.95	1.00	1.05	0.00	1.00	1.00	1.00
T_{13}	1.00	1.00	1.00	1.00	1.00	1.00	1.00	1.00	0.00	1.00	0.00	1.05	1.00	0.00	1.00	1.00	1.00
T_{14}	1.00	1.00	1.00	1.00	0.00	1.00	1.00	1.00	0.00	1.00	1.00	0.00	0.00	1.00	1.00	1.00	1.00
T_{15}	1.00	1.00	0.00	1.00	1.00	1.00	1.00	0.00	1.00	1.00	1.00	1.00	1.00	1.00	1.00	0.00	1.00
T_{16}	1.00	1.00	1.00	1.00	1.00	1.00	1.00	0.95	1.00	1.00	1.00	1.00	1.00	1.00	0.00	1.00	1.00
T_{17}	1.00	1.00	0.00	0.00	0.00	1.00	1.00	1.00	1.00	1.00	1.00	1.00	1.00	1.00	1.00	1.00	1.00

Fig. 4.4. Technology compatibility and interaction matrix (TCIM)

The resultant TPM considering the compatibility between technologies was obtained. The number of technology portfolios was reduced approximately by half from 131,072 to 6,456. In Fig. 4.5, 6,456 technology portfolios are listed including the baseline; all elements of TPV for the baseline are zero.

	T_1	T_2	T_3	T_4	T_5	T_6	T_7	T_8	T_9	T_{10}	T_{11}	T_{12}	T_{13}	T_{14}	T_{15}	T_{16}	T_{17}
Baseline	0	0	0	0	0	0	0	0	0	0	0	0	0	0	0	0	0
Alt_1	0	0	0	0	0	0	0	0	0	0	0	0	0	0	0	0	1
⋮	⋮	⋮	⋮	⋮	⋮	⋮	⋮	⋮	⋮	⋮	⋮	⋮	⋮	⋮	⋮	⋮	⋮
Alt_{2964}	1	0	0	0	0	1	0	0	1	1	0	0	0	0	1	0	0
⋮	⋮	⋮	⋮	⋮	⋮	⋮	⋮	⋮	⋮	⋮	⋮	⋮	⋮	⋮	⋮	⋮	⋮
Alt_{6455}	1	0	1	1	1	1	1	0	0	1	1	1	0	0	0	1	0

Fig. 4.5. Technology portfolio matrix (TPM)

4.1.5. Technology Portfolio Effect

Finally, the resultant TPEM was constructed by Eq. (2.5) in accordance with TPM, TIM, and interaction factor. In the deterministic analysis, a single TPEM of $[6{,}456] \times [23]$ shape. When the probabilistic approach was used, N_s sampled TIM from the distribution by Eq. (3.1) were selected, and then a single TPEM was extended to the 3-dimensional array. In this study, 10,000 samples were drawn by LHS making the resultant TPEM of $[10{,}000] \times [6{,}456] \times [23]$ shaped array that is shown in Fig. 4.6.

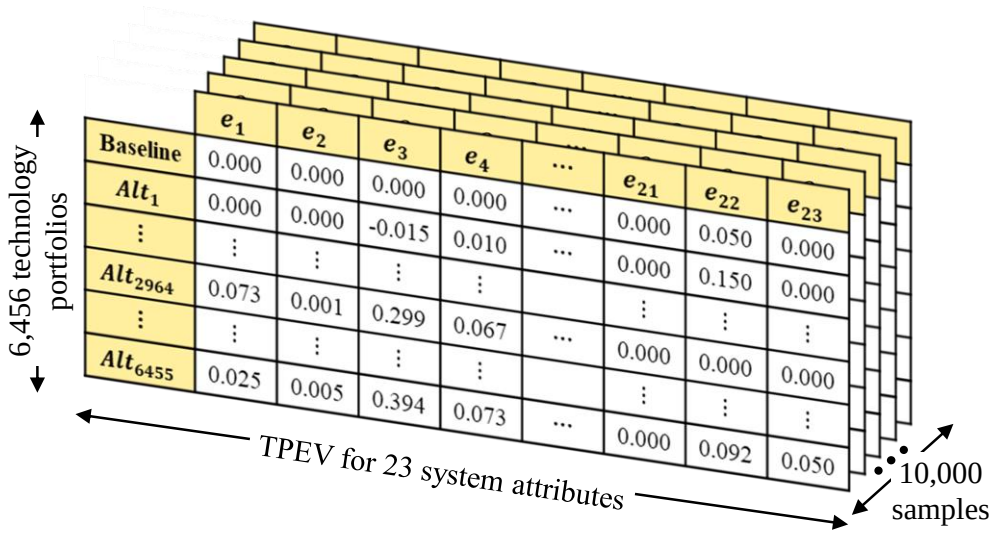

	e_1	e_2	e_3	e_4	⋯	e_{21}	e_{22}	e_{23}
Baseline	0.000	0.000	0.000	0.000	⋯	0.000	0.050	0.000
Alt_1	0.000	0.000	-0.015	0.010	⋯	0.000	0.150	0.000
⋮	⋮	⋮	⋮	⋮		⋮	⋮	⋮
Alt_{2964}	0.073	0.001	0.299	0.067	⋯	0.000	0.000	0.000
⋮	⋮	⋮	⋮	⋮		⋮	⋮	⋮
Alt_{6455}	0.025	0.005	0.394	0.073	⋯	0.000	0.092	0.050

Fig. 4.6. Technology portfolio effect matrix

4.1.6. Surrogate Model construction

As mentioned in Section 2.1.5, although the assessment of technology portfolios could be conducted using the design tool, herein RISPECT+, the direct calculation through the design tool requires burdensome computational resources and time. Even in the deterministic environment, the required number of evaluations is equal to 6,456 (the number of rows in TPEM). The number of evaluations has increased by 10,000 times, approximately 65 million, when the MCS environment was set. For a rapid MCS implementation with reduced computational resources, MLP model [44], one of artificial neural networks, was adopted to replace the design tool in this study. The MLP model was chosen since it is more suitable for the non-linear system with a large number of in-output parameters than other models like RSM and Kriging model. If the problem is reduced with less in-output parameters, Kriging model or other methods also can be used. The architecture of MLP model is shown in Fig. 4.7 where input parameters are the elements of TPEV (e_i), and output parameters are in total 12 performance and economics quantities including gross weight, maximum noise level, and vehicle cost. The 12 response quantities are tabulated in Table 4.4. The maximum noise level is presented as the overall sound pressure level in dBA.

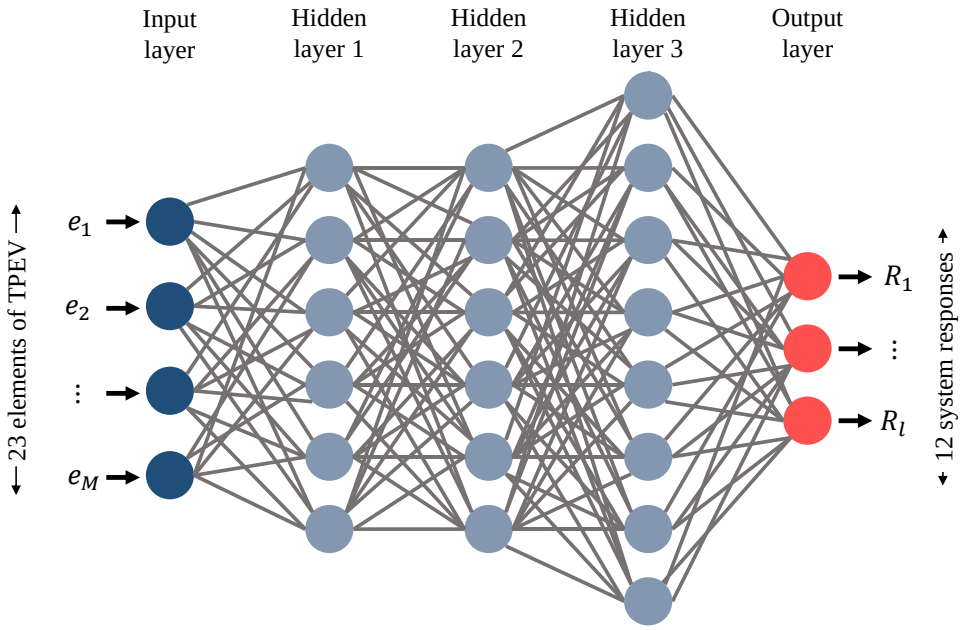

Fig. 4.7. MLP model architecture

Table 4.4. System responses of interest

Performance system response		Economic system response	
Name	Symbol	Name	Symbol
Gross weight	GW	RDT&E cost	$C_{RDT\&E}$
Maximum noise level	$OASPL_{max}$	Vehicle cost	$C_{vehicle}$
Battery energy capacity	E_{bat}	Direct operating cost	C_{DOC}
Effective lift to drag ratio	$LtoD_e$	Yearly operational days	Day_{oper}
Maximum motor power	$P_{motor_{max}}$	Battery life cycle	LC_{bat}
		Maintenance cost	$C_{DOC_{mnt}}$
		Battery replacement cost	$C_{bat_{replace}}$

As described at Section 3.2.2, epistemic uncertainty that occurs by adopting the surrogate model should be considered. In order to capture the epistemic uncertainty of MLP model, MC dropout was carried out. MC dropout is a renowned method for representing model uncertainty in the deep learning section as approximate Bayesian inference [106]. The schematic diagram for the concept of MC dropout is presented in Fig. 4.8 [115]. By randomly breaking links between layers of the MLP model repetitively, the output parameters estimated by the MLP model can be presented using expectation value with standard deviation. The calculated standard deviation represents the model uncertainty of the MLP model. A detailed descriptions about MC dropout can be found in Ref. [106]. The number of dropout executions in this study was 1,000 that is enough to capture the epistemic uncertainty in the MLP model.

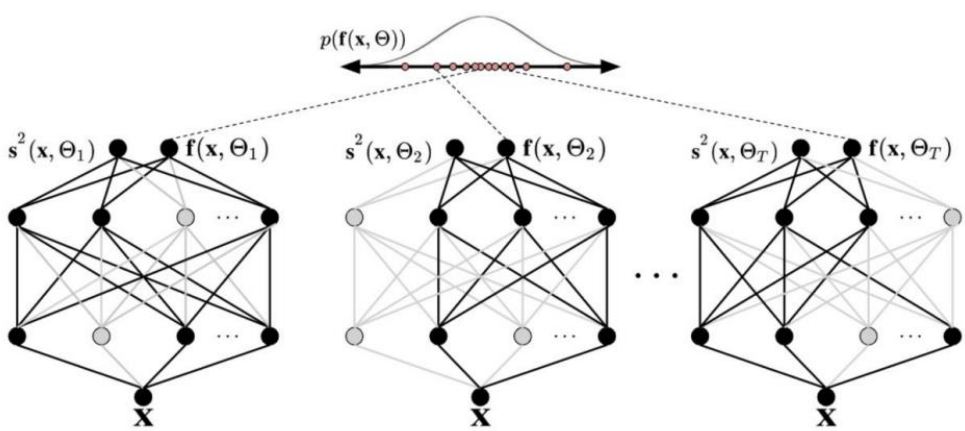

Fig. 4.8. Schematic diagram of MC dropout [115]

The reliability of the MLP model was validated by cross-validation shown in Fig. 4.9 where the plots of the 12 output quantities are collocated. The scattered symbols show expectation value, and error bar lines show 3 times of standard deviation meaning a 99.7% confidence interval. The expectation value and standard deviation were obtained by MC dropout at the tested point with 1,000 random samples. The error bar line in the plot for gross weight is enlarged to apparently show area near the diagonal line.

As can be seen in the figure, the scattered symbols are well aligned with the diagonal line, which means the predicted values by the surrogate model are well matched to the actual values of test data. The R-squared values of all output quantities are above 0.988 when calculated based on the expectation values, which implies that the constructed MLP model is accurate enough to replace the design tool.

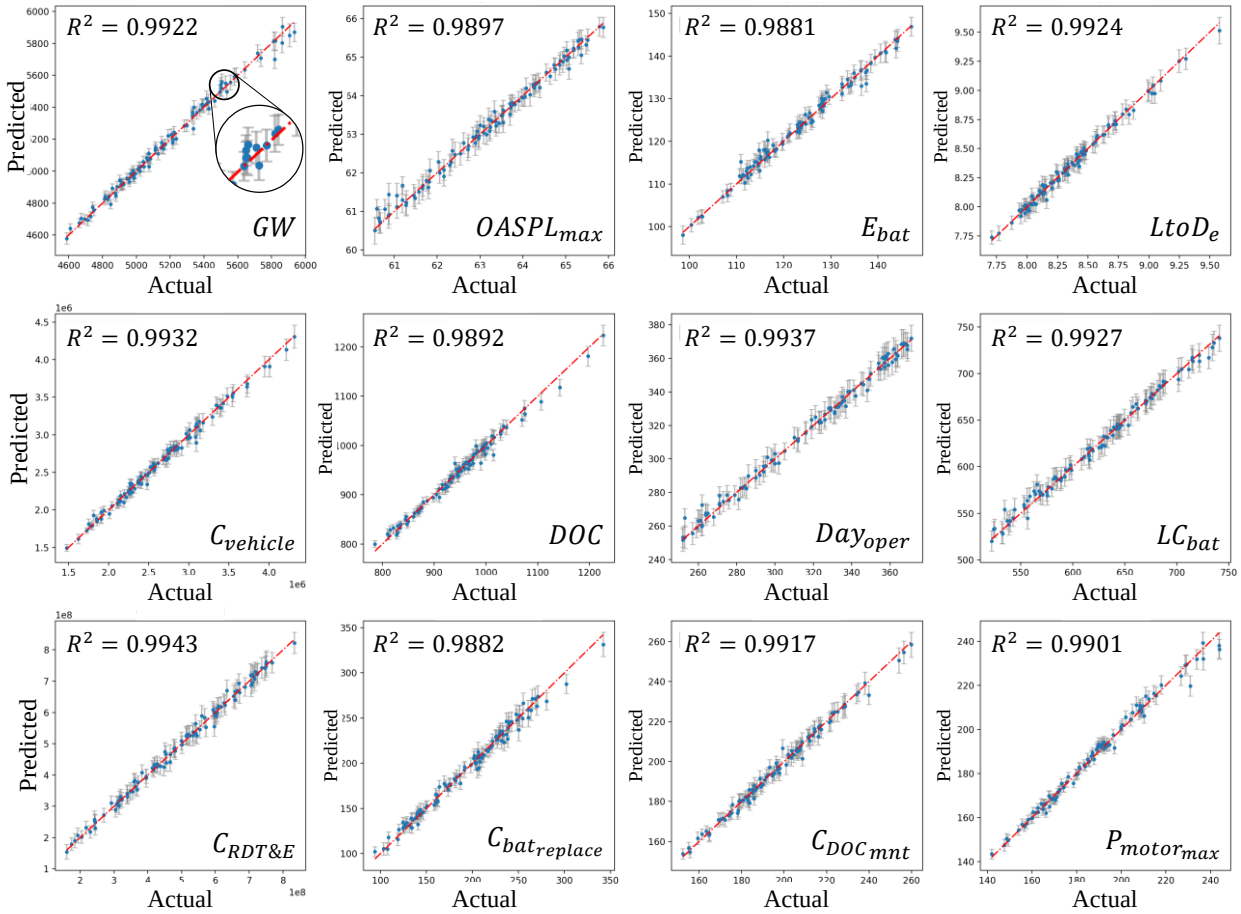

Fig. 4.9. Cross validation of MLP surrogate model with confidence interval by MC dropout

4.1.7. Evaluation with MCS

The MCS process that can be divided three steps shown in Fig. 4.10 is as follows.

1. By LHS, "N_s" number of samples are selected following the designated PDF shape for impact factors in TIM. Herein, 10,000 number of sampled were chosen for each technology portfolio vector. Then, corresponding deterministic TPEM was constructed by Eq. (2.5). The resultant TPEM for the probabilistic simulation was extended to a 3-dimensional array of $[10{,}000] \times [6{,}456] \times [23]$ shape.
2. The deterministic TPEM was fed to the surrogate model (MLP) With the surrogate model $[10{,}000 \times 6{,}456]$ number of cases were evaluated deterministically, resulting in approximately 65 million of raw data for the system responses of interest.
3. The effectiveness indices defined by Eq. (2.7), and (2.8) were calculated for each case and grouped again by alternative design candidates. At certain groups that were expected to be the most favorable technology portfolio, the epistemic uncertainty from the surrogate model was incorporated using Eq. (3.2) if necessary. The statistical moments including expectation, standard deviation, and Pearson's moment skewness coefficient of a system response of interest were calculated by Eq. (3.7), (3.8), and (3.9), respectively. Graphical probabilistic representations such as empirical PDF and CDF could be presented.

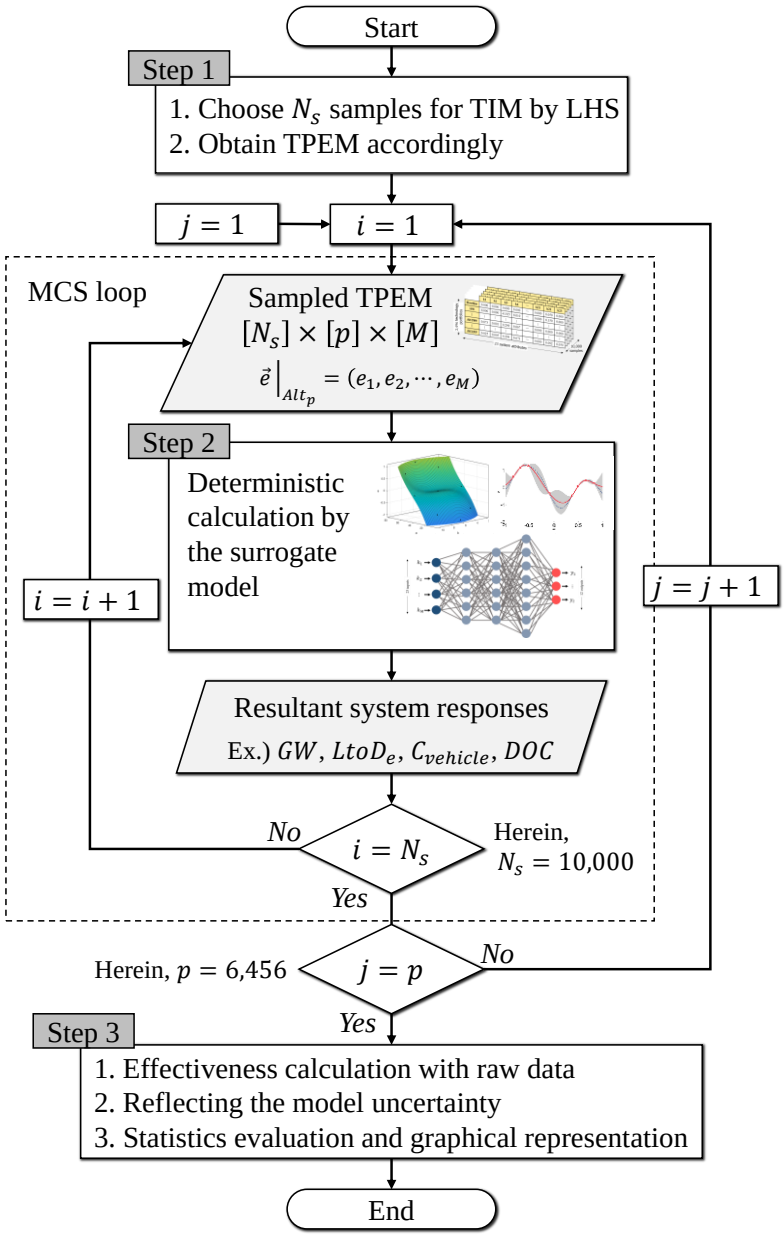

Fig. 4.10. Monte Carlo simulation process for technology portfolio assessment

4.1.8. Selection by Effectiveness

Through MCS with the 6,456 technology portfolios for which 10,000 samples were selected, approximately 65 million cases were evaluated. Using Eqs. (2.7), and (2.8) the result of the MCS was represented by the effectiveness indices for easier determination. The four performance parameters and economics parameters were selected for the PE and EE calculation, respectively. They are tabulated in Table 4.5 with threshold values and the equations are presented as Eq. (4.1) and (4.2). The SE was calculated by Eq. (4.3) with the weight factor on EE is 0.65.

The two effectiveness indices except for SE and RDT&E cost of all alternative design candidates are presented using a three-dimensional scatter plot as shown in Fig. 4.11. The scattered symbols show mean values obtained by averaging MCS results and they were classified by the number of selected technologies in each technology portfolio. Red dash-dot lines indicate a threshold line for each axis that would be determined by the project managers or targeted performance criteria. The ideal point, or desirable point, is a combination of the minimum RDT&E, maximum EE, and maximum PE among the all possible solutions. It is guided by supplementary grey-dashed lines for clear visualization in the figure.

Table 4.5. Parameters for effectiveness calculation for the project

	Parameter	Symbol	Weight	Threshold value	
Performance parameter	Gross weight	GW	0.35	5000	[lb]
	Maximum noise level	$OASPL_{max}$	0.25	65	[dBA]
	Effective lift to drag ratio	$LtoD_e$	0.25	9.0	·
	Battery energy capacity	E_{bat}	0.15	120	[kWh]
Economics parameter	Vehicle cost	$C_{vehicle}$	0.25	2.5M	[USD]
	Direct operating cost	DOC	0.55	750	[USD/FH]
	Yearly operational days	Day_{oper}	0.10	250	[days]
	Battery cycle	LC_{bat}	0.10	650	[times]

$$PE_p = 0.35 \cdot \left(\frac{GW|_{Alt_p}}{GW|_{BL}}\right)^{-1} + 0.25 \cdot \left(\frac{OASPL_{max}|_{Alt_p}}{OASPL_{max}|_{BL}}\right)^{-1} + 0.25 \cdot \left(\frac{LtoD_e|_{Alt_p}}{LtoD_e|_{BL}}\right)^{1} + 0.15 \cdot \left(\frac{E_{bat}|_{Alt_p}}{E_{bat}|_{BL}}\right)^{-1} \quad (4.1)$$

$$EE_p = 0.25 \cdot \left(\frac{C_{vehicle}|_{Alt_p}}{C_{vehicle}|_{BL}}\right)^{-1} + 0.55 \cdot \left(\frac{DOC|_{Alt_p}}{DOC|_{BL}}\right)^{-1} + 0.10 \cdot \left(\frac{Day_{oper}|_{Alt_p}}{Day_{oper}|_{BL}}\right)^{1} + 0.10 \cdot \left(\frac{LC_{bat}|_{Alt_p}}{LC_{bat}|_{BL}}\right)^{1} \quad (4.2)$$

$$SE_p = 0.35 \cdot PE_p + 0.65 \cdot EE_p \quad (4.3)$$

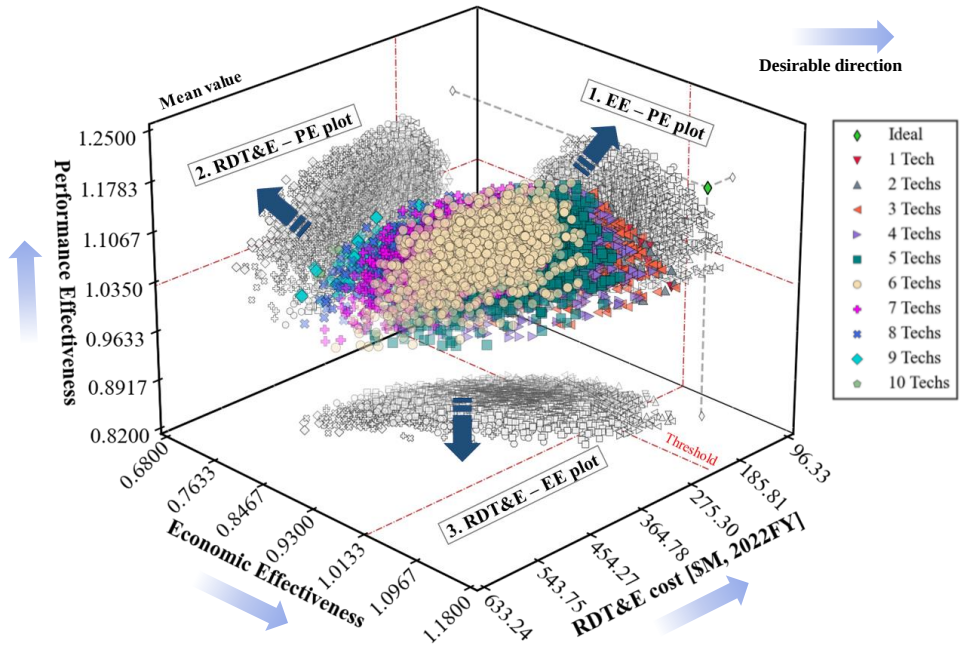

Fig. 4.11. 3D scatter plot of the PE, EE and RDT&E cost

From the 3D scatter plot, three 2D scatter plots can be obtained by projection to each pane: 1) EE-PE plot, 2) RDT&E-PE plot, and 3) RDT&E-EE plot.

EE-PE plot

The first EE-PE plot is shown in Fig. 4.12. This plot shows the effectiveness of the technology portfolios only from the perspective of the possible benefit without consideration of RDT&E cost. The clustered points are surrounded by a convex hull line showing the edge of the result. Since the higher effectiveness implies the resultant effect of technology infusion is beneficial in the system level, (max-max) quadrant is a desirable space in the EE-PE plot. Based on the threshold values in Table 4.5, the threshold lines are drawn for each effectiveness, and the number of desirable solutions is only 60. Note that a solution that did not satisfy the single

threshold value for system response was ruled out even if the calculated effectiveness would exceed the threshold line.

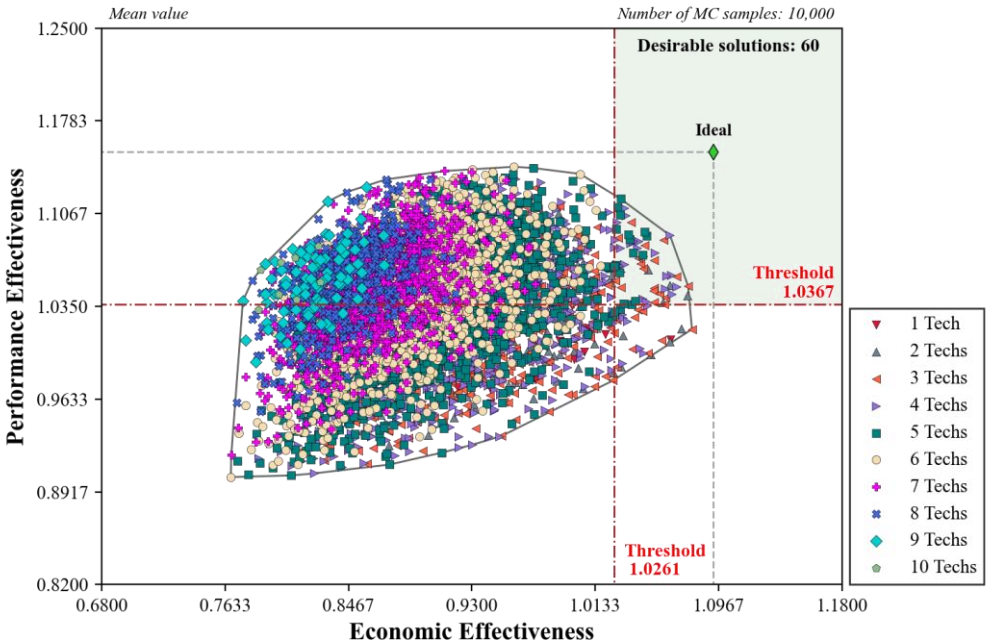

Fig. 4.12. Overview of EE-PE plot

In order to focus on the desirable solutions, the (max-max) quadrant was enlarged and additional information was marked that is shown in Fig. 4.13. Among the 60 desirable solutions, 9 Pareto solutions could be obtained based on the ideal point that is a combination of the maximum EE and maximum PE. These Pareto solutions are non-dominated solutions that were derived by changing the weight for each effectiveness. The three solutions from the Pareto front for which technology combination was noted could be representative solutions that draw interest of the project manager. It is noted that the notations of technologies were joined with cross mark to emphasize the method of TPEV calculation is based on the product-based approach. Two of the representative solutions are one-sided objective-oriented

solutions: solutions for maximum EE, and maximum PE. For the maximum EE, the combination of "$T_2 \times T_7 \times T_{17}$" is the best solution, and the combination of "$T_1 \times T_7 \times T_9 \times T_{15} \times T_{17}$" is the best solution for the maximum PE. The last solution of the final candidates is so called "the best compromise solution" which is the nearest point from the ideal value. The combination of "$T_2 \times T_7 \times T_9 \times T_{17}$" shows the shortest distance from the ideal point in EE-PE plot.

These three solutions were chosen by averaged mean values of MCS output because the mean values can show the direction of the response change by impact of the technology portfolios. Although the mean-value-presenting plot is not that different to the deterministic approach of decision-making from the perspective of that users checked only a single point value, it has a primary role as the first step of filtering out unnecessary information from millions of MCS calculation results.

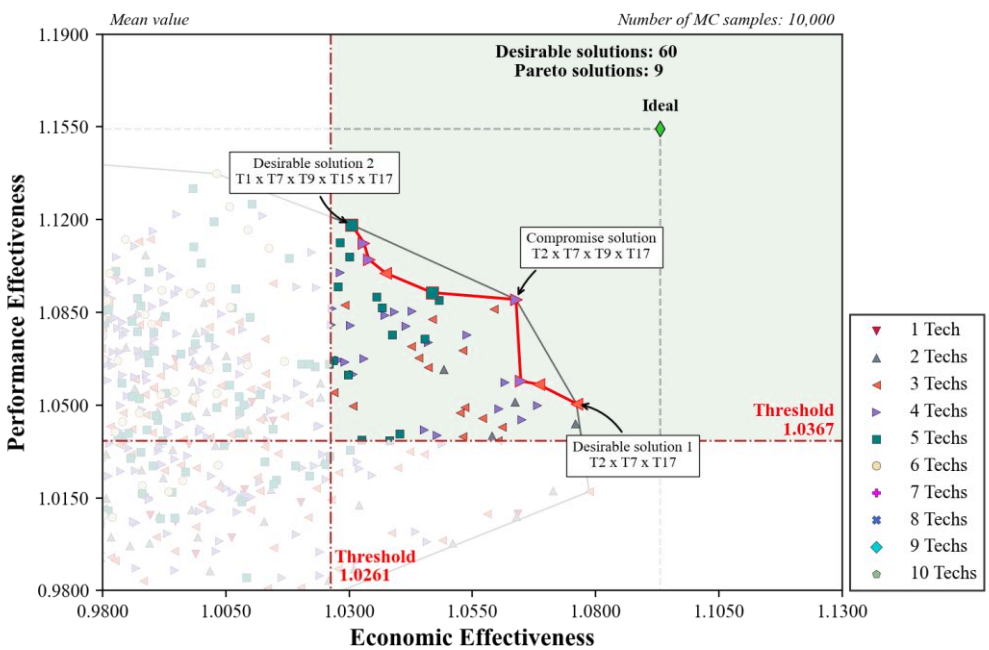

Fig. 4.13. Desirable-quadrant-enlarged EE-PE plot

In addition to the mean-value-based EE-PE plot, a scatter plot to help the probabilistic approach of decision-making was drawn using raw data of MSC results. The MCS scatter of EE-PE plot is shown in Fig. 4.14. There are clustered points around the centered symbol. The centered symbols indicate the mean value used in Fig. 4.13, and clustered small dots are every single evaluation of MCS for each technology portfolio. For clarity, only points of the Pareto solutions were added. There are two elliptical dashed lines in Fig. 4.14 to show the confidence ellipse indicating 3 times of standard deviation (3-sigma or 3-σ) area that encircles 98.89% of the raw data points in 2-dimensional distribution [116]. The horizontally long ellipse lines imply that the variance in EE is more significant than that in PE.

The inner grey dashed line was obtained without incorporating the model uncertainty in the MLP model. It shows a pure aleatory uncertainty effect from the distribution of TIM values. The outer green dashed line was obtained with the addition of the model uncertainty in the MLP model. Thus, this line shows the total variance including the epistemic uncertainty, which was calculated by Eq. (3.2). It can be seen that the area covered by the confidence ellipse slightly increased when the model uncertainty was incorporated. The magnitude of increase of area, indicating the effect of the model uncertainty, is different depending on the technology portfolio since the constructed surrogate model has different confidence according to the input values.

The solutions of which the confidence ellipses crossed the threshold are displayed faintly with assuming a situation where a decision-maker wants to secure solutions

satisfying the 3-sigma confidence. In that situation, 5 solutions in the desirable quadrant were ruled out, and one of the three desirable solutions determined by mean value were changed: the PE-oriented solution. In the analysis based on mean value, the PE-oriented solution was "$T_1 \times T_7 \times T_9 \times T_{15} \times T_{17}$" combination. However, the original PE-oriented solution has a possibility for violating the EE threshold of approximately 35%, equal to area over the EE threshold line. The EE-oriented solution maintained unchanged due to less variation in PE distribution.

From the MCS scatter, the project manager is able to graphically check the variation of the expected effectiveness by the technologies, then make decisions with visual aids. Depending on the project manager's tendency of risk-taking, the final solution can be changed to anyone in the Pareto front with smaller confidence ellipse.

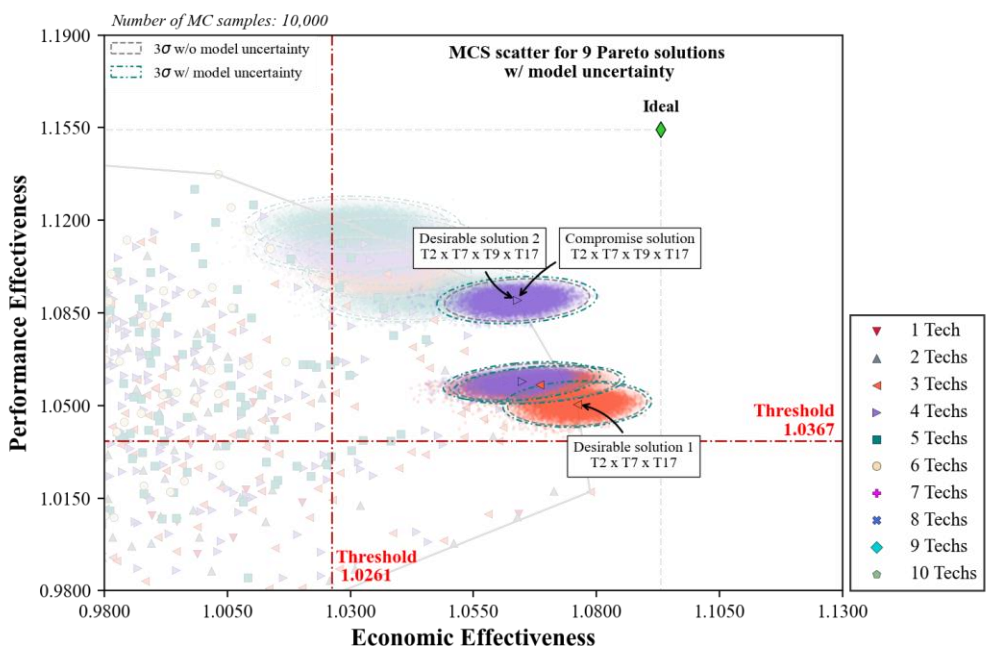

Fig. 4.14. MCS scatter of EE-PE plot

The same visualization approach was applied to the other projection plots: RDT&E-PE plot and RDT&E-EE plot. These RDT&E cost-related plots might draw more interest since budget issues are inevitable and substantially important.

RDT&E-PE plot

Firstly, RDT&E-PE plot is shown in Fig. 4.15. As can be seen, the more technologies were selected in the portfolio, the higher RDT&E cost was required, which is quite natural since more technologies need more effort for development and integration. On the other hand, there was no clear dependency between PE and the number of technologies, implying that more technologies do not always produce a better effective solution. In the RDT&E-PE plot, a desirable space is (min-max) quadrant, and 766 solutions satisfied the two threshold lines.

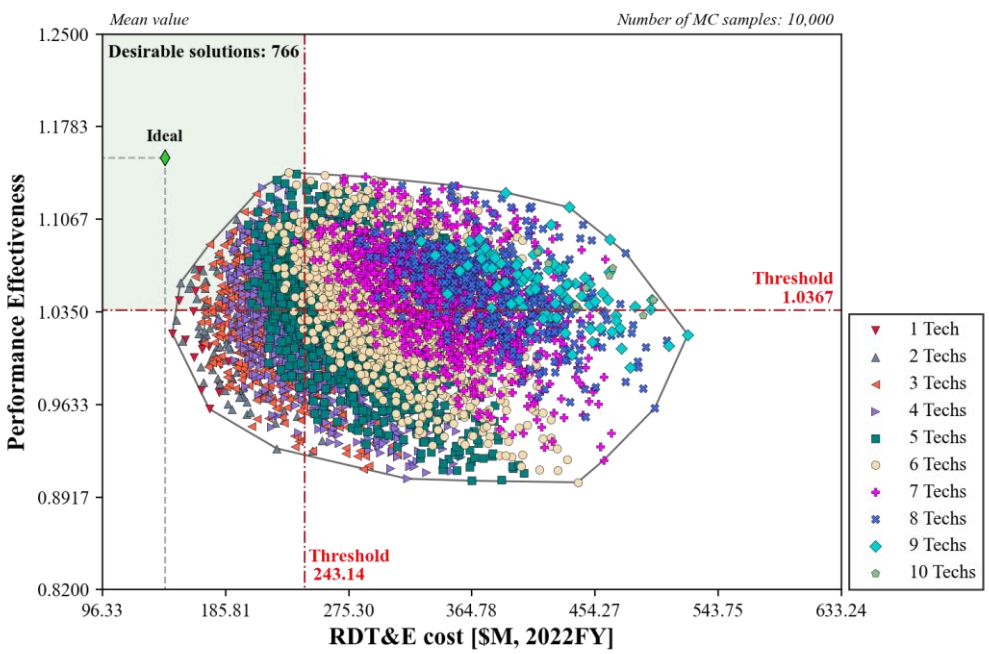

Fig. 4.15. Overview of RDT&E-PE plot

The enlarged desirable quadrant of RDT&E-PE plot is shown in Fig. 4.16 where the mean-value-based solutions are presented. Among in total 766 solutions, 16 Pareto solutions were obtained. The RDT&E-oriented solution is "T_2", PE-oriented solution is "$T_1 \times T_4 \times T_7 \times T_9 \times T_{10} \times T_{15}$" combination, and best compromise solution is "$T_1 \times T_{10} \times T_{12}$".

As mentioned earlier, since more technologies tend to induce the increase of RDT&E cost, the number of technologies in the portfolio for RDT&E cost-oriented solution is only one, T_2. It implies the T_2 was the most influential technology among the portfolios that lay in the desirable quadrant. Meanwhile, the PE-oriented solution has a combination of six technologies, and the compromise solution has a combination of three technologies. In the Pareto solutions, there was a tendency for higher PE with increasing the number of technologies.

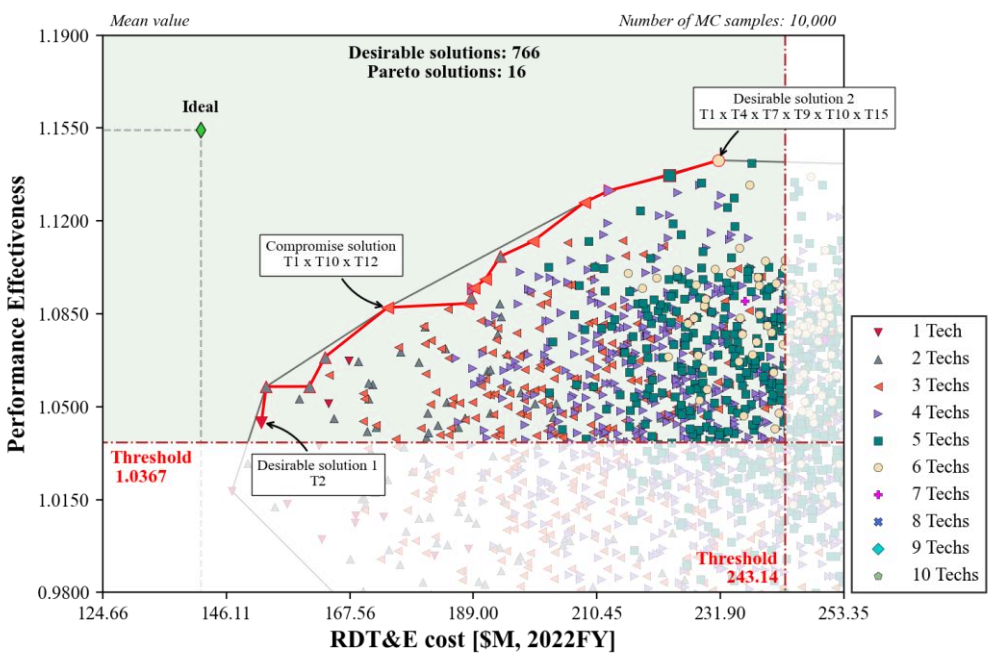

Fig. 4.16. Desirable-quadrant-enlarged RDT&E-PE plot

Two MCS plots for RDT&E-PE distributions are drawn in Fig. 4.17 and Fig. 4.18 according to the application of the model uncertainty. In Fig. 4.17, the confidence ellipse without the model uncertainty is drawn solely. When the pure effect of the aleatory uncertainty was considered, the RDT&E-oriented solution was changed from "T_2" to "$T_1 \times T_{12}$" combination since the distribution of the original solution violated the PE threshold slightly due to the variability. The PE-oriented solution was maintained.

However, when the model uncertainty from the surrogate model was added, the PE-oriented solution was changed to another combination of "$T_1 \times T_4 \times T_7 \times T_9 \times T_{10}$" to secure the 98.89% confidence interval lay in the desirable quadrant perfectly. The original PE-oriented solution showed the violation of the RDT&E threshold with the line crossed. This alternation of the solution showed the reason why the model uncertainty from the surrogate model should be incorporated in the process of technology portfolio assessment.

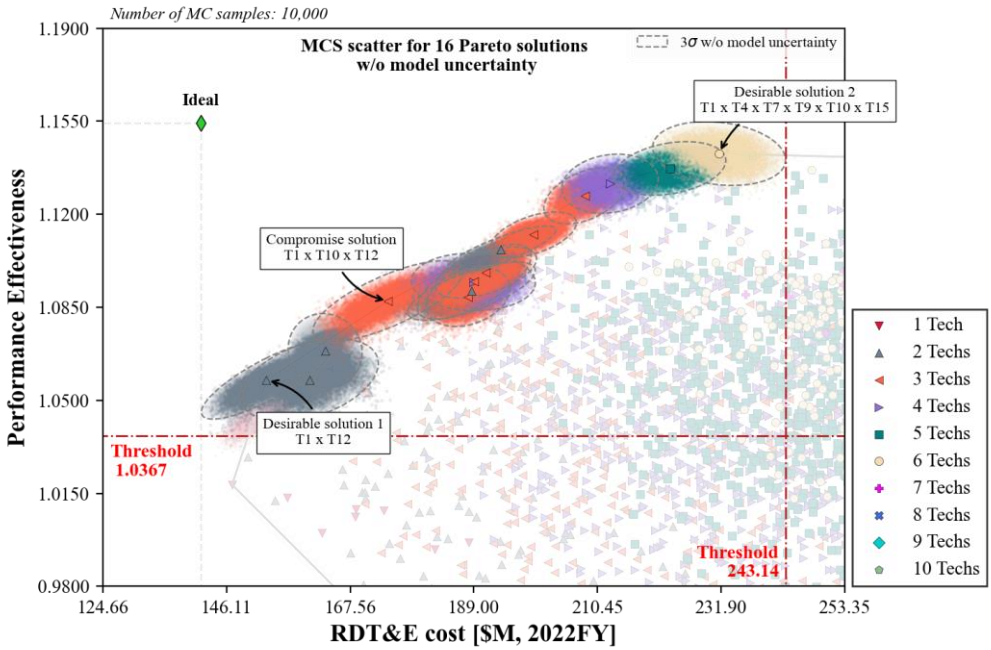

Fig. 4.17. MCS scatter of RDT&E-PE plot without model uncertainty

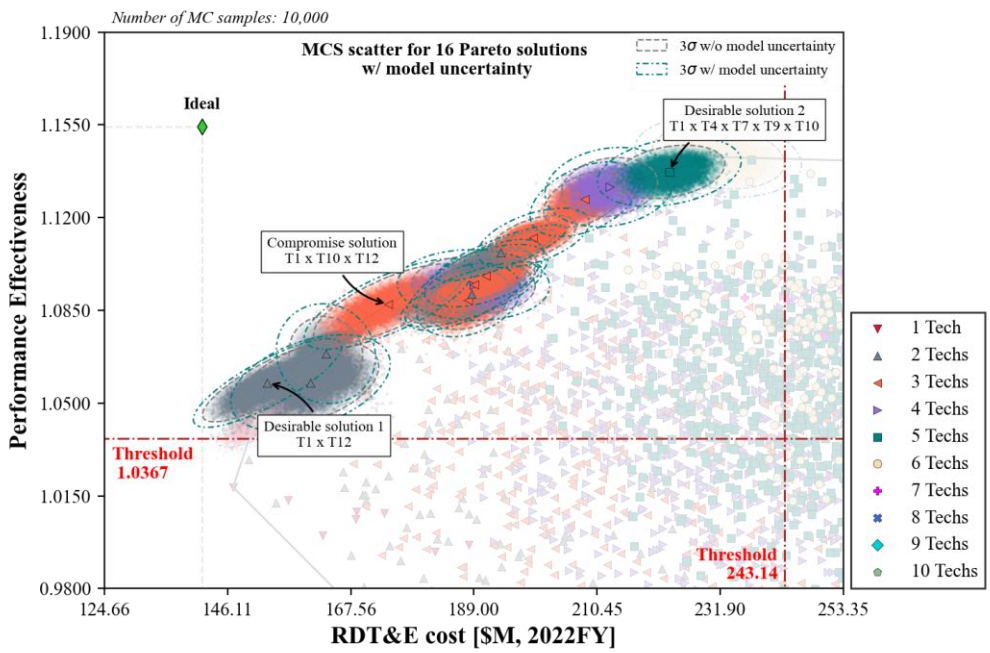

Fig. 4.18. MCS scatter of RDT&E-PE plot with model uncertainty

RDT&E-EE plot

The overview of the RDT&E-EE plot is presented in Fig. 4.19 where the relationship between the two axis values and the number of technologies in a portfolio is apparently shown. A directional arrow heading right-bottom could be obtained by the number of technologies. As the number of technologies in a portfolio increased, EE shows a decreasing trend displaying that the band of EE is going down. Meanwhile, RDT&E cost shows an increasing trend with the increasing number of technologies. The desirable area is the (min-max) quadrant where 60 solutions lay in the area. This number is only 7.8% of the number of solutions in the RDT&E-PE plot, which implies that it is much more difficult to achieve economic benefit than performance benefit even though the target value of the threshold line is lower than that of the PE; 1.0261 for EE and 1.0367 for PE.

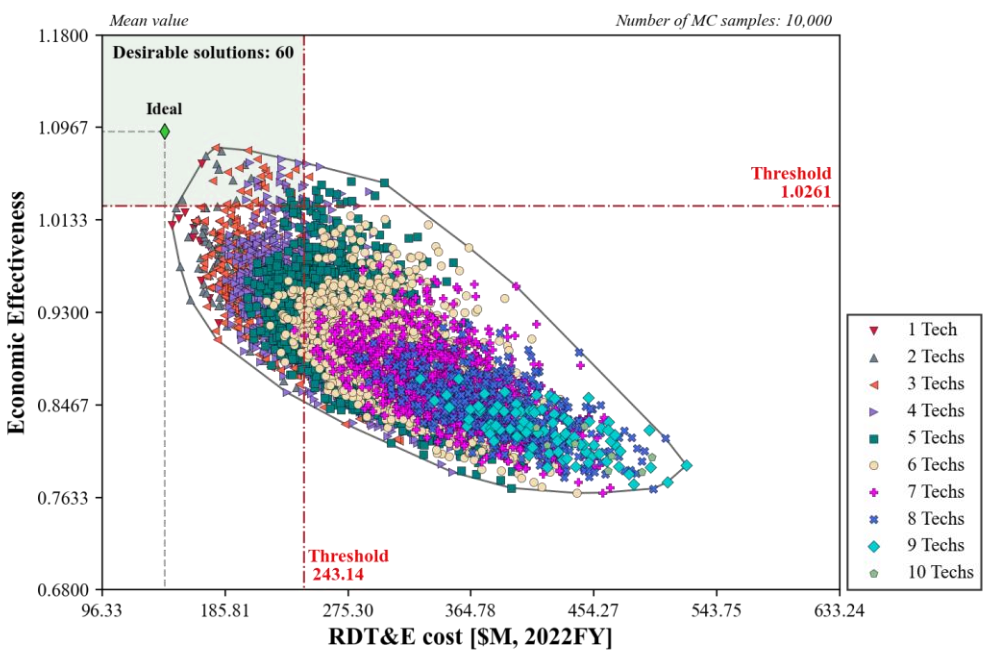

Fig. 4.19. Overview of RDT&E-EE plot

Three desirable solutions from 4 Pareto solutions were obtained and they are shown in Fig. 4.20. The number of technologies in the portfolios for the desirable solution did not exceed three. This is because the increase of RDT&E cost according to technology infusion was reflected in the vehicle cost, which diminished the EE.

When the MSC plots for RDT&E-EE distributions are displayed in Fig. 4.21 and Fig. 4.22, different and similar situations observed in the RDT&E-PE plots occurred simultaneously. The different situation is that the three desirable solutions were not changed when the pure effect of the aleatory uncertainty was considered. The RDT&E-oriented solution has low variability, so that the solutions were maintained in Fig. 4.21. Nevertheless, when the model uncertainty was applied, the desirable solution was changed from "$T_7 \times T_{16}$" to "T_{17}" since the original RDT&E-oriented solution barely satisfied the EE threshold.

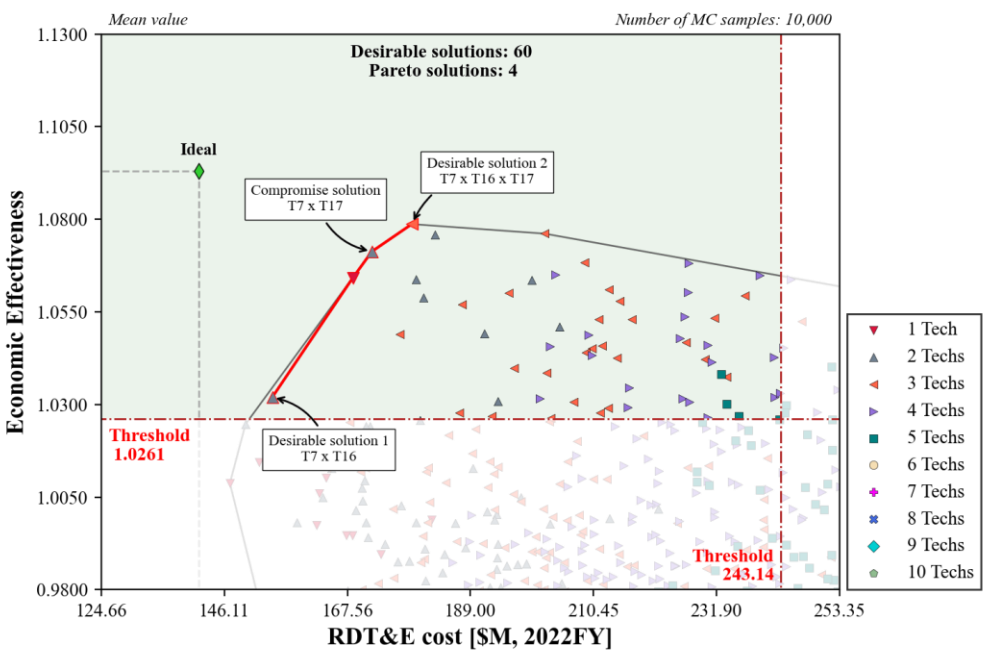

Fig. 4.20. Desirable-quadrant-enlarged RDT&E-EE plot

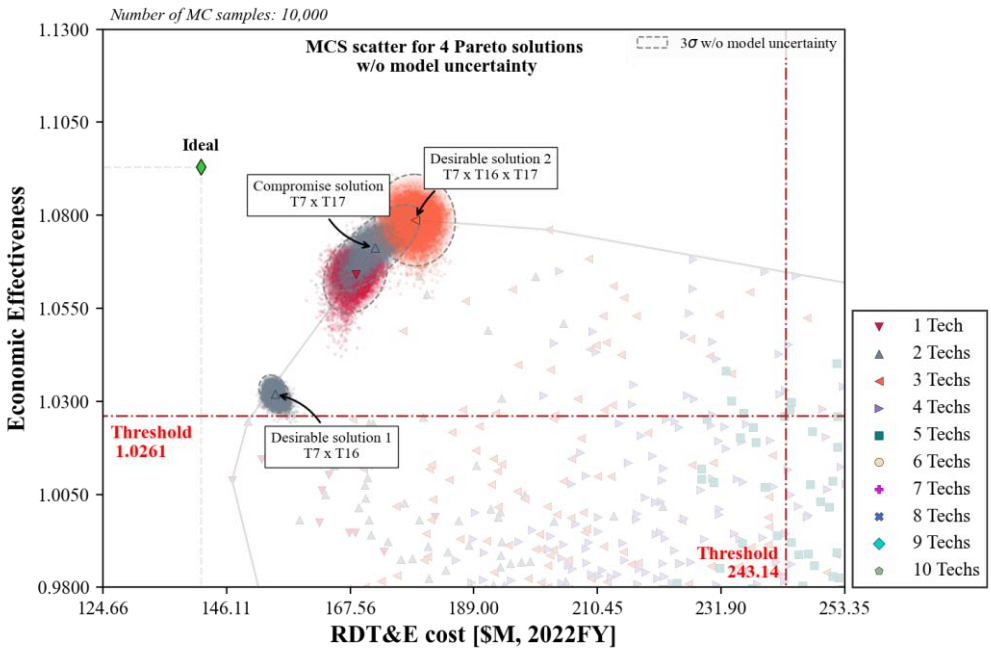

Fig. 4.21. MCS scatter of RDT&E-EE plot without model uncertainty

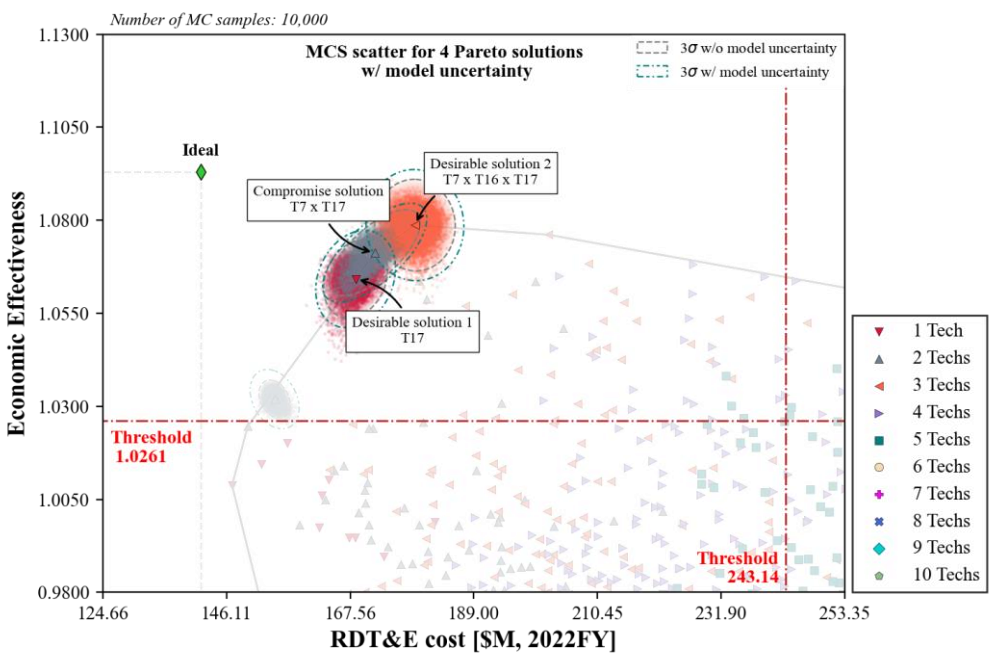

Fig. 4.22. MCS scatter of RDT&E-EE plot with model uncertainty

RDT&E-SE plot

Lastly, system effectiveness, SE, obtained by Eq. (4.3) was plotted with RDT&E cost. For brevity enlarged quadrant plot and MCS plot with model uncertainty are displayed in Fig. 4.23 and Fig. 4.24, respectively. The desirable solutions were changed when the criteria were based on the uncertainty-based analysis.

The three desirable solutions partially share the selected technologies with those obtained from the RDT&E-PE plot and RDT&E-EE plot. Since the more weight of 0.65 was imposed on EE, the desirable solutions had T_7 or T_{17} in their portfolio which were arose in the analysis of the RDT&E-EE plot. If the weight factor moved to the PE in Eq. (4.3), the solutions would follow the trend in the RDT&E-PE plot.

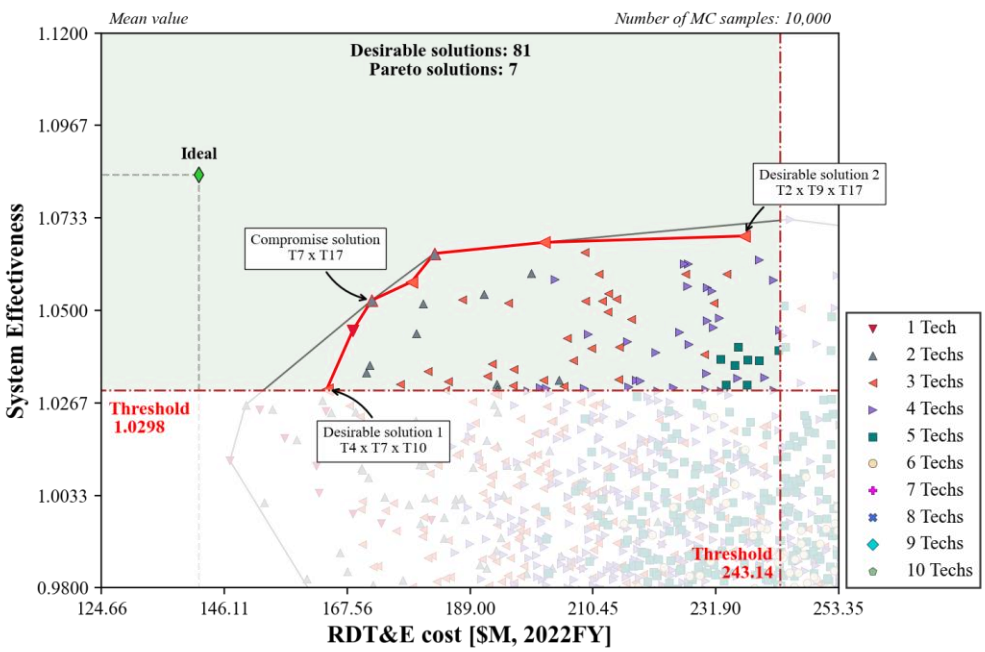

Fig. 4.23. Desirable-quadrant-enlarged RDT&E-SE plot

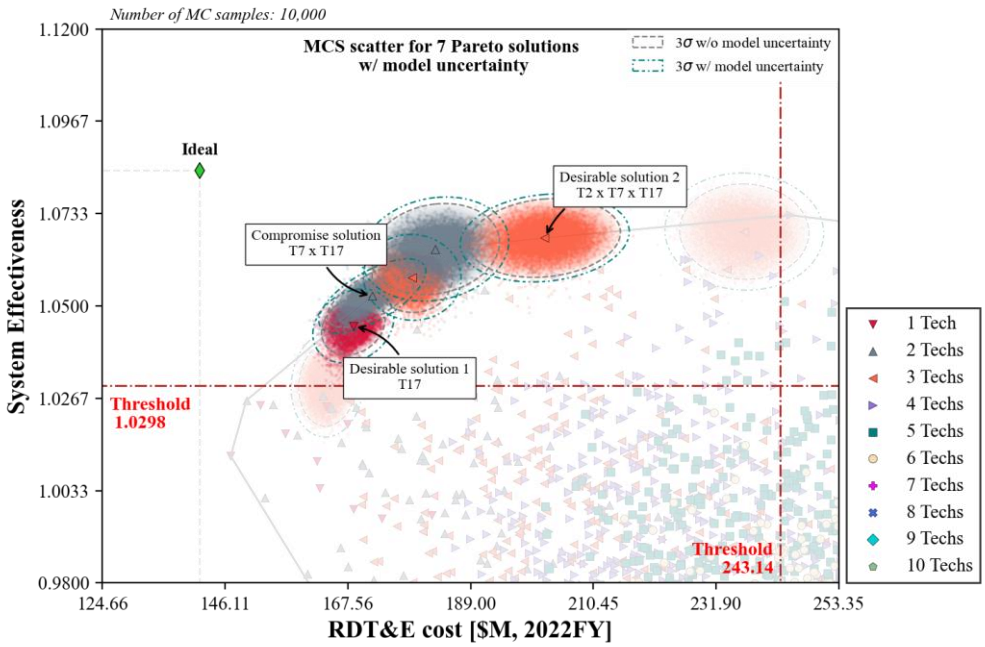

Fig. 4.24. MCS scatter of RDT&E-SE plot with model uncertainty.

As seen so far, the desirable solutions were different in terms of effectiveness indices and incorporation of the uncertainties. The desirable solutions that could be possibly selected technology portfolios in terms of each effectiveness perspective are tabulated in Table 4.6. The solutions that were determined based on the mean value and the 3-sigma rule without or with the model uncertainty are presented simultaneously. The compromise solutions are presented only once since there was no change for them depending on the model uncertainty. It is noted that the determined technology portfolio has a different technology combination in some cases; they are colored differently for legibility.

Additionally, the final shortlist of technology portfolios for each effectiveness index tend to have certain technologies in common. In terms of the performance effectiveness, T_1 of lithium-sulfur battery cell is always included in the final shortlist of technology portfolios. Since this fact implies that T_1 is one of the most influential technologies on the performance effectiveness, the project managers should contain this technology in the project technology roadmap if they choose to achieve high performance effectiveness. Similarly, when seeing the shortlist of technology portfolios in the economic effectiveness, the three technologies appeared alternately; T_7-battery package integration, T_{16}-surface coating for anti-icing, and T_{17}-fast production technology. These technologies were selected due to cost-lowering characteristics; reducing the maintenance cost (T_7) or increasing operable days (T_{16}), or decreasing vehicle acquisition cost (T_{17}). Using this information, the project managers could plan the technology roadmap for the success of development program with their own philosophy and objectives, which is the development purpose of the technology portfolio assessment framework.

Table 4.6. Summary of the desirable solutions from the various effectiveness plots

	EE-PE plot	**RDT&E-PE plot**	**RDT&E-EE plot**	**RDT&E-SE plot**
Ideal point	(1.0931, 1.1545)	(141.6586, 1.1545)	(141.6586, 1.0931)	(141.6586, 1.0842)
Desirable solution 1 (by avg.)	(1.0761, 1.0506) by T_2, T_7, T_{17}	(152.2119, 1.0441) by T_2	(154.4596, 1.0319) by T_7, T_{16}	(163.9885, 1.0301) by T_4, T_7, T_{10}
Desirable solution 1 (by pure aleatory)	(1.0761, 1.0506) by T_2, T_7, T_{17}	(153.0405, 1.0576) by T_1, T_{12}	(154.4596, 1.0319) by T_7, T_{16}	(168.5097, 1.0449) by T_{17}
Desirable solution 1 (by total variability)	(1.0761, 1.0506) by T_2, T_7, T_{17}	(153.0405 , 1.0576) by T_1, T_{12}	(168.5097, 1.0642) by T_{17}	(168.5097, 1.0449) by T_{17}

Desirable solution 2 (by avg.)	(1.0305, 1.1180) by T_1, T_7, T_9, T_{15}, T_{17}	(231.5764, 1.1429) by T_1, T_4, T_7, T_9, T_{10}, T_{15}	(178.8044, 1.0787) by T_7, T_{16}, T_{17}	(236.8373, 1.0688) by T_2, T_9, T_{17}
Desirable solution 2 (by pure aleatory)	(1.0639, 1.0898) by T_2, T_7, T_9, T_{17}	(231.5764, 1.1429) by T_1, T_4, T_7, T_9, T_{10}, T_{15}	(178.8044, 1.0787) by T_7, T_{16}, T_{17}	(201.9673, 1.0672) by T_2, T_7, T_{17}
Desirable solution 2 (by total variability)	(1.0639, 1.0898) by T_2, T_7, T_9, T_{17}	(223.0341, 1.1372) by T_1, T_4, T_7, T_9, T_{10}	(178.8044, 1.0787) by T_7, T_{16}, T_{17}	(201.9673, 1.0672) by T_2, T_7, T_{17}
Compromise solution (by avg.)	(1.0639, 1.0898) by T_2, T_7, T_9, T_{17}	(174.1401 , 1.0874) by T_1, T_{10}, T_{12}	(171.8250, 1.0713) by T_7, T_{17}	(171.8250, 1.0525) by T_7, T_{17}

4.2. Sizing of eVTOL under uncertainties in conceptual design

In this section, eVTOL sizing with uncertainties in the conceptual design phase was conducted considering the various uncertainties described in Section 3.3. The variance in performance and weight of the eVTOL by physical variation in components and analysis modules were quantified under two flight conditions: single hover and a generic mission profile. The details of uncertainty quantification conditions were presented in each related section, respectively.

4.2.1. Test Bed eVTOL

The baseline of a hypothetical eVTOL aircraft configuration is identical to the reference vehicle described in Section 4.1.1 earlier; vectored thrust configuration with six tilting rotors and a T-shaped empennage system (Fig. 4.1). Meanwhile, the exact numbers for the geometric specification and the mission profile are a little bit different and modified. They are presented in each related section.

4.2.2. Uncertainty Identification

Based on the categorization of uncertainties described in Section 3.3, aleatory and epistemic uncertainties were identified.

For the aleatory uncertainty, physical variation of geometric parameters in major components of the eVTOL was selected as in Table 4.7. There are eleven parameters related to the rotor design, wing position, and electric propulsion system. In the rotor-related parameters, rotor radius, blade chord length, rotational speed, and blade twist

were selected. In the wing-related parameter, the wing incidence angle was selected as parametric uncertainty. In the electric propulsion components, efficiency coefficients for the electric motor, inverter, and battery were selected as the parametric uncertainty. In addition to them, the variations of specific power for the electric motor, inverter, and specific energy were selected as the parametric uncertainty in order to replicate the situation where the representative performance indices were not obtained with a given fixed weight for each component.

These eleven parameters have an inherent variance of the value due to various reasons. For instance, manufacturing tolerance, local flight condition variation, and physical damages and weathering could result in variance in the rotor-related geometric parameters. Accuracy and tolerance of control mechanism and algorithm, electromagnetic interference, weathering, erosion in wiring, and aging effect could result in variance in the electric parameters. All parametric uncertainties were modeled using Gaussian distribution in this study because it is natural to assume that manufacturers try to make the components to have a specific value. The COVs, defined as Eq. (3.3), for each parameter were assigned based on literature surveys [39,117,118] and knowledge of experts. Depending on the problem definition of uncertainty quantification, the parametric uncertainties were considered or not.

Table 4.7. List of parametric uncertainty of eVTOL and fixed parameters

Component	Variable		Distribution type	Nominal value	COV [%]
Rotor	R_{rotor}	[ft]	Gaussian	4.421	0.1
	c_{rotor}	[ft]	Gaussian	0.8320	0.2
	Ω_{rotor}	[RPM]	Gaussian	1020	2.0
	tw_{rotor}	[deg]	Gaussian	-40.112	0.5
Wing	α_{winc}	[deg]	Gaussian	2.68	2.0
Electric Propulsion	η_{mot}	·	Gaussian	0.96	0.6
	η_{inv}	·	Gaussian	0.98	0.4
	η_{bat}	·	Gaussian	0.97	0.7
	SP_{mot}	[kW/kg]	Gaussian	4.932	2.0
	SP_{inv}	[kW/kg]	Gaussian	13.00	2.0
	SE_{bat}	[Wh/kg]	Gaussian	205.0	2.0
Fixed gross weight				Fixed battery weight	
4965.914 lb (2252.50 kg)				1596.660 lb (724.233 kg)	

The epistemic uncertainty in the conceptual design module was modeled by adopting the model uncertainty parameter defined and obtained in Section 3.3.2 with Eqs. (3.5) and (3.6). As with the aleatory uncertainty, the application of the model uncertainty parameters depends on the definition of the following uncertainty quantification problems.

4.2.3. MCS process

The MCS process is shown in Fig. 4.25 where four steps are presented. Iterative deterministic calculations are conducted using sampled input parameters. During MCS, the optimization process of RISPECT+ was excluded and the sizing process was only executed. The statistical outcomes by Eqs. (3.7), (3.8), (3.9), and (3.10) are the final result of the MCS process

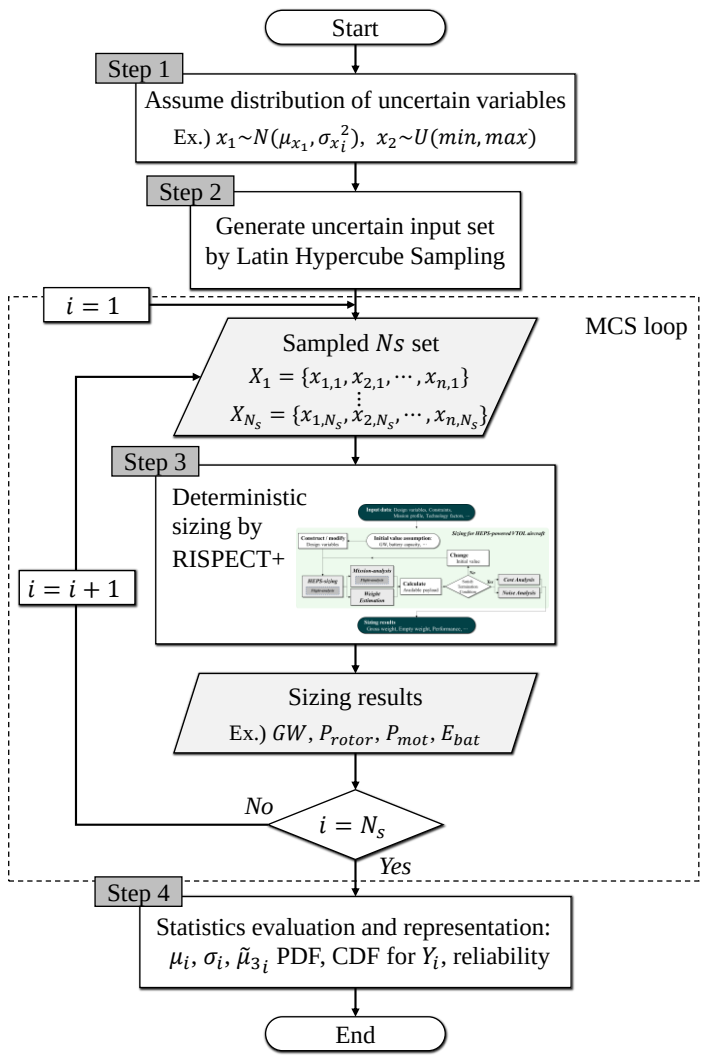

Fig. 4.25. Monte Carlo simulation process for sizing

4.2.4. Sensitivity Study

Sample number test

In order to determine the appropriate number of samples for MCS, a sample number test was conducted with six different numbers of samples: 100, 300, 500, 1,000, 10,000, and 100,000. According to each number of samples, the expectation and standard deviation were calculated in terms of five performance parameters: final depth of discharge DoD_{fin}, mechanical power of a rotor P_{rotor}, battery discharge C-rate χ_{bat}, maximum overall sound pressure level with A-weighting $OASPL_{max}$, and system efficiency η_{sys}. The η_{sys} was calculated by multiplying all efficiency coefficients of the propulsion components (the rotor, motor, inverter, and battery). Geometric input parameters are the same as Table 4.7 and 10 min hovering flight at altitude of 200 m was imposed. The convergence trends are shown in Fig. 4.26 and Fig. 4.27 in terms of the expectation and standard deviation. They are presented as relative differences from the value obtained with 100,000 samples, assuming that results with 100,000 samples are true values. Convergence criterion was set as deviation of 1%. As can be seen, the MCS result with 10,000 samples satisfies the criterion sufficiently in both the expectation and standard deviation of the five performance indices. Hence, the following MCS results were obtained with the simulation of 10,000 samples.

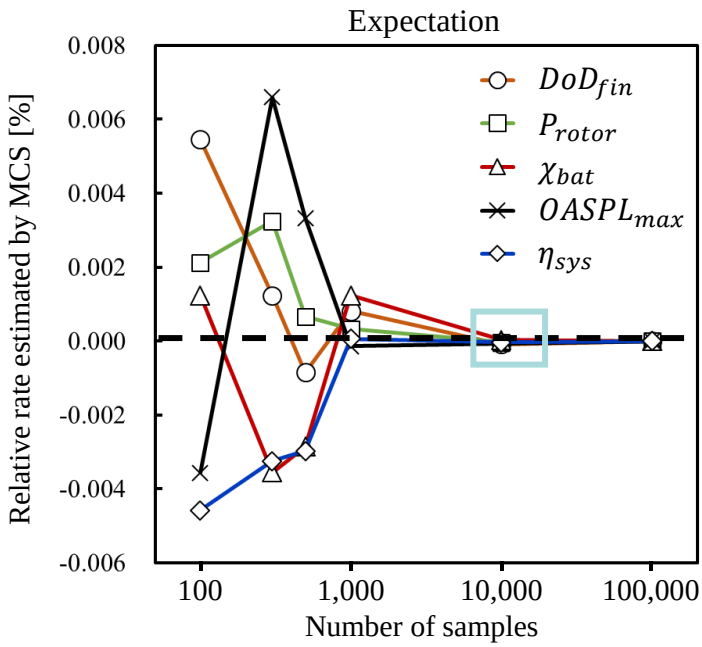

Fig. 4.26. Sample number test results: expectation

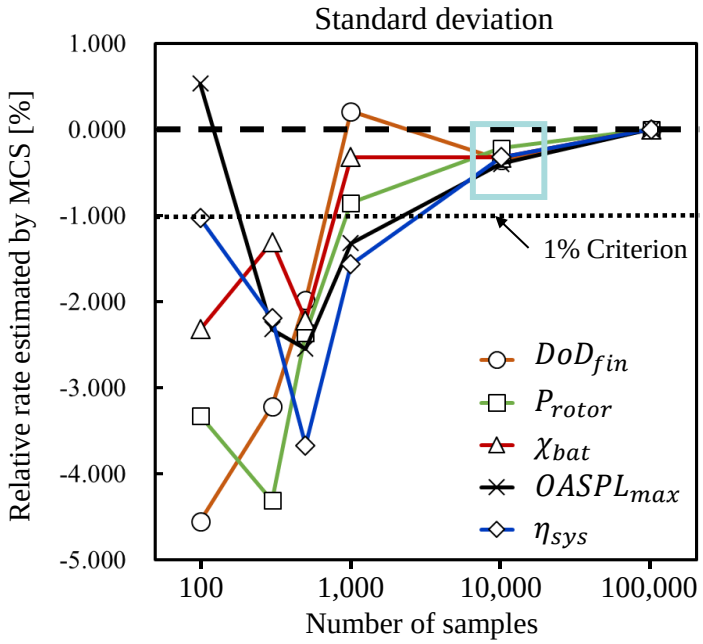

Fig. 4.27. Sample number test results: standard deviation

Sensitivity study

In order to investigate the single effect of each parametric uncertainty on the performance and filter out less influential uncertain parameters, the sensitivity of the uncertain geometric parameters was studied firstly. The sensitivity study was conducted under 10 minutes of hovering flight. The input condition is presented in Table 4.8. The sensitivity of the uncertainties was measured using sensitivity index SI defined by Eq. (4.4) where x_i is an uncertain variable in the input set, and y_j is output performance parameters. $y_j|x_i$ means that the conditional output parameter of y_i when an uncertain input parameter is x_i.

$$SI_{i,j} = \frac{COV\ of\ y_j|x_i}{COV\ of\ x_i} = \frac{(\sigma/\mu)_{y_j|x_i}}{(\sigma/\mu)_{x_i}} \tag{4.4}$$

Table 4.8. Parametric uncertainty of the base eVTOL in hover flight

Component	Variable		Distribution type	Nominal value	COV [%]
Rotor	R_{rotor}	[ft]	Gaussian	4.421	0.1
	c_{rotor}	[ft]	Gaussian	0.8320	0.2
	Ω_{rotor}	[RPM]	Gaussian	1020	2.0
	tw_{rotor}	[deg]	Gaussian	-40.112	0.5
Electric Propulsion	η_{mot}	·	Gaussian	0.96	0.6
	η_{inv}	·	Gaussian	0.98	0.4
	η_{bat}	·	Gaussian	0.97	0.7
	SE_{bat}	[Wh/kg]	Gaussian	205	2.0

At first, the sensitivities of the eight input parameters were measured in terms of DoD_{fin} after 10 minutes of hovering flight. DoD_{fin} was selected as a benchmark since the remaining battery energy is the resultant outcome at last when equipped battery energy and hovering time are settled. Hence, the sensitivity rank based on DoD_{fin}, $SI_{x_i,DoD_{fin}}$ were obtained for the eight input parameters. The graphical results are presented in Fig. 4.29 and Fig. 4.30 where histogram with PDF curve and normal probability plots (NPP) with skewness coefficient are displayed. The NPP is a graphical technique to show the deviation of a distribution of data from the ideal normal distribution [119]. If data follow the normal distribution, the samples are aligned with the diagonal line. The offset from the diagonal line indicates that the data follow a skewed distribution. A left-skewed distribution has a concave downward curve (C-shape), and a right-skewed distribution has a concave upward curve (inverted C shape). The S-shape curve indicates that the data follow a long-tailed distribution.

The histograms and NPPs by rotor-related parameters are shown in Fig. 4.29. Except for Ω_{rotor} and tw_{rotor} cases, the distributions of DoD_{fin} were normally distributed by following input normal distributions. A rough histogram by tw_{rotor} was due to the numerical convergence criterion in the BEMT analysis. In the case when the Ω_{rotor} was the uncertain parameter, the distribution of DoD_{fin} showed right skewness. This is because the relationship between Ω_{rotor} and DoD_{fin} had a positive correlation following 3rd order polynomial equation. Following the Eq. (2.13), rotor power P_{rotor} was proportional to the third power of Ω_{rotor}, so the

used battery energy had the same relation when the efficiency coefficients were constant. The distribution of the third power of normal distribution has slightly right skewness in natural. In the tw_{rotor} case, the relationship between tw_{rotor} and P_{rotor} had weak positive correlation. Therefore, the resultant skewness of DoD_{fin} was smaller. The correlations of Ω_{rotor}, tw_{rotor}, and P_{rotor} were presented in Fig. 4.28.

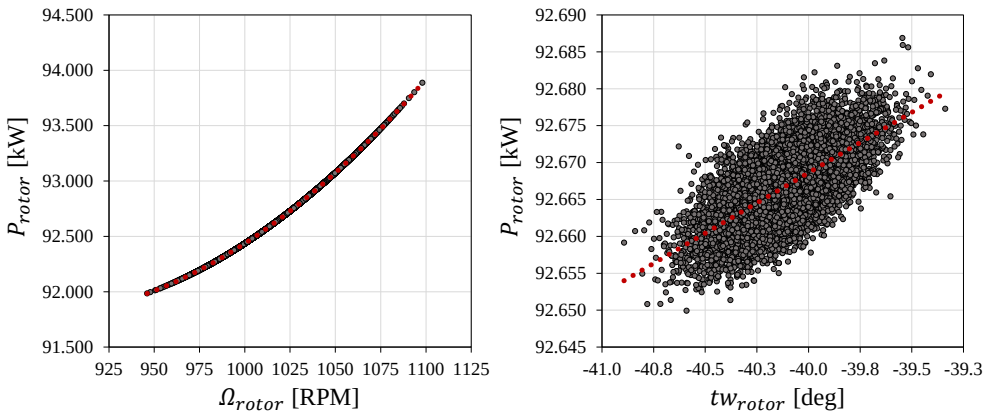

Fig. 4.28. Correlation between Ω_{rotor}, tw_{rotor}, and P_{rotor}

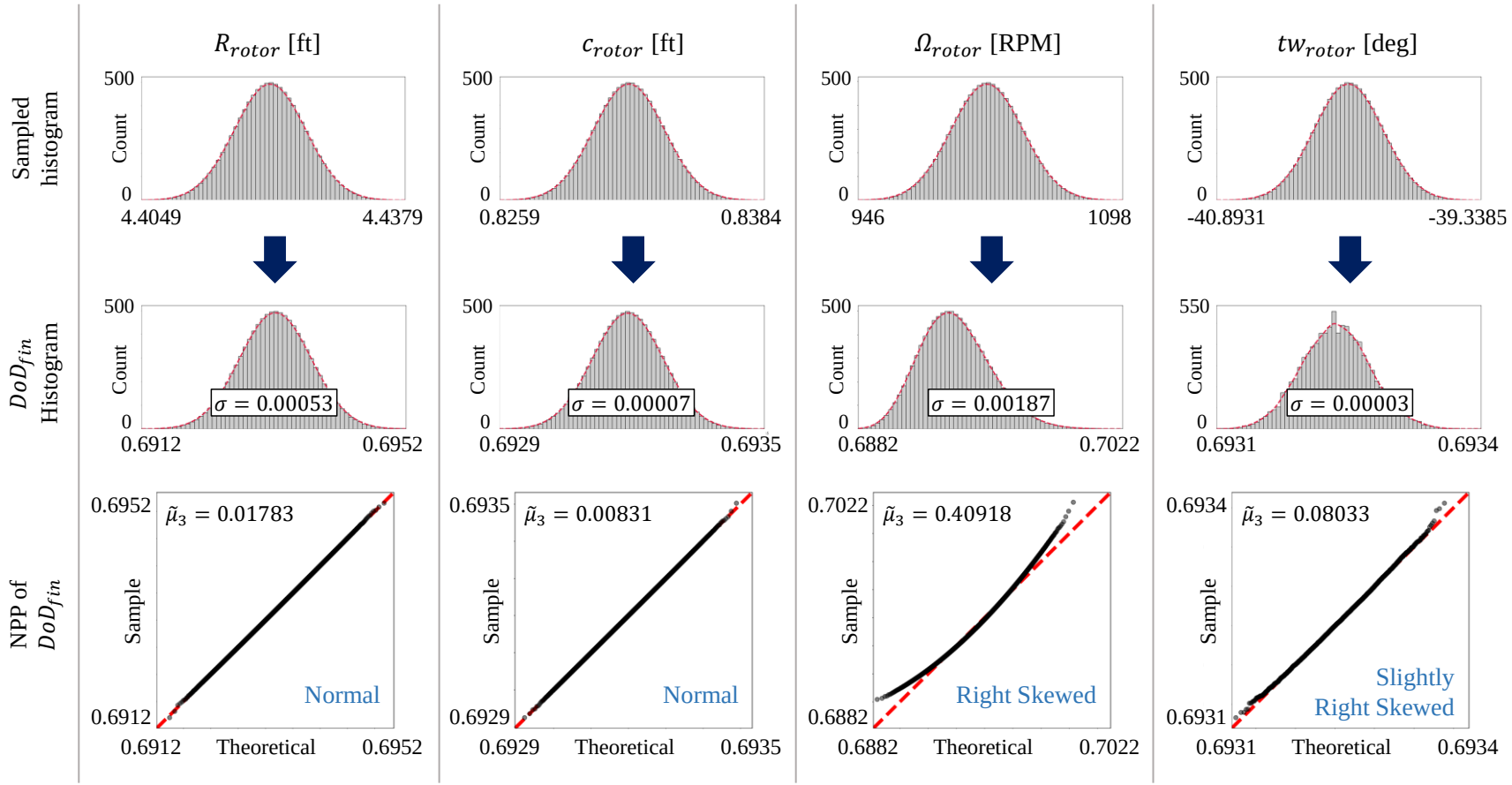

Fig. 4.29. Sensitivity study result of DoD_{fin} by rotor parameters

The histograms and NPPs by electric components-related parameters are shown in Fig. 4.30. At this time, except for SE_{bat} case, the distributions of DoD_{fin} were normally distributed by following the input normal distributions. In the case when the SE_{bat} was the uncertain parameter, the distribution of DoD_{fin} showed slightly right skewness. This is because the relationship between SE_{bat} and DoD_{fin} had an inverse correlation as shown in Eq. (4.5). The distribution of reciprocal of normal distribution has slightly right skewness. Although the other electric efficiency coefficients also have inverse correlations with the electric power (see Eqs. (2.26), (2.30), and (2.31)), their impact was negligible, producing nearly normal distribution of DoD_{fin} since the absolute variability of the efficiency coefficients were small. Therefore, the skewness coefficients $\tilde{\mu}_3$ were positive but lower than 0.1, a criterion of the skewness in this study.

$$DoD_{fin} \propto \frac{1}{E_{bat}} \propto \frac{1}{SE_{bat}} \tag{4.5}$$

The numerical data are tabulated in Table 4.9. Based on the sensitivity indices sensitivity ranks were obtained. The electric propulsion components-related parameters were in high rank, and rotor-related parameters were in low rank. The tw_{rotor} had the lowest impact, which corresponds well with the results in Ref. [91] where rotor pitch has the lowest impact on the flight time of a small unmanned aerial vehicle.

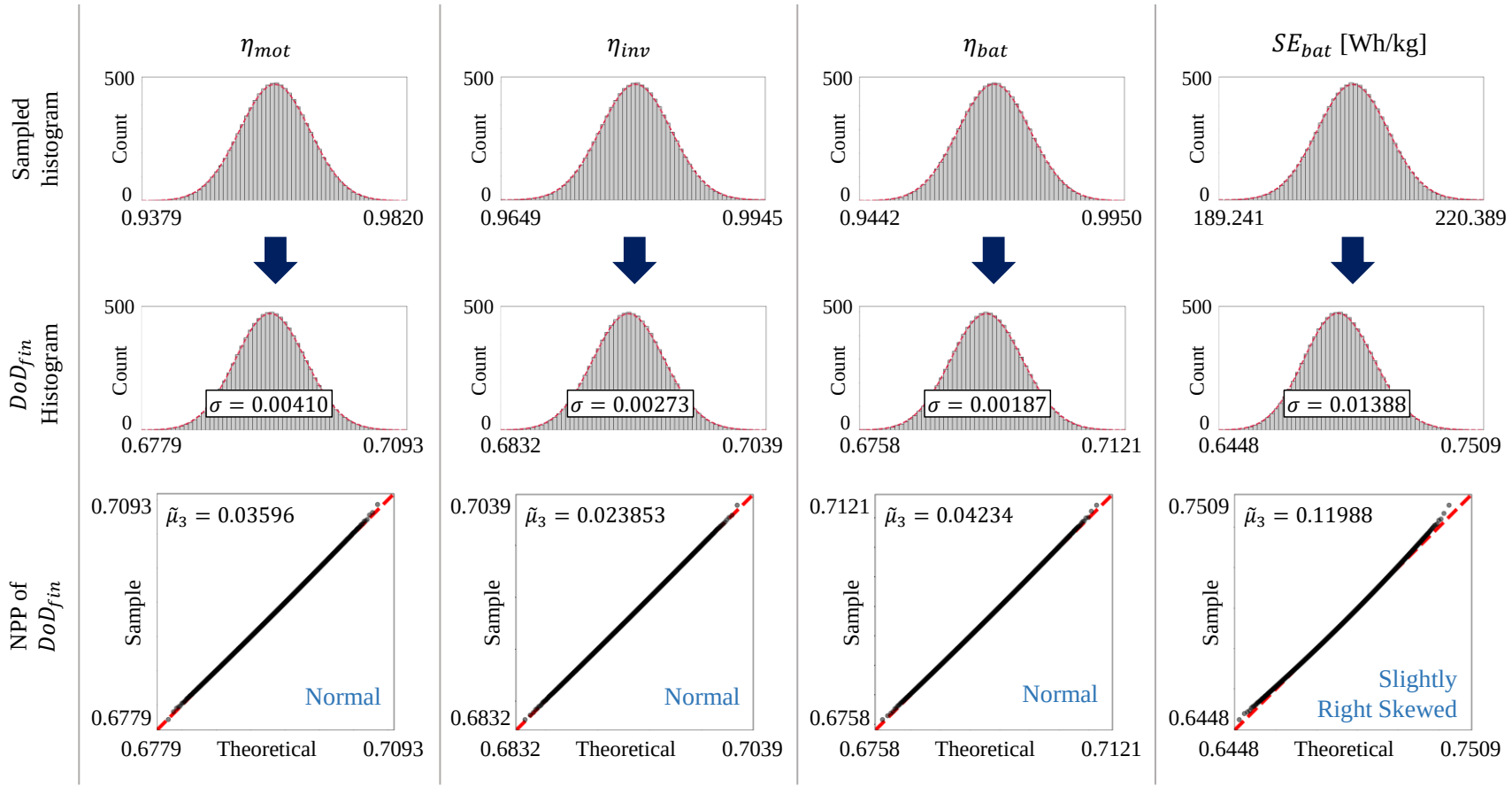

Fig. 4.30. Sensitivity study result of DoD_{fin} by electric propulsion parameters

Table 4.9. Sensitivity study result of DoD_{fin}

Uncertain parameter, x_i	R_{rotor}	c_{rotor}	Ω_{rotor}	tw_{rotor}	η_{mot}	η_{inv}	η_{bat}	SE_{bat}
COV of sampled x_i	0.1	0.2	2.0	0.5	0.6	0.4	0.7	2.0
$\mu_{DoD_{fin}}$ (mean)	0.69321	0.69321	0.69333	0.69321	0.69323	0.69322	0.69324	0.69348
$\sigma_{DoD_{fin}}$ (std. dev.)	0.00053	0.00007	0.00187	0.00003	0.00410	0.00273	0.00485	0.01388
$\tilde{\mu}_{3_{DoD_{fin}}}$ (skewness)	0.01783	0.00832	0.40918	0.08033	0.03596	0.02385	0.04234	0.11988
Median of DoD_{fin}	0.69321	0.69321	0.69321	0.69321	0.69321	0.69321	0.69321	0.69321
COV of DoD_{fin}	0.07618	0.01099	0.26925	0.00511	0.59162	0.39436	0.69958	2.00096
$SI_{x_i,DoD_{fin}}$	0.76244	0.05501	0.13473	0.01023	0.98675	0.98669	1.00015	1.00120
Sensitivity rank	5	7	6	8	3	4	2	1

A similar analysis was conducted for one of the other output results $OASPL_{max}$. Since the $OASPL_{max}$ was affected only by the rotor-related parameters, four histograms and NPPs were obtained. The graphical results and numerical results are presented in Fig. 4.31 and Table 4.10, respectively. As can be seen in Fig. 4.31, when Ω_{rotor} had the normal distribution, the distribution of $OASPL_{max}$ had slight left skewness, showing a concave downward curve in NPP and a negative skewness coefficient. This is the non-linear correlation by the logarithm function in Eq. (2.57). The distribution of the logarithm of a normal distribution has slightly left skewness in naturally.

The variance of $OASPL_{max}$ had the biggest value in Ω_{rotor} case because the absolute variation in the distributions of the geometric parameters (R_{rotor}, c_{rotor}, and tw_{rotor}) were small. The sensitivity indices based on $OASPL_{max}$, $SI_{x_i,OASPL_{max}}$, had the same ranks with the sequence of the variance. The influential parameters were in the sequence of Ω_{rotor}, R_{rotor}, c_{rotor}, and tw_{rotor}. The result that Ω_{rotor} and R_{rotor} are the two most influential parameters corresponded well with the result in Ref. [120].

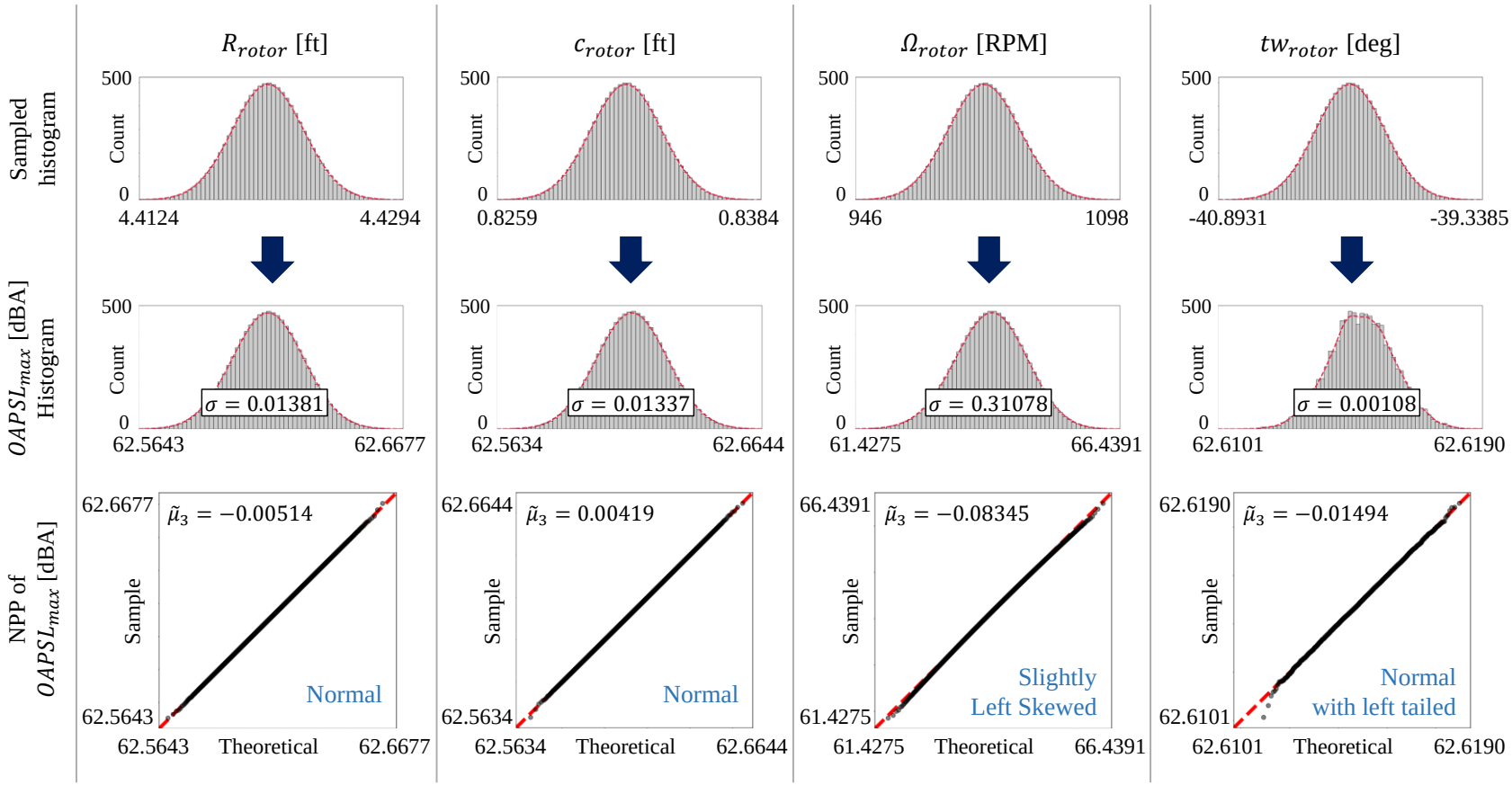

Fig. 4.31. Sensitivity study of $OASPL_{max}$ by rotor parameters

Table 4.10. Sensitivity study result of $OASPL_{max}$

Uncertain parameter, x_i	R_{rotor}	c_{rotor}	Ω_{rotor}	tw_{rotor}
COV of sampled x_i	0.1	0.2	2.0	0.5
$\mu_{OASPL_{max}}$ (mean)	62.61493	62.61495	62.61056	62.61494
$\sigma_{OASPL_{max}}$ (std. dev.)	0.013808	0.013376	0.310781	0.00108
$\tilde{\mu}_{3_{OASPL_{max}}}$ (skewness)	-0.00514	0.004186	-0.08345	-0.01494
Median of $OASPL_{max}$	62.61494	62.61494	62.61494	62.61494
COV of $OASPL_{max}$	0.022052	0.021362	0.496371	0.001725
$SI_{x_i,OASPL_{max}}$	0.220699	0.106892	0.248380	0.00345
Sensitivity rank	2	3	1	4

4.2.5. Hover Performance Analysis

In order to investigate the mixed parametric uncertainty effect on the performance output indices, MCS was conducted for 10-minute hover flight with the eight parametric uncertainties as before. The flight condition was assigned as in Table 4.11. As mentioned earlier, the battery weight was settled as a constant to simulate battery energy capacity variation depending on the variation of the specific energy of the battery. With given gross weight, battery weight, and flight time, the final depth of discharge DoD_{fin} was obtained after 10-minute hover flight.

Table 4.11. Hover flight condition

Hover altitude	Gross weight	Battery weight	Flight time
656.2 ft	4965.914 lb	1596.660 lb	10 min.
200 m	2252.50 kg	724.233 kg	

Aleatory uncertainty (parametric uncertainty)

Under the designated hover flight condition, statistical moments and distributions were obtained by MCS. The outcome quantities of interest were 9 performance quantities in total: rotor power P_{rotor}, noise index $OASPL_{max}$, figure of merit FM, motor power P_{mot}, inverter power P_{inv}, battery power P_{bat}, battery discharge C-rate χ, overall system efficiency η_{sys}, and final depth of discharge DoD_{fin}. For the nine quantities of interest, histograms, empirical PDF curves, and CDF curves are overlaid together in Fig. 4.32, and numerical data including statistical moments are presented in Table 4.12. The empirical PDF curves drawn with a red dashed line were

obtained by kernel density estimator with Gaussian basis function [111] (Eq. (3.10)). The CDF curves were plotted with a solid blue line, and short black tips indicated the 95% confidence interval of the distribution. The yellow glowing dotted line showed the nominal values that were obtained by deterministic analysis, which was nearly same with, but clearly different to the mean values. The deviation between the interval boundaries and the nominal value was presented in percentage units.

The first row in Fig. 4.32 shows the output quantities that were influenced only by the rotor-related parameters. The second row is for the power-related output quantities that were influenced by the efficiency coefficients. The output quantities that are positioned in the last row are kinds of the final outcomes after considering all effects of the uncertainty parameters. This downward stratification implies the calculation direction in the conceptual design tool.

Analysis of variance (ANOVA) results for each outcome quantity were presented using sunburst chart where the most influential input parameter and its impact was given. Blue-based colors are for the rotor-related input parameters, and green-based colors are for electric-components-related input parameters. As can be expected by the sensitivity results, the electric-component-related parameters have emerged to be influential as the calculation has proceeded. The most influential parameter in rotor-related outcome quantities was Ω_{rotor} and its impact was overwhelming the other variables. After applying the efficiency coefficient for the electric power in motor and inverter, η_{mot} had the most significant impact. When the battery-related outcome quantities (P_{bat}, χ, DoD_{fin}, and η_{sys}) were analyzed, η_{bat} and SE_{bat}

were the influential factors on them. SE_{bat} had over the half of proportion in the quantified impact especially when the battery energy was used to calculate χ_{bat} and DoD_{fin}; recall the Eqs. (2.25) and (2.26)).

From the magnitude of the deviations between the nominal values and the 95% confidence intervals, three major characteristics or phenomena could be drawn; skewness, dilution effect, and forward propagation of uncertainties.

The first feature was a skewness relationship in which the inequality of the deviations toward both ends implies that there was a skewness in the distribution. The skewness of the distribution was getting bigger as the magnitude of inequality increased. The distributions in the first row, for P_{rotor}, $OASPL_{max}$, and FM, were taken as an example. In the distribution of P_{rotor}, the deviation between the nominal value and interval ends had a difference of 0.14% point and the value in the right-hand side was bigger. These characteristics indicated that the distribution of P_{rotor} had right skewness. On the other hand, the distribution of FM showed the opposite situation where the difference in the two values of deviation was equal to 0.14% point, but the left-hand side value was bigger. Therefore, the distribution of FM had a left skewness. In the distribution of $OASPL_{max}$ the magnitude of the difference became smaller to 0.05% point, so that the skewness was mitigated. However, the sign of the skewness coefficient was not exactly matched due to small value of the skewness. It can be concluded that the skewness coefficient under 0.1 was not that meaningful. These results could be confirmed numerically in Table 4.12 where the skewness coefficients of the distributions are presented.

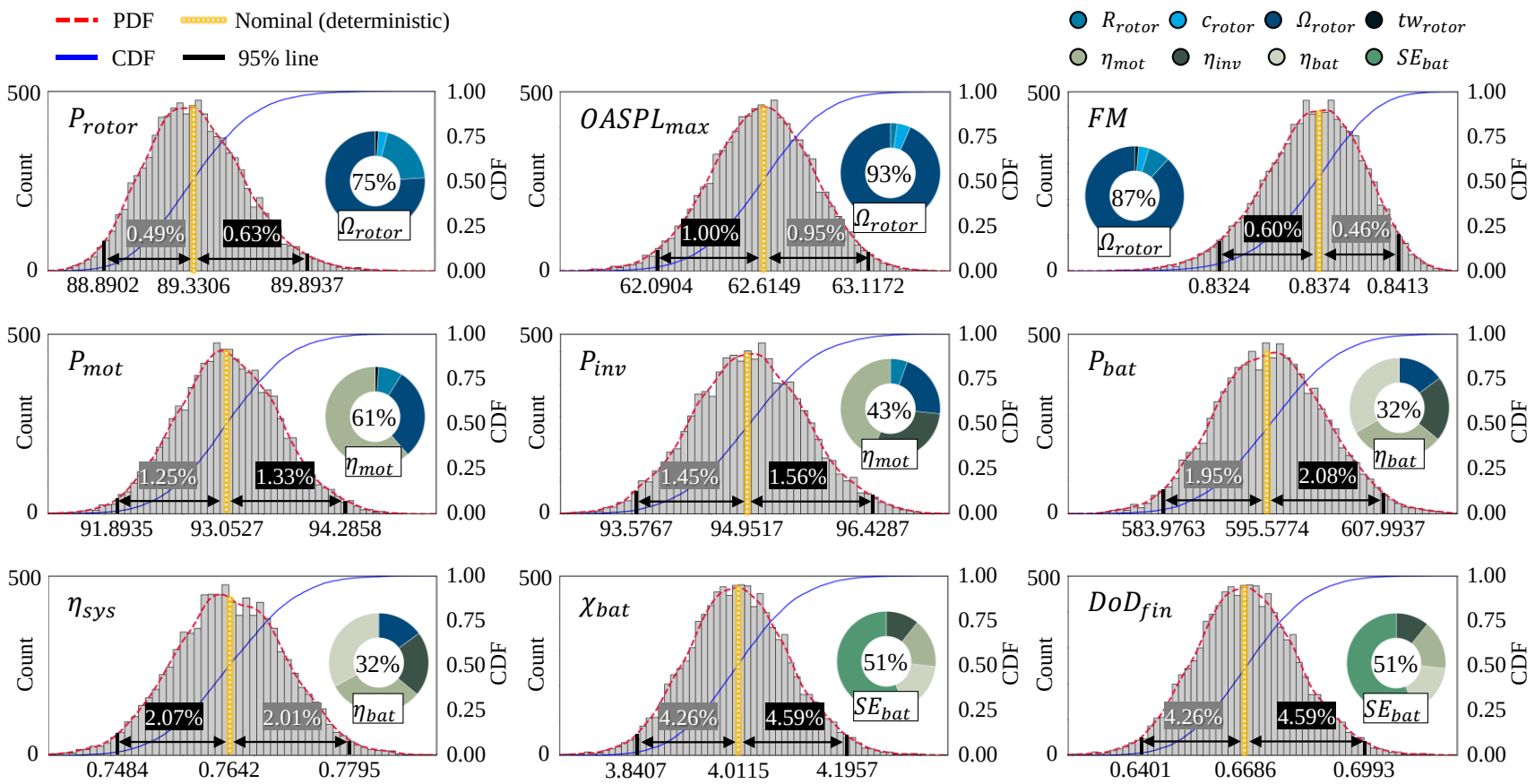

Fig. 4.32. Distribution of performance indices with the parametric uncertainty in 10 minutes hover flight

Table 4.12. Statistical values of the performance indices in 10 minutes hover flight

Output	Nominal value (deterministic)	μ	COV [%]	$\tilde{\mu}_3$	95% interval	Top 4 influential parameters			
						1st	2nd	3rd	4th
P_{rotor} [kW]	89.33056	89.34765	0.28313	0.37212	[88.8902, 89.8937]	Ω_{rotor}	R_{rotor}	c_{rotor}	tw_{rotor}
						74.85%	19.62%	2.88%	1.07%
$OASPL_{max}$ [dBA]	62.61494	62.61056	0.49741	-0.08793	[62.0904, 63.1172]	Ω_{rotor}	R_{rotor}	c_{rotor}	tw_{rotor}
						93.40%	4.35%	2.22%	1.24%
FM	0.83740	0.83725	0.27417	-0.39520	[0.8324, 0.8413]	Ω_{rotor}	R_{rotor}	c_{rotor}	tw_{rotor}
						86.60%	6.98%	3.35%	1.24%
P_{mot} [kW]	93.05266	93.07377	0.66537	0.04059	[91.8935, 94.2858]	η_{mot}	Ω_{rotor}	R_{rotor}	c_{rotor}
						60.74%	29.40%	7.71%	1.13%
P_{inv} [kW]	94.95170	94.97472	0.77382	0.04729	[93.5767, 96.4287]	η_{mot}	η_{inv}	Ω_{rotor}	R_{rotor}
						42.99%	29.23%	20.81%	5.46%

Continued to next page

P_{bat} [kW]	595.57738	595.74906	1.03706	0.04979	[583.9763, 607.9937]	η_{bat}	η_{mot}	η_{inv}	Ω_{rotor}
						31.66%	29.38%	19.97%	14.22%
χ_{bat} [1/hour]	4.01150	4.01426	2.24946	0.10167	[3.8407, 4.1957]	SE_{bat}	η_{bat}	η_{mot}	η_{inv}
						50.93%	15.55%	14.42%	9.81%
η_{sys}	0.764192	0.76405	1.04253	0.01559	[0.7484, 0.7795]	η_{bat}	η_{mot}	η_{inv}	Ω_{rotor}
						32.23%	30.31%	20.62%	14.60%
DoD_{fin}	0.66858	0.66904	2.24946	0.10167	[0.6401, 0.6993]	SE_{bat}	η_{bat}	η_{mot}	η_{inv}
						50.93%	15.55%	14.42%	9.81%

The second feature was the effect of overlapped uncertainties on the output quantities, referred to as a dilution effect here and in Ref. [91], which means the skewness of the output quantities is decreasing as the uncertainty propagates. In order to graphically check the skewness of the outcomes' distributions multiple NPPs are plotted in Fig. 4.33. The P_{rotor} and FM have remarkable skewness in their distribution. This skewness is induced from the uncertainties in the rotor geometry and rotational speed. When the rotor thrust T_{rotor} is fixed, the P_{rotor} has proportional relationship with rotor geometric parameters shown in Eq. (4.6). The equation in the right parenthesis have a natural right skewness when each parameter is normally distributed. As FM is proportional to a reciprocal of P_{rotor} (Eq. (2.17)), it has naturally left skewness in its distribution.

$$P_{rotor} = \rho_{air} \cdot A \cdot V_{tip}^3 \cdot C_P \propto \left(\frac{1}{R} + c \cdot R^4 \cdot \Omega_{rotor}^3\right) \tag{4.6}$$

As mentioned earlier at the sensitivity study in Section 4.2.4, the distribution of power in the electric components P_{mot}, P_{inv}, and P_{bat} should follow the distribution of P_{rotor} with the first order linear correlation. Nevertheless, the skewness originated from the distribution of P_{rotor} was diluted a lot and the skewness were not be recognized in the P_{mot}, P_{inv}, and P_{bat} distribution. Their NPPs show well aligned scatter plots at the diagonal line. This is because the normal distribution of the efficiency coefficient η_{mot}, η_{inv}, and η_{bat} had larger effect on the each-related power indices, mitigating the skewness from the P_{rotor}. As shown

in ANOVA analysis, the electric efficiency coefficients emerged on the top ranks and their normal distribution diluted the impact of the rotor parameters.

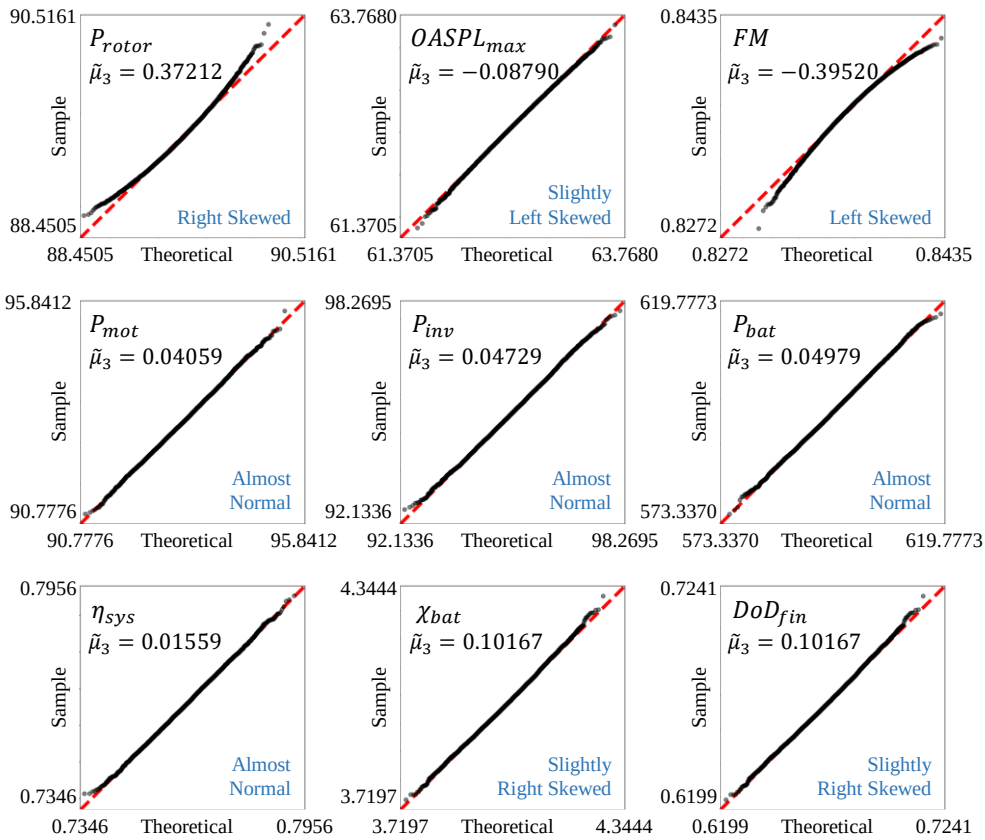

Fig. 4.33. NPP of output quantities of interest

The last feature that could be observed was a forward propagation of the uncertainties. In Fig. 4.32, the magnitude of deviation was getting bigger as the calculation of the outcome quantities proceeded. This trend also can be confirmed the increase of COV in Table 4.12, which is graphically presented in Fig. 4.34. The x-axis of Fig. 4.34 is sequenced according to the calculation process, and the y-axis was the COV in percentage units. As can be seen, the COV of the outcome quantities

kept increasing when the uncertainty in each calculation step was infused, and the magnitude of the increment was nearly proportional to the magnitude of the COV of the infused uncertainties. Since χ times by flight time, herein fixed 10 minutes, is equal to DoD_{fin}, the COV, skewness, and the result of ANOVA were identical to each other.

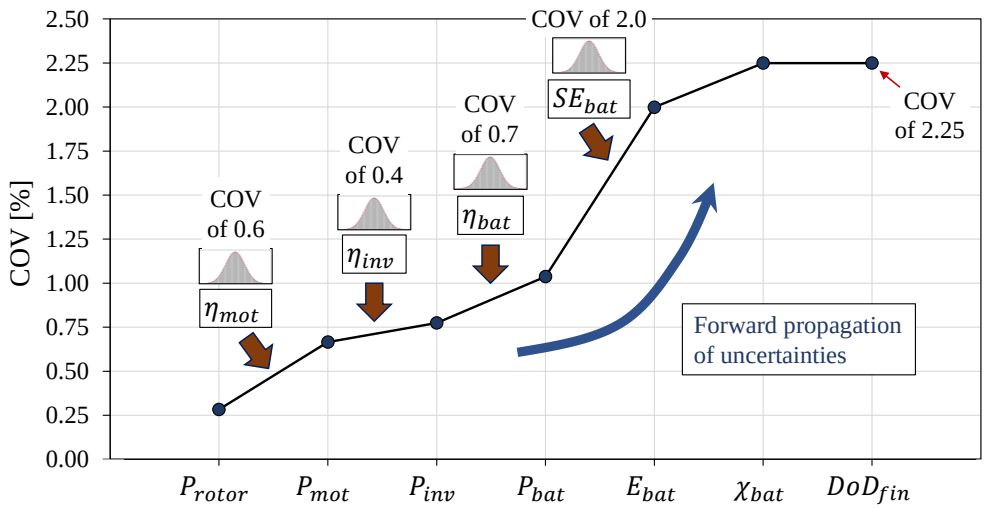

Fig. 4.34. COV variation by forward propagation of uncertainties

With epistemic uncertainty (model uncertainty)

As an imperative milestone before conducting uncertainty quantification in a mission profile, the model uncertainty parameter defined in Section 3.3.2 was used to analyze the effect of the simplified model. Since the performance indices were calculated in the hover flight condition, the model uncertainty parameter for rotor power, $\theta_{pw,BEMT}$, was only used among the three model uncertainty parameters.

Resultant probability boxes (p-box) for the nine performance parameters were generated as shown in Fig. 4.35. In the figure, there are three CDF curves and boundary edges. The boundary edges were obtained using the interval of the $\theta_{pw,BEMT}$ for the best and worst situations. The blue line is the CDF curve when the only parametric uncertainties was considered with the expectation of $\theta_{pw,BEMT}$. This blue line was equal to CDF curve in Fig. 4.32. As can be seen, except for $OASPL_{max}$, the p-box was generated according to $\theta_{pw,BEMT}$ since $\theta_{pw,BEMT}$ corrected the calculated rotor power P_{rotor} and the effect of $\theta_{pw,BEMT}$ was propagated sequentially. The difference between the blue CDF curve and boundary with respect to median values of the three curves was presented in percentage units. The magnitude of difference to the both sides was not equal to each other since there was a shift in the interval of $\theta_{pw,BEMT}$ in Fig. 3.8. Meanwhile, the magnitudes of difference in the outcome quantities were almost same since the only one model uncertainty parameter, herein $\theta_{pw,BEMT}$, was used in the hover flight condition.

As described earlier in Section 3.1.4, CDF curves can lie anywhere in the p-box unless crossing the boundaries that were obtained by the end values of the interval

of $\theta_{pw,BEMT}$. In order to demonstrate the effect of the hasty application of distribution to the model uncertainty parameter, two cases with different distribution of $\theta_{pw,BEMT}$ were added in Fig. 4.35: normal distribution of $\theta_{pw,BEMT}$, and uniform distribution of $\theta_{pw,BEMT}$. Each distribution was constructed using the numbers in Table 3.2. The standard deviation of the normal distribution was set to able to enclose the interval of $\theta_{pw,BEMT}$ with 99% confidence. It was decided that the boundary values required for uniform distribution were the same as the end value of $\theta_{pw,BEMT}$ interval.

In Fig. 4.35, the black dashed CDF curve was obtained with the normal distribution for $\theta_{pw,BEMT}$, and the red dash-dotted CDF curve was obtained with the uniform distribution for $\theta_{pw,BEMT}$. Depending on the type of distribution the resultant CDFs had different shape although they were in the p-box area. These results underpin that an unthoughtful assumption and hasty application of distribution for the model uncertainty could lead to inaccurate predictions of the outcome quantities of interest.

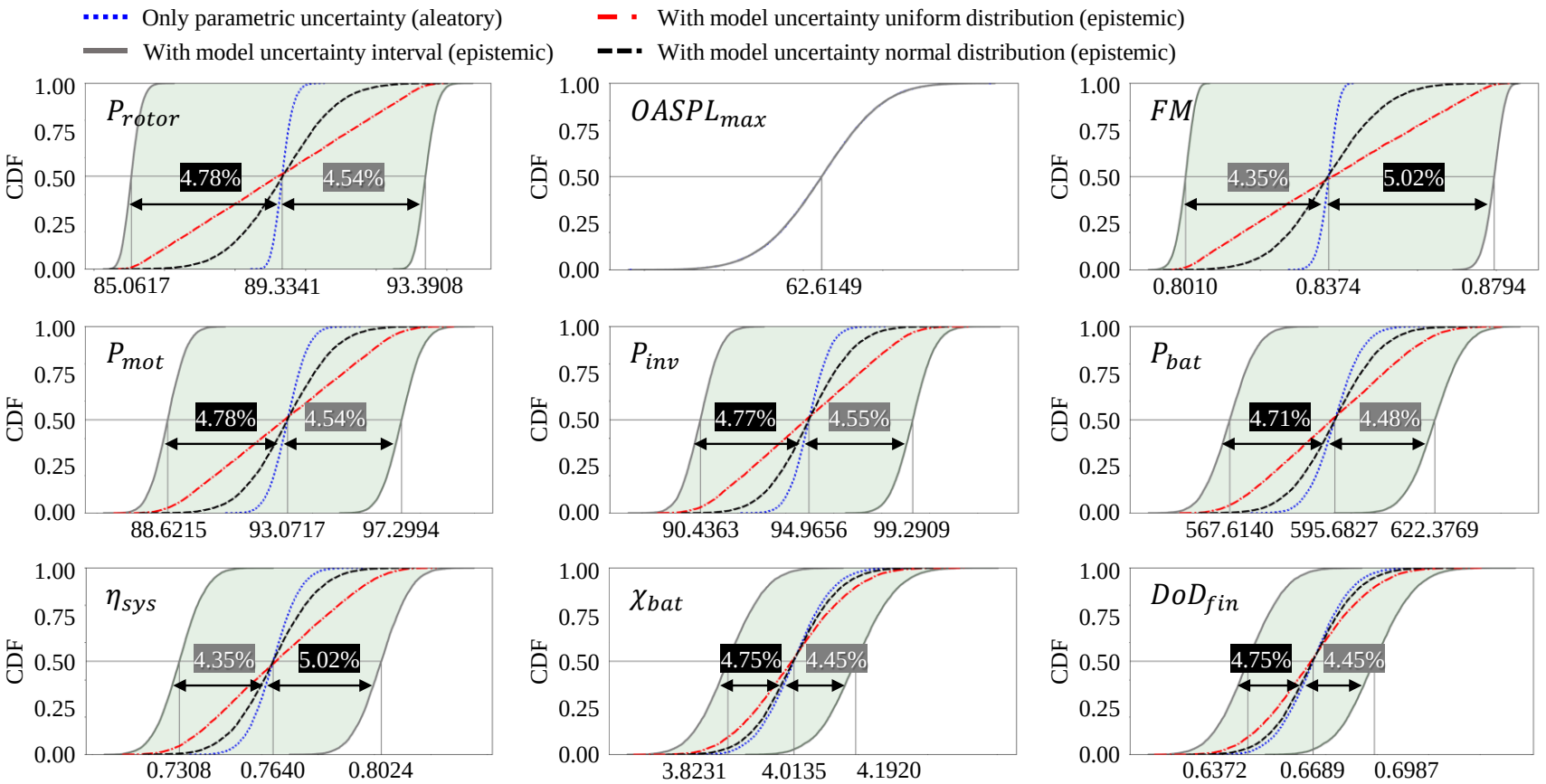

Fig. 4.35. Probability box of performance indices with the parametric and model uncertainty in 10 minutes hover flight

4.2.6. Sizing for Mission Flight

Lastly, the sizing of eVTOL for a generic transportation mission was conducted under an uncertain sizing environment using RISPECT+. The transportation mission consisted of eleven segments as shown in Fig. 4.36 where specific numbers such as flight speed, altitude, and flight distance in each segment are provided. The reference vehicle aviates out 100 km on an altitude of 500 m with a passenger payload of 500 kg. The total flight time was approximately 28 minutes and it was assumed that there was no external wind disturbance during the flight. The maximum DoD_{fin} was set to be 0.8, which meant 80% of nominal energy could be used. The uncertain input parameters and the specification of the reference vehicle were the same as in the hovering case adding the wing incidence angle $\alpha_{w_{inc}}$, specific power of motor, SP_{mot}, and inverter, SP_{inv}, which are shown in Table 4.13. The all variables were assumed again to be follow Gaussian distribution. The three model uncertainty parameters, $\theta_{pw,BEMT}$, $\theta_{pw,BET}$, and $\theta_{C_{L_{\alpha_{wing}}}}$ were settled as the biggest values to obtain the most conservative design result with simplicity.

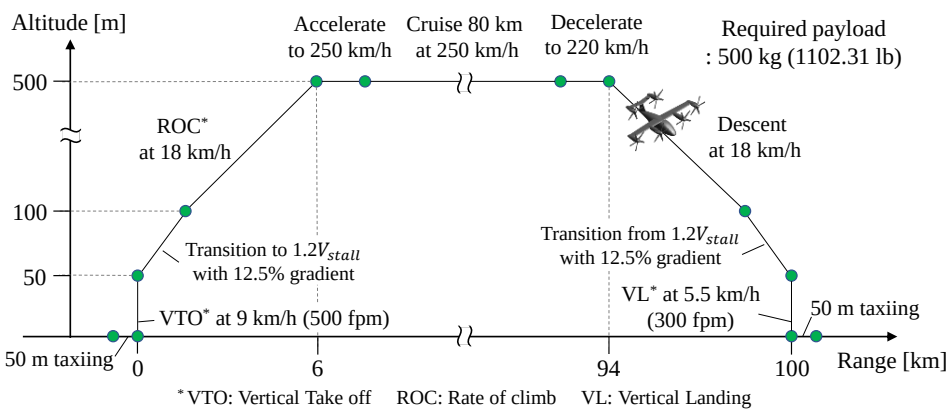

Fig. 4.36. Transportation mission profile

Table 4.13. Parametric uncertainty of the base eVTOL in mission flight

Component	Variable		Distribution type	Nominal value	COV [%]
Rotor	R_{rotor}	[ft]	Gaussian	4.421	0.1
	c_{rotor}	[ft]	Gaussian	0.8320	0.2
	Ω_{rotor}	[RPM]	Gaussian	1020	2.0
	tw_{rotor}	[deg]	Gaussian	-40.112	0.5
Wing	$\alpha_{w_{inc}}$	[deg]	Gaussian	2.68	2.0
Electric Propulsion	η_{mot}	·	Gaussian	0.96	0.6
	η_{inv}	·	Gaussian	0.98	0.4
	η_{bat}	·	Gaussian	0.97	0.7
	SP_{mot}	[kW/kg]	Gaussian	4.932	2.0
	SP_{inv}	[kW/kg]	Gaussian	13.00	2.0
	SE_{bat}	[Wh/kg]	Gaussian	205.0	2.0

Under the given uncertain geometry parameters, the iterative sizing process was conducted until the available payload became equal to required payload weight following RISPECT+ sizing process (Fig. 2.8) through MCS. The flight performance variation under the uncertainty is displayed in Fig. 4.37 where the required power at the battery and the required energy with respect to the mission segments are presented with 95% interval. The line plot is for the required power in kilowatt units. The dashed line shows the averaged value of the required power and the shaded area indicates the 95% interval that is approximately equal to 2-sigma area. The

maximum power was obtained in the vertical flight: vertical take-off and vertical landing. From the transition-out segment to the transition-in segment, the eVTOL flight in the wing-borne configuration that required less power during flight. The distributions of rotor power and battery power for the three segments (vertical take-off, cruise, and vertical landing) were added in the top of the figure with their NPP figures. In the fully vertical flights, the distribution of the required powers had right skewness, which corresponded with the results from hover flight in Section 4.2.5 due to the distribution of Ω_{rotor}. Meanwhile, the magnitude of skewness was almost twice as large as that in hover flight. This was because of the fact that required thrust, proportional to the sized gross weight, varied according to the input variables, which was a different situation to the hover case where the gross weight was fixed at a certain value. The skewness was mitigated in the cruise segment since the parasite power during the cruise segment was nearly constant due to a fixed equivalent flat plate area of the aircraft. The magnitude of variation presented with COV also underpinned those results.

Bar plot in Fig. 4.37 shows the required energy in kilowatt-hour units with respect to the mission segment, which was obtained by multiplying the required power and segment time. The error bar indicates the 95% interval, which is approximately equal to 2-sigma area. During 28-minutes flight, the cruise segment occupied approximately 67.8% of flight time, 19 minutes, so that the required energy in the cruise segment was incomparable to the other segments although the required power in the cruise segment was not that demanding. In the same line, the required energy

in the vertical landing was bigger than that of the vertical take-off due to the longer segment time. The magnitude of COVs of the required energy in the vertical take-off and cruise segments was both bigger than those of the required power due to uncertainty in the variance of the efficiency coefficients of the electric propulsion components. The distribution plots of the required energy were omitted because their shapes were identical to those of the required power distribution. Table 4.14 shows the numerical results with the mean values and 95% intervals.

Table 4.14. Required power and energy during the mission

Segment	Req. battery power [kW]		Req. energy [kWh]	
	mean	95% interval	mean	95% interval
Taxiing in	9.294	[9.096, 8.507]	0.044	[0.043, 0.044]
VTO	551.962	[511.842, 604.734]	6.224	[5.778, 6.810]
Transition out	271.166	[251.269, 297.362]	4.658	[4.325, 5.096]
Climb	264.371	[247.863, 286.265]	6.058	[5.690, 6.545]
Acceleration	169.951	[161.453, 180.033]	2.971	[2.828, 3.140]
Cruise	183.895	[175.158, 194.078]	60.339	[57.622, 63.488]
Deceleration	169.951	[161.453, 180.033]	2.971	[2.828, 3.140]
Descent	68.574	[62.419, 77.607]	2.901	[2.668, 3.245]
Transition in	249.170	[230.325, 273.917]	4.291	[3.977, 4.705]
VL	523.552	[485.079, 574.251]	9.668	[8.966, 10.590]
Taxiing in	9.294	[9.096, 9.499]	0.044	[0.043, 0.044]

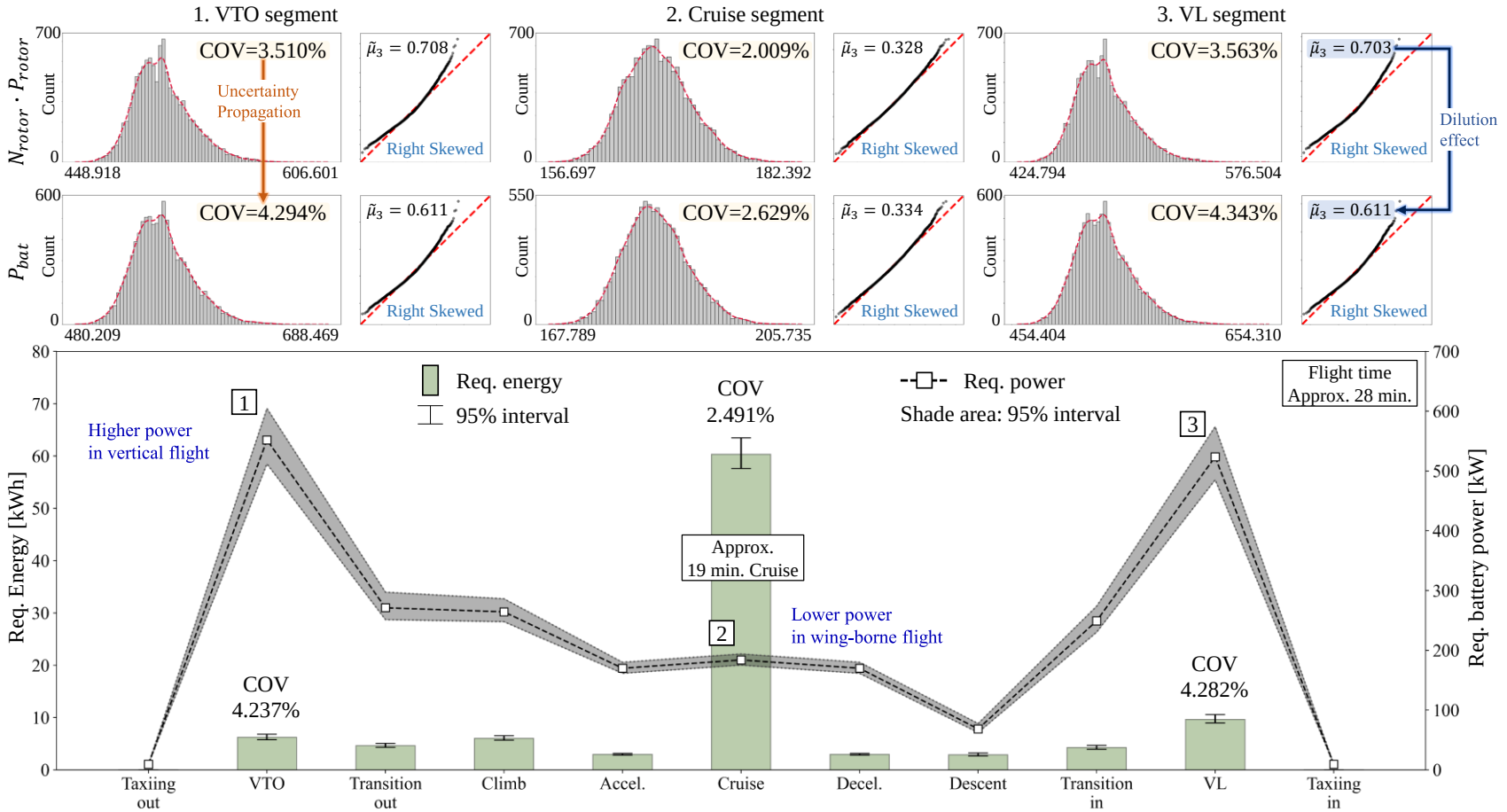

Fig. 4.37. Required power and energy during the mission

The weight breakdown and some of the weight histograms are shown in Fig. 4.38. The left bar plot in Fig. 4.38 shows the weight information of each component with each fraction in empty weight and the right histograms show distributions of some components. The nominal values are for the averaged value of MCS samples and error bars show 95% interval. The weight axis is presented by both imperial unit system and SI unit system. The mean gross weight was 4994.88 lb (2265.64 kg) and its COV was calculated as 2.438. The payload weight was almost fixed to 1102.31 lb (500 kg) since the sizing process was conducted iteratively by changing the gross weight until the available payload was equal to the given target payload, herein 1102.31 lb. Hence, there was little variance in the payload given convergence error was ignored. The histogram of gross weight had a little freaky shape showing highly frequent data samples in a certain area. This situation was related to the sizing process of RISPECT+. As described in Section 2.2.1, the sizing process was initiated with an assumption of gross weight for calculating component weights that were functions of gross weight. Thus, the sizing process would be terminated immediately if the initial value was appropriate by chance. Since the converged payload was almost same with the given target value, the distribution of empty weight also had similar shape.

The major components that composed the empty weight were classified by structure group, electric propulsion group, and system group. The blue series color bars are for the structure group: fuselage, rotor, and wing system. They accounted for from 33.80% to 38.10% of empty weight.

The green series color bars are for the electric propulsion group: battery, motors, inverters, and TMS with wiring. The battery is the single heaviest component in the eVTOL of which weight fraction accounted for 32.67~36.36% of the empty weight alone. The distribution of the battery weight shows a right skewness induced from the right-skewed distribution of the required power and energy. The distributions of electric motors and TMS with wiring have similar aspects to that of battery. Note that the COV of TMS with wiring weight became much bigger than any other components' weight. That was because TMS and wiring were sized based on a summation of parameters induced from every electric component. TMS was sized using a summation of power losses from the battery, motors, and inverters (Eq. (2.32)), which implies that the summed power losses got effect from all three components' power distributions. A similar situation was observed in the wiring weight that was proportional to the entire weight of the electric propulsion system (Eq. (2.45)). That was why the COV of TMS with wiring weight was much bigger than others.

The system group was for flight control systems and given avionics equipment. Its variance was negligible due to the fact that a custom value was imposed on avionics equipment without variance.

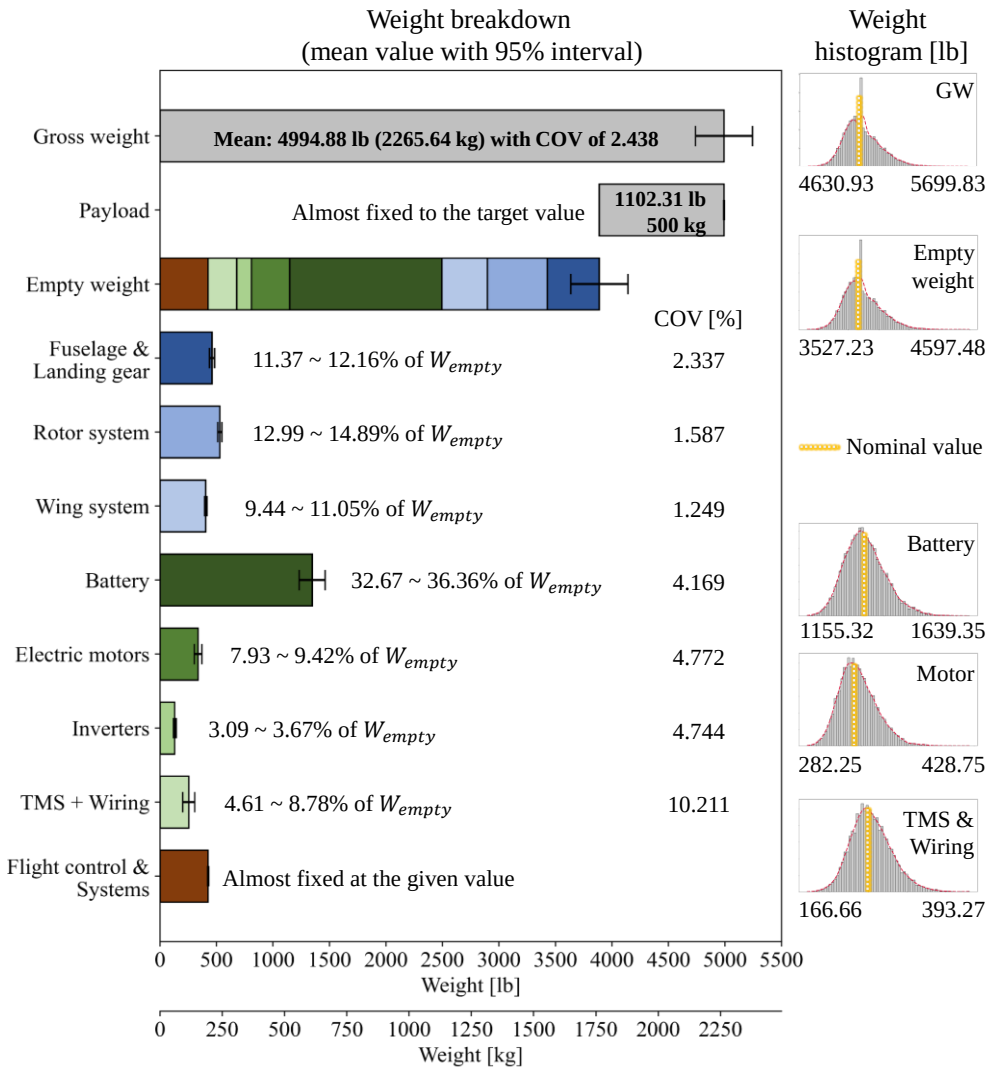

Fig. 4.38. Weight breakdown and histograms of sized eVTOL

When scrutinizing the gross weight distribution of the MCS samples, it can be recognized at a glance that approximately 53% of the samples had heavier gross weight than the nominal value that was obtained by the deterministic way. The heavier gross weight implied that more energy was required to conduct the target mission. In this circumstance, the probability of the mission success under deterministic input condition was lower than half (47%). This value indicated a high risk of eVTOL designed under the deterministic environment.

In order to investigate which combination of the geometric uncertainties brought about the higher gross weight, the histograms of the input geometric uncertainties are shown in Fig. 4.39 with discrete two levels by the weight index that was determined by the gross weight obtained by the deterministic approach. The blue-colored histograms were flagged with a lighter gross weight, which implied sufficiency of mission fulfillment. The orange-colored histograms were flagged with a heavier gross weight, which implied insufficiency of mission fulfillment. The straight lines indicate the mean value of each category. In comparison, there was a shift in the mean lines in the histogram according to the category. From the lighter gross weight to heavier gross weight, the notable changes in the mean values were as follows; larger Ω_{rotor}, smaller η_{bat}, SE_{bat}, η_{mot}, SP_{mot}, η_{inv}, and SP_{inv} induced the heavier gross weight. The shift in the other variables can be neglected. All shifts in the mean values resulted in the higher required power and resultant energy during the mission. The high rotational speed generated higher power and lower efficiency (Figure of merit) in the rotor aerodynamics. The decrease in the

efficiency coefficients was the immediate cause of energy increment, and the decreases in the specific energy of the battery and specific power of the motor and inverter directly induced the increases in electric propulsion components' weight. The magnitude of shift implied the impact of the variables; the battery was the most influential component as it occupied at most 36.36% of empty weight. The electric motors and inverters followed sequentially. From the result, designers recognized and confirmed the significance of the electric propulsion system from the quantified data, so that they should plan by priority to develop electric propulsion components with high robustness showing little variance in the performance for designing a highly reliable eVTOL aircraft.

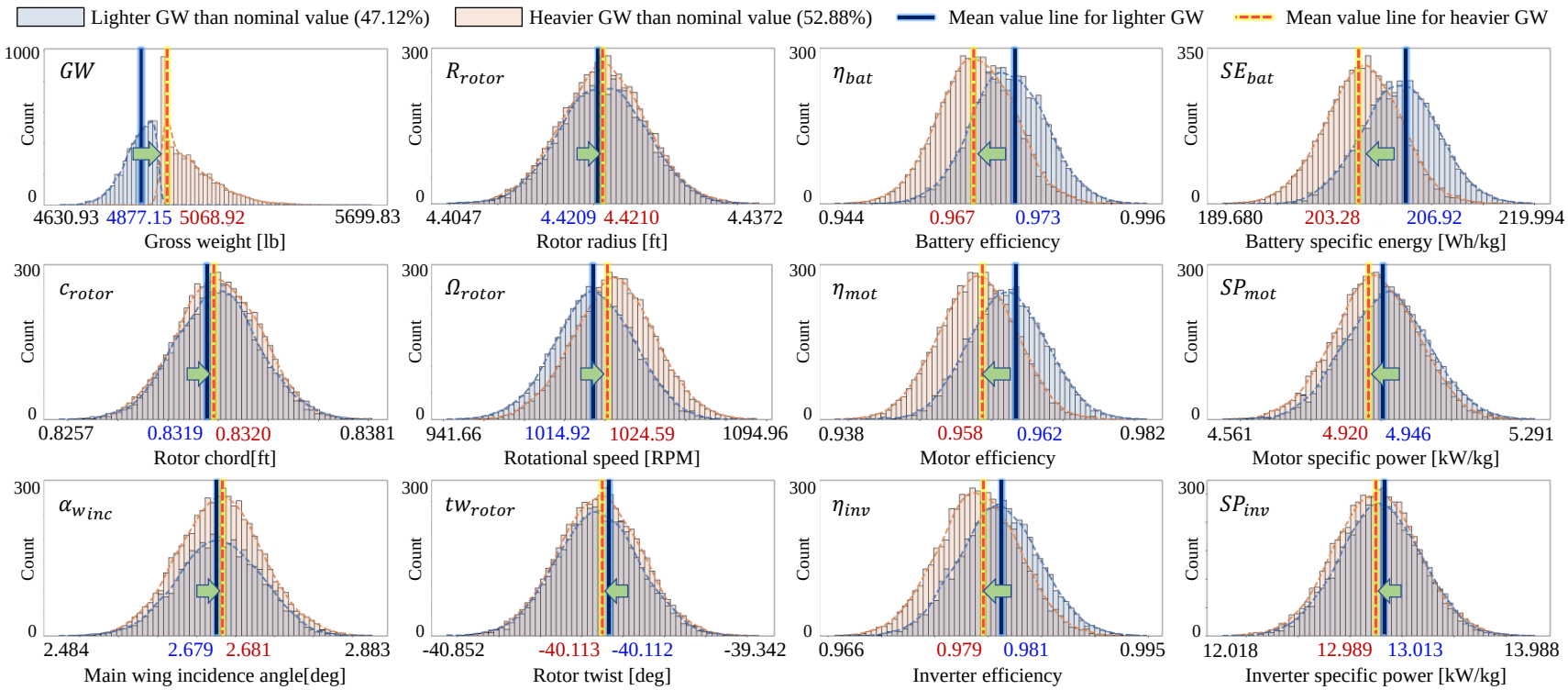

Fig. 4.39. Histogram of parametric uncertainties by gross weight variation

Chapter 5

Conclusion

5.1. Summary

In efforts to derive more practical designs for advanced air mobility, improved design frameworks for the two primary tasks that should be carried out in the conceptual design phase were developed and their validities were demonstrated with the pilot projects in this study. Not only suggested better mathematical formulations were, but also various uncertainties were considered with the use of the combination of the surrogate model, MCS, and LHS method for their propagation.

The most important improvement in the technology portfolio assessment framework was that the calculation method for an amalgamated effect of multiple technologies was based on a multiplicative approach rather than an additive approach. In addition, the interaction factor which was defined from TCIM elements enabled to consider the non-linear relationship and interactional effects between technologies. Both improvements could result in more rational and practical situations in technology infusion.

In terms of uncertainties, epistemic uncertainties from surrogate models that were usually excluded before were incorporated using MLP model with MC dropout. The alternative method of using prediction intervals as confidence intervals of a surrogate model could be used similarly depending on the surrogate model [105]. The inclusion of the epistemic uncertainty provided more information to help decision-

makers to make more reasonable and reliable decisions. It would result in a reduction in the number of design feedbacks, the possibility of development cost increases, and eventually the risk of program failure. In the demonstration project, different desirable technology portfolios were selected based on the consideration of epistemic uncertainty.

In the sizing process, with uncertainties from physical geometric parameters and simplified mathematical analysis modules, the sizing process was expanded, and then uncertainty propagation on flight performance and sizing results was carried out throughout various flight conditions in the conceptual design phase. The uncertainties were identified and classified based on their origins. Variations in the representative geometric parameters were modeled using Gaussian distribution, and model uncertainties in the simplified analysis modules were quantified by comparing analysis results with experimental data or higher fidelity analysis. The quantified uncertainties were considered by adopting model uncertainty parameters.

For the single hovering flight, skewed distributions for performance outcomes were observed as the responses to the normally distributed geometry input, which implied non-linear characteristics in the aircraft system. Another point that drew interest was the dilution effect showing that specific uncertainties overwhelmed other uncertainties, which helped to prioritize the significance of the uncertainties.

For the generic transportation mission, over half of the cases with geometric variations were sized to have a heavier gross weight than that obtained by the deterministic sizing method. The heavier gross weight was induced by higher

required power and energy that are result in heavier electric propulsion component weight. This situation implied that deterministically sized aircraft had a high possibility of mission failure and low reliability of successful transportation in the conceptual design phase. There is a chance that fault design problems can be captured and fixed during the later design phases, but that situation means there will be an increase in cost and a delay in the project schedule. The use of uncertainty-based sizing processes could prevent these consequences from occurring by ensuring that a proper design margin or bumper has been established during the conceptual design phase.

5.2. Originality and Contribution

The ultimate objective and contribution of this dissertation focuses on to derive more realistic, reliable, rational, and reasonable outcomes in the conceptual design phase. The originality and major contributions of this dissertation can be summarized as follows.

- An improved mathematical formulation is developed and presented to realize more plausible and realistic situations where multiple technologies are infused simultaneously. The newly developed formulation is based on the multiplicative approach instead of the previous additive approach. The multiplicative approach makes it able to spontaneously avoid unphysical situations such as zero-mass or negative mass as a result of technology infusion as mentioned in Section 2.1.4.

- Interaction between technologies are simulated by adopting TCIM and an interaction factor. The original TCM was expanded to incorporate additional information of interactions or interference between technologies with the assumptions that only pairwise relationship is considered. The interaction information embedded in TCIM is based on asymmetric relationships between technologies as shown in Section 2.1.3.. Using the elements of TCIM, an interaction factor that is also defined by the multiplicative approach is calculated and used for a net change of system attributes by technologies. The use of TCIM and interaction factor also leads to more realistic and plausible results during technology portfolio assessment.

- "Model uncertainty" from the surrogate models, which has been generally neglected before, is considered and included when evaluating technology infusion results in the surrogate-model-based environment. It was shown that the selected technology portfolios could be different depending on the inclusion of the model uncertainty from the surrogate model (Section 4.1.8). The inclusion of this uncertainty would lead to more reliable and less risky determination for the technology portfolio assessment in the conceptual design phase.

- The developed framework for technology portfolio assessment has the platform-agnostic feature. Though it has been applied to advanced air mobility to demonstrate its methodology and validity, the framework can be applied to a wide range of system or subsystem development projects to decide which technologies to prioritize. In addition to that, eco-systems of future aviation such as operation of advanced air mobility can be subject to the framework if related technologies and their impacts are identified. The framework is also able to help develop roadmaps for future technologies.

- Uncertainty-based sizing framework for advanced air mobility is developed to analyze the uncertainty effect on the performance and sizing results, and to present reliable sizing result in the conceptual design phase for the first time. To this end, a deterministic sizing tool and a cost estimation tool for advanced air mobility were firstly developed by co-working with colleagues, and then they are expanded to the uncertainty-based frameworks. The works done using

this uncertainty-based framework is a kind of prerequisite for the reliability-based design optimization. Presenting the uncertainty-based sizing result could reduce the number of design feedbacks and iterations from the further design phases, which resulting in successful advanced air mobility development program.

- "Model uncertainty" from the simplified analysis models, one of the epistemic uncertainties, is quantified by adopting model uncertainty parameter that is defined as a ratio between a quantity of interest obtained by the used analysis method and that obtained by higher fidelity method. This epistemic uncertainty should be considered especially in the conceptual design phase where most analysis methods used have relatively low fidelity. With the model uncertainty parameters, the confidence interval induced by the used analysis methods can be modeled and presented in the sizing results.

- Model uncertainty parameter, the method used in this dissertation for incorporating uncertainty effects from less reliable analysis methods, is the generalized formulation. They can be applied to a variety of other aircraft sizing and analysis frameworks or analysis tools for disciplines with the same approach.

5.3. Future Work Recommendation

The recommendations for future work for the technology portfolio assessment method and uncertainty-based sizing method presented in this dissertation can be summarized as follows.

An approach to modeling the impact of technology on a system can be improved. The definition of TRL applied in the current study was slightly modified by SAIC [99] from the perspective of the system level since the original definition of TRL was defined at the component technology level. In lieu of this approach, some of the previous studies [15,16] presented other indices for the readiness level such as the integration readiness level, and system readiness level. Adopting these readiness levels may be an effective method for taking a systematic approach, but at the same time, it might complicate the problem. In terms of TRL and the shape of technological uncertainty, the shape function of technology impact is assumed to be a function of the TRL of each technology. If more practical data are obtained from the reality, better assumptions could be developed to lead to more practically meaningful results [10]. Nevertheless, this assumption results in high dependency of the impact factor distribution on the TRL itself, which makes it another uncertainty source to determine which number is appropriate for TRL of a certain technology. Although, in this dissertation, the averaged TRL values obtained from the literature surveys were used in the exemplary application project, handling this aspect could lead to more practical and reasonable results for technology selection.

Second, the timeframe of each technology development speed is assumed that the technology will be sufficiently developed to reach high TRL when production of advanced air mobility starts. However, the development speed of each technology is different from each other in nature. In this dissertation, it was assumed that the parameter for RDT&E cost increase was much larger for low TRL technologies to compensate for the lag in development when compared to high TRL technologies. Developing a more quantitative formulation to address the timeframe issue may be one of the greatest steps toward achieving more meaningful and practical results.

Third, from the perspective of uncertainty-based sizing, it is worth applying the method to more sophisticated and comprehensive analysis modules in order to capture the system response by physical parameter variation in the component level. For example, the implementation of advanced modeling methods for electric motors, inverters, and batteries based on their physical characteristics could result in more abundant materials to help understand the entire system.

As well, reliability-based design optimization by changing the design variables with uncertainties could also be a promising step forward. The direct uncertainty-based sizing process conducted in this dissertation requires substantial computational resources comparable to computational fluid dynamics analysis, from many hours to several days, which makes it difficult to carry out direct design optimization with uncertainties. Instead, for efficient optimization, the surrogate model-based design optimization method can be applied by estimating the mean and standard deviation that are obtained from the sizing with uncertainties.

Finally, the integration of the two processes, namely the assessment of the technology portfolio as well as sizing with uncertainties or optimization, should also be considered. Currently, the two frameworks were not coupled since the computational resource problem. The expected computational time in total is approximately over 50 days under personal desktop environment for constructing a surrogate model; 1000 cases for DOE of surrogate model, 5 seconds of averaged RISPECT+ runtime, and 1000 samples for MCS of each case. There is a possibility that the requirements and proper technology combinations may vary depending on the design variables, the geometry of the vehicle, and the uncertainties in the variables. They might be not independent of one another. The uncertainty effect on performance and weight could also be different depending on the design space and used technologies. To this end, a sophisticated mathematical formulation that connects the two processes is required, but the formulation should be both time- and resource-efficient in order to conduct iterative calculations within the available computational resources. This improvement eventually leads to reliable and practical design results in the conceptual design phase.

References

[1] Hirschberg, M. The Electric VTOL Revolution. Presented at the SA Symposium 2018, San Francisco, California, 2018.

[2] Torenbeek, E. *Advanced Aircraft Design; Conceptual Design, Analysis and Optimization of Subsonic Civil Airplanes*. John Wiley & Sons, Ltd, 2013.

[3] Raymer, D. *Aircraft Design: A Conceptual Approach, Sixth Edition*. American Institute of Aeronautics and Astronautics, Reston, VA, 2018.

[4] Roskam, J. *Airplane Design: Preliminary Sizing of Airplanes*. Design, Analysis and Research Corporation, 1985.

[5] Gudmundsson, S. Chapter 1 - The Aircraft Design Process. In *General Aviation Aircraft Design*, Butterworth-Heinemann, Boston, 2014, pp. 1–32.

[6] McMasters, J., and Cummings, R. Rethinking the Airplane Design Process - An Early 21st Century Perspective. Presented at the 42nd AIAA Aerospace Sciences Meeting and Exhibit, Reno, Nevada, 2004.

[7] Trybula, C. D. C. *"Big Five" Lessons for Today and Tomorrow*. Institute for Defense Analyses, 2012, p. 118.

[8] Mas, F., Arista, R., Oliva, M., Hiebert, B., Gilkerson, I., and Ríos, J. A Review of PLM Impact on US and EU Aerospace Industry. In *Procedia Engineering*, No. 132, 2015.

[9] Padfield, G. *So You Want to Be an Engineer: A Guide to a Wonderful, Mysterious Profession; with Sketches from an Aeronautical Engineer's Album*. Gareth D Padfield, 2015.

[10] Kirby, M. R. *A Methodology for Technology Identification, Evaluation, and Selection in Conceptual and Preliminary Aircraft Design*. Ph.D. Dissertation. Georgia Institute of Technology, 2001.

[11] Akram, F., Prior, M., and Mavris, D. Improved Technology Impact Modeling Through Technology Synergy Matrices. Presented at the 49th AIAA Aerospace Sciences Meeting, Orlando, Florida, 2011.

[12] Gatian, K. N., and Mavris, D. N. Enabling Technology Portfolio Selection through Quantitative Uncertainty Analysis. Presented at the 15th AIAA Aviation Technology, Integration, and Operations Conference, Dallas, Texas, 2015.

[13] Jouannet, C., Amadori, K., and Bäckström, E. Selection of Future Technologies during Aircraft Conceptual Design. Presented at the 55th AIAA Aerospace Sciences Meeting, Grapevine, Texas, 2017.

[14] Amadori, K., Bäckström, E., and Jouannet, C. Future Technologies Prioritization for Aircraft Conceptual Design. Presented at the 2018 AIAA Aerospace Sciences Meeting, Kissimmee, Florida, 2018.

[15] Jouannet, C., Amadori, K., Bäckström, E., and Bianchi, D. Uncertainty Management in Technologies Prioritization for Future Aircraft Program. Presented at the AIAA SciTech 2020 Forum, Orlando, Florida, 2020.

[16] Bianchi, D., Amadori, K., Bäckström, E., Jouannet, C., and Secco, N. An Uncertainty-Based Framework for Technology Portfolio Selection for Future Aircraft Program. Presented at the AIAA SciTech 2021 Forum, VIRTUAL EVENT, 2021.

[17] Huang, Y., Sun, D., and Soban, D. S. “Assessing the Novel Aircraft Lightning Strike Protection Technology Using Technology Impact Forecasting.” *Journal of Aircraft*, Vol. 57, No. 5, 2020, pp. 914–921. https://doi.org/10.2514/1.C035875.

[18] Huang, Y., Soban, D., and Sun, D. “Assessing the Self-Healing Technology Using Novel Technology Impact Forecasting.” *Journal of Aircraft*, Vol. 58, No. 4, 2021, pp. 803–814. https://doi.org/10.2514/1.C036058.

[19] Lee, D., Lim, D., and Yee, K. “Generic Design Methodology for Vertical Takeoff and Landing Aircraft with Hybrid-Electric Propulsion.” *Journal of Aircraft*, Vol. 59, No. 2, 2022, pp. 278–292. https://doi.org/10.2514/1.C036214.

[20] Lee, D., Kang, S., and Yee, K. A Comparison Study of Rotorcraft with Hybrid Electric Propulsion System. Presented at the 45th European Rotorcraft Forum proceedings, Warsaw, Poland, 2019.

[21] Lee, D., and Yee, K. Advanced Analysis Method of Electric Propulsion System for UAM Vehicles. Presented at the 47th European Rotorcraft Forum, VIRTUAL EVENT, 2021.

[22] Cakin, U., Kaçan, Z., Aydogan, Z. A., and Kuvvetli, I. Initial Sizing of Hybrid Electric VTOL Aircraft for Intercity Urban Air Mobility. Presented at the AIAA Aviation 2020 Forum, VIRTUAL EVENT, 2020.

[23] Finger, D. F., Bil, C., and Braun, C. “Initial Sizing Methodology for Hybrid-Electric General Aviation Aircraft.” *Journal of Aircraft*, Vol. 57, No. 2, 2020, pp. 245–255. https://doi.org/10.2514/1.C035428.

[24] Sgueglia, A., Schmollgruber, P., Bartoli, N., Benard, E., Morlier, J., Jasa, J., Martins, J. R. R. A., Hwang, J. T., and Gray, J. S. “Multidisciplinary Design Optimization Framework with Coupled Derivative Computation for Hybrid Aircraft.” *Journal of Aircraft*, Vol. 57, No. 4, 2020, pp. 715–729. https://doi.org/10.2514/1.C035509.

[25] Isikveren, A. T., Pornet, C., Vratny, P. C., and Schmidt, M. “Optimization of Commercial Aircraft Using Battery-Based Voltaic-Joule/Brayton Propulsion.” *Journal of Aircraft*, Vol. 54, No. 1, 2017, pp. 246–261. https://doi.org/10.2514/1.C033885.

[26] de Vries, R., Brown, M. T., and Vos, R. A Preliminary Sizing Method for Hybrid-Electric Aircraft Including Aero-Propulsive Interaction Effects. Presented at the 2018 Aviation Technology, Integration, and Operations Conference, Atlanta, Georgia, 2018.

[27] Khurana, M. S., Russell, C. R., and Scott, R. Uncertainty Quantification of a Rotorcraft Conceptual Sizing Toolsuite. Presented at the AIAA Scitech 2019 Forum, San Diego, California, 2019.

[28] Hartmann, J., Strack, M., and Nagel, B. Conceptual Assessment of Different Hybrid Electric Air Vehicle Options for a Commuter with 19 Passengers. Presented at the 2018 AIAA Aerospace Sciences Meeting, Kissimmee, Florida, 2018.

[29] Voskuijl, M., van Bogaert, J., and Rao, A. G. "Analysis and Design of Hybrid Electric Regional Turboprop Aircraft." *CEAS Aeronautical Journal*, Vol. 9, No. 1, 2018, pp. 15–25. https://doi.org/10.1007/s13272-017-0272-1.

[30] Pornet, C., Gologan, C., Vratny, P. C., Seitz, A., Schmitz, O., Isikveren, A. T., and Hornung, M. "Methodology for Sizing and Performance Assessment of Hybrid Energy Aircraft." *Journal of Aircraft*, Vol. 52, No. 1, 2015, pp. 341–352. https://doi.org/10.2514/1.C032716.

[31] Wang, Y., Pang, Y., Chen, O., Iyer, H. N., Dutta, P., Menon, P. K., and Liu, Y. "Uncertainty Quantification and Reduction in Aircraft Trajectory Prediction Using Bayesian-Entropy Information Fusion." *Reliability Engineering & System Safety*, Vol. 212, 2021, p. 107650. https://doi.org/10.1016/j.ress.2021.107650.

[32] Jung, Y. S., and Baeder, J. Uncertainty Quantification for Laminar-Turbulent Transition on Airfoil and Fuselage. Presented at the VFS International Forum 75, Philadelphia, Pennsylvania, 2019.

[33] Padulo, M., Campobasso, M. S., and Guenov, M. D. "Novel Uncertainty Propagation Method for Robust Aerodynamic Design." *AIAA Journal*, Vol. 49, No. 3, 2011, pp. 530–543. https://doi.org/10.2514/1.J050448.

[34] Ricks, N., Abraham, S., Contino, F., and Ghorbaniasl, G. "Uncertainty Quantification for the Aeroacoustics of Rotating Blades in the Time Domain." *Applied Acoustics*, Vol. 139, 2018, pp. 57–68. https://doi.org/10.1016/j.apacoust.2018.04.012.

[35] Vouros, S., Goulos, I., Scullion, C., Nalianda, D., and Pachidis, V. “Impact of Tip-Vortex Modeling Uncertainty on Helicopter Rotor Blade–Vortex Interaction Noise Prediction.” *Journal of the American Helicopter Society*, Vol. 66, No. 1, 2021, pp. 1–13. https://doi.org/10.4050/JAHS.66.012005.

[36] Ton, C. T., McCourt, M., and Mehta, S. S. Robust Tracking Control of a Quadrotor with Time-Varying Gain in the Presence of Uncertainty and Disturbances. Presented at the AIAA Guidance, Navigation, and Control Conference, San Diego, California, 2016.

[37] Islam, S., Dias, J., and Xiros, N. Robust Adaptive Finite-Time Tracking Control for Unmanned Aerial Vehicle with Uncertainty. Presented at the 2020 American Control Conference, 2020.

[38] Din, I. S. E., Khurana, M., and Yeo, H. Towards Uncertainty Quantification of the ONERA 7A Rotor Using Comprehensive Analysis. Presented at the 47th European Rotorcraft Forum, 2021.

[39] Siva, C., Murugan, M. S., and Ganguli, R. “Uncertainty Quantification in Helicopter Performance Using Monte Carlo Simulations.” *Journal of Aircraft*, Vol. 48, No. 5, 2011, pp. 1503–1511. https://doi.org/10.2514/1.C000288.

[40] Soban, D. S., and Mavris, D. N. “Assessing the Impact of Technology on Aircraft Systems Using Technology Impact Forecasting.” *Journal of Aircraft*, Vol. 50, No. 5, 2013, pp. 1380–1393. https://doi.org/10.2514/1.C031871.

[41] Box, G. E. P., and Draper, N. R. *Empirical Model-Building and Response Surfaces*. John Wiley & Sons, Oxford, England, 1987.

[42] Montgomery, D. C. *Design and Analysis of Experiments*. John Wiley & Sons, Inc, Hoboken, New Jersey, 2013.

[43] Oliver, M. A., and Webster, R. “Kriging: A Method of Interpolation for Geographical Information Systems.” *International journal of geographical*

information systems, Vol. 4, No. 3, 1990, pp. 313–332. https://doi.org/10.1080/02693799008941549.

[44] Pal, S. K., and Mitra, S. "Multilayer Perceptron, Fuzzy Sets, and Classification." *IEEE Transactions on Neural Networks*, Vol. 3, No. 5, 1992, pp. 683–697. https://doi.org/10.1109/72.159058.

[45] Lee, D., Jeong, S., and Yee, K. Development of a Conceptual Design Tool for Various Compound Helicopters. Presented at the 44th European Rotorcraft Forum, Delft, Netherlands, 2018.

[46] Kang, S., Lee, D., Jeong, S., and Yee, K. Sizing Methodology and Performance Assessment of Hybrid Electric Propulsion Aircraft. Presented at the 7th Asian/Australian Rotorcraft Forum, Jeju, Republic of Korea, 2018.

[47] Kim, H., and Yee, K. "A Novel Cost Estimation Method for UAM eVTOLs." *Journal of the Korean Society for Aeronautical & Space Sciences*, Vol. 49, No. 3, 2021, pp. 233–241. https://doi.org/10.5139/JKSAS.2021.49.3.233.

[48] Brown, A. *A Vehicle Design and Optimization Model for On-Demand Aviation*. Master Thesis. Massachusetts Institute of Technology, 2018.

[49] Leishman, G. J. *Principles of Helicopter Aerodynamics*. Cambridge University Press, 2006.

[50] Johnson, W. *Rotorcraft Aeromechanics*. Cambridge University Press, 2013.

[51] Du, Z., and Selig, M. A 3-D Stall-Delay Model for Horizontal Axis Wind Turbine Performance Prediction. Presented at the 1998 ASME Wind Energy Symposium, Reno, Nevada, 1998.

[52] Bell Helicopter. *Advancement of Proprotor Technology. Task 2: Wind-Tunnel Test Results*. Publication REPT-300-099-004. 1971.

[53] Koning, W. J. F., Acree, C. W. J., and Rajagopalan, G. Using RotCFD to Predict Isolated XV-15 Rotor Performance. Presented at the AHS Technical

Meeting on Aeromechanics Design for Vertical Lift, San Francisco, California, 2016.

[54] Helf, S., Broman, E., Gatchel, S., and Charles, B. *Full Scale Hover Test of a 25 Foot Tilt Rotor*. Publication NASA-CR-114626. 1973.

[55] Gudmundsson, S. Chapter 9 – The Anatomy of the Wing. In *General Aviation Aircraft Design*, Butterworth-Heinemann, Boston, 2014, pp. 299–399.

[56] Scholz, D., and Nita, M. Estimating the Oswald Factor from Basic Aircraft Geometrical Parameters. Presented at the German Aerospace Congress, Berlin, 2012.

[57] Harris, F. D. *Introduction to Autogyros, Helicopters, and Other V/STOL Aircraft*. National Aeronautics and Space Administration, Ames Research Center, Moffett Field, California, 2011.

[58] Ferguson, S., W. *Development and Validation of a Simulation for Generic Tilt-Rotor Aircraft*. Publication CR-166537. Systems Technology, Mountain View, California, 1989.

[59] German, B. Introduction to Batteries and Cell Discharge Modeling for Electric Aircraft Design. , 2018.

[60] Qinghua, L. *Analysis, Design and Control of Permanent Magnet Synchronous Motors for Wide-Speed Operation*. Ph.D. Dissertation. National University of Singapore, 2005.

[61] Ding, X., Guo, H., Xiong, R., Chen, F., Zhang, D., and Gerada, C. "A New Strategy of Efficiency Enhancement for Traction Systems in Electric Vehicles." *Applied Energy*, Vol. 205, 2017, pp. 880–891. https://doi.org/10.1016/j.apenergy.2017.08.051.

[62] Jansen, R., Bowman, C., and Jankovsky, A. Sizing Power Components of an Electrically Driven Tail Cone Thruster and a Range Extender. Presented at

the 16th AIAA Aviation Technology, Integration, and Operations Conference, Washington, D.C., 2016.

[63] Stückl, S. *Methods for the Design and Evaluation of Future Aircraft Concepts Utilizing Electric Propulsion Systems*. Ph.D. Dissertation. Technical University of Munich.

[64] Liu, Y.-T., Liu, S., Li, G.-R., and Gao, X.-P. "Strategy of Enhancing the Volumetric Energy Density for Lithium–Sulfur Batteries." *Advanced Materials*, Vol. 33, No. 8, 2021, p. 2003955. https://doi.org/10.1002/adma.202003955.

[65] Silva, C., Johnson, W. R., Solis, E., Patterson, M. D., and Antcliff, K. R. VTOL Urban Air Mobility Concept Vehicles for Technology Development. Presented at the 2018 Aviation Technology, Integration, and Operations Conference, Atlanta, Georgia, 2018.

[66] Krishnan, R., and Bharadwaj, A. S. A Comparative Study of Various Motor Drive Systems for Aircraft Applications. Presented at the Conference Record of the 1991 IEEE Industry Applications Society Annual Meeting, 1991.

[67] Dorn-Gomba, L., Ramoul, J., Reimers, J., and Emadi, A. "Power Electronic Converters in Electric Aircraft: Current Status, Challenges, and Emerging Technologies." *IEEE Transactions on Transportation Electrification*, Vol. 6, No. 4, 2020, pp. 1648–1664. https://doi.org/10.1109/TTE.2020.3006045.

[68] Anton, D. F. EAircraft: Hybrid-Elektrische Antriebe Für Luftfahrzeuge. , 2019.

[69] Type-Certificate Data Sheet for Type E-811 Engine. EASA, May 18, 2020.

[70] Brown, G. Weights and Efficiencies of Electric Components of a Turboelectric Aircraft Propulsion System. Presented at the 49th AIAA Aerospace Sciences Meeting including the New Horizons Forum and Aerospace Exposition, Orlando, Florida, 2011.

[71] Jansen, R. H., Bowman, C. L., Clarke, S., Avanesian, D., Dempsey, P. J., and Dyson, R. W. “NASA Electrified Aircraft Propulsion Efforts.” *Aircraft Engineering and Aerospace Technology*, Vol. 92, No. 5, 2020, pp. 667–673. https://doi.org/10.1108/AEAT-05-2019-0098.

[72] Schwartzberg, M. A., Smith, R. L., Means, J. L., Law, H. Y. H., and Chappell, D. P. *Single-Rotor Helicopter Design and Performance Estimation Programs. Volume I. Methodology*. Publication ADA040803. Army Air Mobility Research and Development Laboratory, 1977.

[73] Johnson, W. NDARC — NASA Design and Analysis of Rotorcraft Validation and Demonstration. Presented at the American Helicopter Society Aeromechanics Specialists’ Conference, 2010.

[74] U., S. *Tilt Rotor and Compound Helicopter Mass Modelling*. Publication GARTEUR/TP-036/2. GARTEUR, 1987, p. 297.

[75] White, G. “A Tilt-Rotor Actuator.” *Proceedings of the Institution of Mechanical Engineers, Part G: Journal of Aerospace Engineering*, Vol. 224, No. 6, 2010, pp. 657–672. https://doi.org/10.1243/09544100JAERO666.

[76] Vegh, J. M., Botero, E., Clarke, M., Smart, J., and Alonso, J. Current Capabilities and Challenges of NDARC and SUAVE for EVTOL Aircraft Design and Analysis. Presented at the AIAA Propulsion and Energy 2019 Forum, Indianapolis, Indiana, 2019.

[77] Roskam, J. *Airplane Design Part V: Component Weight Estimation*. Design, Analysis and Research Corporation, Lawrence, Kan, 1999.

[78] Gudmundsson, S. Chapter 2 - Aircraft Cost Analysis. In *General Aviation Aircraft Design*, Butterworth-Heinemann, Boston, 2014, pp. 33–53.

[79] Beltramo, M. N., Trapp, D. L., Kimoto, B. W., and Marsh, D. P. *Parametric Study of Transport Aircraft Systems Cost and Weight*. Publication NASA-CR-151970. 1977.

[80] Hasan, S. Urban Air Mobility (UAM) Market Study. Jun, 2019.

[81] Finger, D., Götten, F., Braun, C., and Bil, C. Cost Estimation Methods for Hybrid-Electric General Aviation Aircraft. Presented at the Asia Pacific International Symposium on Aerospace Technology, Gold Coast, Australia, 2019.

[82] Scott, R., Vegh, J. M., and AvMC, U. A. C. Progress Toward a New Conceptual Assessment Tool for Aircraft Cost. Presented at the AHS International Forum 76, VIRTUAL EVENT, 2020.

[83] Kotwicz Herniczek, M., Feszty, D., Meslioui, S.-A., and Park, J. Applicability of Early Acoustic Theory for Modern Propeller Design. Presented at the 23rd AIAA/CEAS Aeroacoustics Conference, Denver, Colorado, 2017.

[84] Schlegel, R., King, R., and Mull, H. *Helicopter Rotor Noise Generation and Propagation*. Defense Technical Information Center, Fort Belvoir, Virginia, 1966.

[85] Uber Elevate. *Fast-Forwarding to a Future of On-Demand Urban Air Transportation*. 2016, p. 98.

[86] Kurtz, D. W., and Marte, J. E. *A Review of Aerodynamic Noise from Propellers, Rotors, and Lift Fans*. Publication NASA-CR-107568. 1970.

[87] Oberkampf, W., and Roy, C. *Verification and Validation in Scientific Computing*. Cambridge University Press, 2010.

[88] Hosder, S., and Bettis, B. R. "Uncertainty and Sensitivity Analysis for Reentry Flows with Inherent and Model-Form Uncertainties." *Journal of Spacecraft and Rockets*, Vol. 49, No. 2, 2012, pp. 193–206. https://doi.org/10.2514/1.A32102.

[89] Bettis, B., Hosder, S., and Winter, T. Efficient Uncertainty Quantification in Multidisciplinary Analysis of a Reusable Launch Vehicle. Presented at the

17th AIAA International Space Planes and Hypersonic Systems and Technologies Conference, San Francisco, California, 2011.

[90] West, T. K., and Phillips, B. D. “Multifidelity Uncertainty Quantification of a Commercial Supersonic Transport.” *Journal of Aircraft*, Vol. 57, No. 3, 2020, pp. 491–500. https://doi.org/10.2514/1.C035496.

[91] Lim, D., Kim, H., and Yee, K. “Uncertainty Propagation in Flight Performance of Multirotor with Parametric and Model Uncertainties.” *Aerospace Science and Technology*, Vol. 122, 2022, p. 107398. https://doi.org/10.1016/j.ast.2022.107398.

[92] Park, H.-U., Lee, J.-W., Chung, J., and Behdinan, K. “Uncertainty-Based MDO for Aircraft Conceptual Design.” *Aircraft Engineering and Aerospace Technology*, Vol. 87, No. 4, 2015, pp. 345–356. https://doi.org/10.1108/AEAT-07-2013-0128.

[93] Aughenbaugh, J. M., and Paredis, C. J. J. The Value of Using Imprecise Probabilities in Engineering Design. Presented at the ASME 2005 Design Engineering Technical Conferences and Computers and Information in Engineering Conference, Long Beach, California, 2005.

[94] Azizian, N., Shahram, S., and Mazzuchi, T. “A Comprehensive Review and Analysis of Maturity Assessment Approaches for Improved Decision Support to Achieve Efficient Defense Acquisition.” *Lecture Notes in Engineering and Computer Science*, Vol. 2179, 2009.

[95] Fernandez, J. A. *Contextual Role of TRLs and MRLs in Technology Management.* Publication SAND2010-7595. Sandia National Laboratories, Albuquerque, New Mexico, and Livermore, California, 2010.

[96] Sauser, B., Gove, R., Forbes, E., and Ramirez-Marquez, J. E. “Integration Maturity Metrics: Development of an Integration Readiness Level.” *Information Knowledge Systems Management*, Vol. 9, No. 1, 2010, pp. 17–46. https://doi.org/10.3233/IKS-2010-0133.

[97] Sauser, B. J., Long, M., Forbes, E., and McGrory, S. E. “Defining an Integration Readiness Level for Defense Acquisition.” *INCOSE International Symposium*, Vol. 19, No. 1, 2009, pp. 352–367. https://doi.org/10.1002/j.2334-5837.2009.tb00953.x.

[98] Kujawski, E. “Analysis and Critique of the System Readiness Level.” *IEEE Transactions on Systems, Man, and Cybernetics: Systems*, Vol. 43, No. 4, 2013, pp. 979–987. https://doi.org/10.1109/TSMCA.2012.2209868.

[99] Peisen, D. J., and Schulz, C. L. *Task Order 221 Case Studies: Time Required to Mature Aeronautic Technologies to Operational*. SAIC, Arlington, Virginia, 1999, p. 40.

[100] Helton, J. C., and Davis, F. J. “Latin Hypercube Sampling and the Propagation of Uncertainty in Analyses of Complex Systems.” *Reliability Engineering & System Safety*, Vol. 81, No. 1, 2003, pp. 23–69. https://doi.org/10.1016/S0951-8320(03)00058-9.

[101] Berger, M. P. F. “D-Optimal Sequential Sampling Designs for Item Response Theory Models.” *Journal of Educational Statistics*, Vol. 19, No. 1, 1994, pp. 43–56. https://doi.org/10.3102/10769986019001043.

[102] Joe, S., and Kuo, F. Y. “Constructing Sobol Sequences with Better Two-Dimensional Projections.” *SIAM Journal on Scientific Computing*, Vol. 30, No. 5, 2008, pp. 2635–2654. https://doi.org/10.1137/070709359.

[103] Jospin, L. V., Buntine, W., Boussaid, F., Laga, H., and Bennamoun, M. “Hands-on Bayesian Neural Networks -- a Tutorial for Deep Learning Users.” *IEEE Computational Intelligence Magazine*, Vol. 17, No. 2, 2022, pp. 29–48. https://doi.org/10.1109/MCI.2022.3155327.

[104] Vittal, S., and Hajela, P. Confidence Intervals for Reliability Estimated Using Response Surface Methods. Presented at the 9th AIAA/ISSMO Symposium on Multidisciplinary Analysis and Optimization, Atlanta, Georgia, 2002.

[105] Kim, C., and Choi, K. K. “Reliability-Based Design Optimization Using Response Surface Method with Prediction Interval Estimation.” *Journal of Mechanical Design*, Vol. 130, No. 12, 2008. https://doi.org/10.1115/1.2988476.

[106] Gal, Y., and Ghahramani, Z. “Dropout as a Bayesian Approximation: Representing Model Uncertainty in Deep Learning.” 2015. https://doi.org/10.48550/arXiv.1506.02142.

[107] Lee, Y., and Yee, K. “Numerical Prediction of Scientific Balloon Trajectories While Considering Various Uncertainties.” *Journal of Aircraft*, Vol. 54, No. 2, 2017, pp. 768–782. https://doi.org/10.2514/1.C033998.

[108] Lee, S., Yee, K., and Rhee, D.-H. “Optimum Arrangement of Film Cooling Holes Considering the Manufacturing Tolerance.” *Journal of Propulsion and Power*, Vol. 33, No. 4, 2017, pp. 793–803. https://doi.org/10.2514/1.B36210.

[109] Roger G., G., and Pol D., S. *Stochastic Finite Elements: A Spectral Approach | SpringerLink*. Springer, 1991.

[110] Lim, D., Li, Y., LeVine, M. J., Kirby, M., and Mavris, D. N. Parametric Uncertainty Quantification of Aviation Environmental Design Tool. Presented at the 2018 Multidisciplinary Analysis and Optimization Conference, Atlanta, Georgia, 2018.

[111] Parzen, E. “On Estimation of a Probability Density Function and Mode.” *Annals of Mathematical Statistics*, Vol. 33, No. 3, 1962, pp. 1065–1076. https://doi.org/10.1214/aoms/1177704472.

[112] Droney, C. K., Harrison, N. A., and Gatlin, G. M. Subsonic Ultra-Green Aircraft Research: Transonic Truss-Braced Wing Technical Maturation. Presented at the 31st Congress of the international Council of the Aeronautical Sciences, Belo Horizonte, Brazil.

[113] Bartels, R., Scott, R., Allen, T. J., and Sexton, B. W. The Boeing SUGAR Truss-Braced Wing Aircraft: Wind-Tunnel Data and Aeroelastic Analyses. Apr 16, 2015.

[114] Varzi, A., Thanner, K., Scipioni, R., Di Lecce, D., Hassoun, J., Dörfler, S., Altheus, H., Kaskel, S., Prehal, C., and Freunberger, S. A. "Current Status and Future Perspectives of Lithium Metal Batteries." *Journal of Power Sources*, Vol. 480, 2020, p. 228803. https://doi.org/10.1016/j.jpowsour.2020.228803.

[115] "AWS Prescriptive Guidance - Quantifying Uncertainty in Deep Learning Systems." 2020, p. 25.

[116] Wang, B., Shi, W., and Miao, Z. "Confidence Analysis of Standard Deviational Ellipse and Its Extension into Higher Dimensional Euclidean Space." *PloS one*, Vol. 10, 2015, p. e0118537. https://doi.org/10.1371/journal.pone.0118537.

[117] Gong, X. *Modeling of Lithium-Ion Battery Considering Temperature and Aging Uncertainties*. Ph.D. Dissertation. University of Michigan-Dearborn.

[118] Barcellona, S., Brenna, M., Foiadelli, F., Longo, M., and Piegari, L. "Analysis of Ageing Effect on Li-Polymer Batteries." *The Scientific World Journal*, Vol. 2015, 2015, pp. 1–8. https://doi.org/10.1155/2015/979321.

[119] Wilk, M. B., and Gnanadesikan, R. "Probability Plotting Methods for the Analysis of Data." *Biometrika*, Vol. 55, No. 1, 1968, pp. 1–17. https://doi.org/10.1093/biomet/55.1.1.

[120] Kim, H., Lee, D., Seo, J., Hong, Y., and Yee, K. Design Methodology of Urban Air Mobility for Noise Mitigation at Conceptual Design Stage. Presented at the 48th European Rotorcraft Forum, Winterthur, Switzerland, 2022.

국문 초록

지난 수십 년 동안, 항공기의 여러 학제에서 성취한 획기적인 기술발전으로 오늘날 미래항공 모빌리티로 통칭되는 새로운 항공 시스템이 출현하였다. 특히, 전기동력 추진기술의 성숙도 향상은 미래항공 모빌리티의 다양한 형상과 도심 지역에서의 운용을 가능하게 만든 가장 강력한 요인 중 하나이다.

미래항공 모빌리티의 새로운 특성은 항공기 설계의 시작점인 초기 설계단계에서 지난 반세기 동안 축적된 과거 데이터를 사용하는데 어려움을 유발한다. 따라서 미래항공 모빌리티의 초기 사이징은 물리이론 기반의 설계 접근법을 요구하고, 이와 동시에 개념설계단계의 중요성이 이전에 비해 더욱 상승하였다. 신뢰성 있는 미래항공 모빌리티 설계결과를 도출하기 위한 노력의 일환으로, 본 연구에서는 통계적, 확률론적 방법론을 접목시켜 개념설계단계에서 다뤄지는 중요한 두 가지 주요 업무를 개선하였다.

첫 번째는 효용 최대화와 비용 최소화로 항공기 개발을 성공으로 이끌 기술 포트폴리오를 결정하는 "기술평가" 업무이다. 본 연구에서 제시된 불확실성 기반 기술 포트폴리오 평가 프레임워크는 기술 간의 상호 작용과 기술 효과 예측에서 개선된 수학모델을 수립하였다. 또한 근사모델에 존재하는 불확실성을 고려하여 보다 현실적이고 실용적인 결과를 도출할 수 있다. 이 방법론을 통해 개념설계단계에서 의사결정에

필요한 정보 및 지식 수준을 높일 수 있으며, 이는 결과적으로 미래항공 모빌리티의 개발비용과 반복적인 설계 피드백 횟수를 줄일 수 있다.

두 번째는 상세설계단계를 위해 초기에 전반적인 형상과 중량 분포를 계산하는 "사이징"이다. 본 연구에서는 미래항공 모빌리티 설계를 위한 결정론적 사이징 프레임워크를 우선 제시하고, 이를 기반으로 하여 형상변수와 단순화된 수학적 해석 모듈에 존재하는 불확실성을 몬테카를로 시뮬레이션을 통해 사이징 프레임워크에 반영하였다. 불확실성을 고려한 사이징은 사이징 결과에 적절한 설계여유를 확보하고, 초기설계단계에서 불확실성에 대한 시스템의 반응을 이해할 수 있도록 하여 의사 결정론자가 이후 설계단계를 준비하는데 도움이 될 수 있다.

두 가지 개선된 프레임워크는 전기동력 수직이착륙기 형태의 가상의 미래항공 모빌리티 설계에 적용되었다. 예제 프로젝트는 제시된 두 방법론의 적용 및 결과분석에 대한 예제로서 이를 통해 방법론의 유효성을 확인할 수 있다. 불확실성 기반의 기술 포트폴리오 평가 프레임워크와 미래항공 모빌리티 사이징 프레임워크 두 가지 모두 범용적인 방법론으로서 제시된 예제뿐만 아니라 다양한 항공기 개발 프로그램에 적용할 수 있다.

주요어: 미래항공 모빌리티, 전기동력 수직이착륙기, 개념설계, 사이징, 다학제해석, 기술 포트폴리오 평가, 불확실성 기반 설계, 불확실성 정량화, 모델 불확실성

학번: 2017-27961

성명: 임대진